A Piezoelectric Energy Harvester Emulator for Circuit Evaluation

Mathijs van Binnendijk

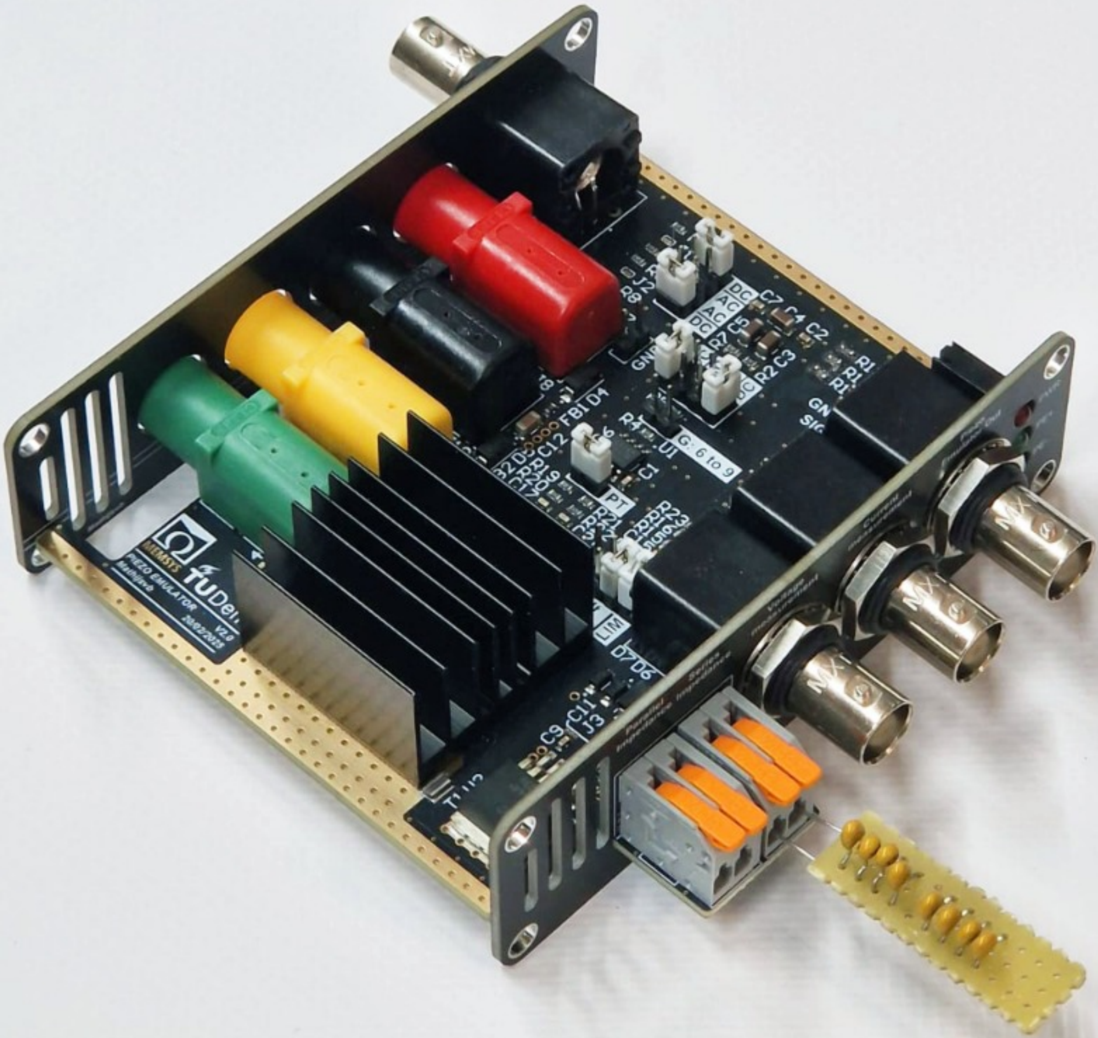

Delft University of Technology

TU Delft

A Piezoelectric Energy Harvester Emulator for Circuit Evaluation

by

Mathijs van Binnendijk

to obtain the degree of Master of Science
at the Delft University of Technology,
to be defended publicly on Thursday September 4, 2025 at 12:45 AM.

Student number:	4583957	
Project duration:	September 9, 2024 – September 4, 2025	
Thesis committee:	Dr. P. Pawełczak,	TU Delft, supervisor
	Dr. G. Iosifidis,	TU Delft
	Dr. T. Blad,	MEMSYS B.V.
	Ir. N. Hokke,	MEMSYS B.V.

Style: TU Delft Report Style, with modifications by Daan Zwaneveld

An electronic version of this thesis is available at `http://repository.tudelft.nl/`.

Preface

This thesis marks the final stage of my Master's program in Embedded Systems Engineering at the Delft University of Technology and was carried out in close collaboration with MEMSYS, a company specializing in vibration-based energy harvesting systems.

The motivation for this work originated from a shared challenge identified during early discussions with MEMSYS: the difficulty of consistently evaluating energy harvesting circuits due to the nonlinear and often chaotic behavior of real piezoelectric energy harvesters. What began as a technical curiosity and side project, the idea of creating a hardware emulator capable of reproducing piezoelectric energy harvester (PEH) behavior in a controlled and repeatable way, gradually evolved into the central research focus of this thesis.

This project truly pushed me beyond my comfort zone. Coming from a background in embedded systems, I found myself diving deep into the unfamiliar worlds of analog electronics and mechanical dynamics. It required me to learn a great deal in a short period, all while balancing my operational responsibilities within MEMSYS. The process was intense, but I also enjoyed it a lot. Few things compare to the satisfaction of finally getting a prototype to work after several failed attempts, especially when you're not even sure if what you're trying is technically possible. I enjoyed this project so much that this thesis does not represent the end, but rather a snapshot along the way. I will continue development on this system beyond the conclusion of this thesis in collaboration with MEMSYS.

Of course, I did not do this alone. I would like to express my gratitude to several individuals. First, my colleague Niels, thank you for your positivity and for your guidance, both technically and personally. Your feedback over the past year and your encouragement during countless debugging sessions meant a lot. I am also grateful to my MEMSYS supervisor, Thijs, not only for your thoughtful feedback throughout the year but also for founding MEMSYS, a place where I, and many others, have been given the opportunity to learn and grow in an inspiring environment.

I would also like to thank my TU Delft supervisor, Dr. P. Pawelczak, for his advice during our meetings and for allowing me to work so independently. I feel that I learned a great deal from being given that level of freedom, and I recognize that it also required trust on his part.

To my partner, Ilse, thank you for being so supportive during the difficult moments and for being someone to celebrate with in the good ones. Your support helped me recharge and show up with new energy each day.

Lastly, I would like to thank the entire MEMSYS team for their support, for being part of this journey, and for fostering such a positive and motivating work environment. I look forward to continuing to work alongside all of you.

Mathijs van Binnendijk
Delft, August 2025

Abstract

This thesis presents the design, implementation, and validation of a piezoelectric energy harvester (PEH) emulator to enable repeatable evaluation of energy extraction circuits for vibration-based systems. PEHs convert mechanical vibrations into electricity using materials that generate charge under stress, offering compact, maintenance-free power for low-power electronics.

Efficient energy extraction from PEHs requires specialized circuits whose performance depends heavily on the PEH's electrical characteristics. However, real PEHs often exhibit nonlinear and chaotic behavior, complicating consistent testing and comparison. The proposed emulator overcomes this by replicating PEH electrical behavior in a controlled, configurable, and repeatable way.

The emulator employs a voltage-controlled voltage source with analog impedance modeling, supporting output ranges up to $\pm 25\,\mathrm{V}$ and $3\,\mathrm{A}$. It includes modular impedance matching and real-time responsiveness without digital latency. A complete prototype was built and tested. Simulations showed stable operation under various conditions, and experimental results demonstrated 80–100% accuracy in reproducing PEH power output.

To the author's knowledge, this is the first emulator designed specifically for PEHs, addressing a gap in existing literature. While emulators are common in photovoltaic and thermoelectric domains, none existed for piezoelectric harvesters. This work establishes a flexible benchmarking platform and outlines paths for improving emulator accuracy via improved impedance modeling and alternative architectures.

Contents

Nomenclature

Abbreviations

Abbreviation	Definition
AC	Alternating Current
AWG	Arbitrary Waveform Generator
BNC	Bayonet Neill–Concelman (connector)
DC	Direct Current
DUT	Device Under Test
EMI	Electromagnetic Interference
FFT	Fast Fourier Transform
GUI	Graphical User Interface
I-V	Current-Voltage
LTspice	Linear Technology Simulation Program with Integrated Circuit Emphasis
MCU	Microcontroller Unit
MPPT	Maximum Power Point Tracking
PCB	Printed Circuit Board
PEH	Piezoelectric Energy Harvester
PV	Photovoltaic
RMS	Root Mean Square
SECE	Synchronous Electric Charge Extraction
SEH	Standard Energy Harvester
SSHI	Synchronized Switch Harvesting on Inductor
TEG	Thermoelectric Generator

Symbols

Symbol	Definition	Unit
C_p	Capacitance of the piezoelectric patch	[F]
C_r	Smoothing capacitor in the rectifier circuit	[F]
E_{elec}	Electrical energy in the system	[J]
E_{mech}	Mechanical energy in the system	[J]
G_{BUF}	Gain of the buffer amplifier	[-]
G_{INA}	Gain of the instrumentation amplifier	[-]
i_l	Load current from the piezoelectric patch	[A]
i_p	Current generated by the piezoelectric patch	[A]
K	Stiffness coefficient (linear)	[N/m]
$K(x)$	Nonlinear stiffness coefficient	[N/m]
k_m^2	Electromechanical coupling coefficient	[-]
L	Inductance in energy extraction circuits	[H]
M	Mass of the vibrating structure	[kg]
R	Electrical resistance (generic)	[Ω]
R_p	Parallel resistance for impedance matching	[Ω]
S	Switch state in energy extraction circuit	[-]
T	Time	[s]
v_p	Voltage across the piezoelectric patch	[V]

Symbol	Definition	Unit
v_r	Rectified voltage after full-bridge rectifier	[V]
V_{OC}	Open-circuit voltage at max displacement	[V]
x	Relative displacement of mass to base	[m]
x_0	Equilibrium position in bistable systems	[m]
X_{OC}	Maximum open-circuit displacement	[m]
y	Displacement of the base	[m]
Z_l	Electrical load impedance	[Ω]
α	Force voltage factor of the harvester	[N/V]
ω_n	Resonant frequency (short-circuit)	[rad/s]
c	Damping coefficient of the mechanical system	[N·s/m]

1

Introduction

1.1. Context

This thesis was carried out in collaboration with MEMSYS, a company focused on developing vibration-based energy harvesting systems for industrial applications. Their work centers on piezoelectric energy harvesters, which convert mechanical vibrations into electrical energy to power low-power devices such as wireless sensor nodes.

In recent years, many circuit techniques have been proposed to improve energy extraction from these systems. However, evaluating and comparing the performance of such circuits remains challenging. Physical PEH devices can exhibit complex and nonlinear behavior, making experiments difficult to replicate and results difficult to compare across different studies.

In other energy harvesting fields, such as photovoltaics and thermoelectrics, similar issues have been addressed through the use of emulator systems. These devices replicate the electrical behavior of real harvesters in a repeatable and controllable way. Inspired by these approaches, this work focuses on the design and validation of an emulator for piezoelectric energy harvesters. The goal is to create a tool that enables consistent, accurate evaluation of energy extraction circuits, independent of the limitations, variability and chaotic behavior found in PEH devices.

1.2. Background

Wireless sensors are essential for a variety of applications, including machinery condition monitoring, environmental data collection, and the management of smart infrastructure systems. Traditionally, these devices are powered by electrochemical batteries, but this approach has several drawbacks. Batteries require frequent replacement or recharging, which can be both expensive and impractical, especially at scale or in hard-to-access locations. Additionally, the stored energy in batteries poses safety risks if suddenly released due to a failure. Lastly, the need for the eventual disposal of batteries comes with environmental concerns. To address these challenges, significant research has been devoted to developing energy harvesting technologies. Energy harvesters are systems with the ability to transform surrounding ambient energy into electrical energy. This collected electrical energy can be used to power low-power electronic devices such as wireless sensors.

There are several forms of ambient energy. The most common sources and their respective power densities can be seen in Figure 1.1. Harvesting energy from environmental sources comes with challenges that vary depending on the type of energy that is being harvested. Solar energy harvesting is highly dependent on the availability of sunlight, which can fluctuate due to weather conditions, the time of day or indoor lighting conditions. It is also unsuitable for deployment in environments with consistent shade. Similarly, thermal energy harvesting relies on temperature gradients, which may not be present or significant enough to generate sufficient power. Radiofrequency energy harvesting is limited by the availability of RF signals, which tend to have low energy densities unless in close proximity to transmitters. Mechanical energy harvesting will be discussed in the next section.

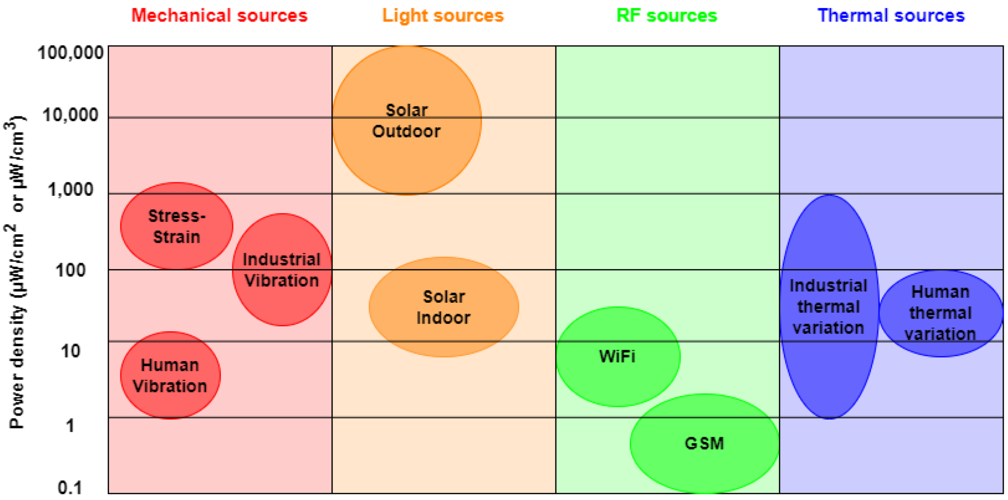

Figure 1.1: Different sources of environmental energy and their power respective densities [1].

1.2.1. Mechanical Energy Harvesting Technologies

Mechanical energy harvesting is preferable in environments where other sources of environmental energy are either not available, too costly, or unable to provide sufficient energy. It relies on the ability to convert mechanical energy into electrical energy. This conversion is done using electrostatic, electromagnetic, or piezoelectric mechanisms. Among these mechanisms, piezoelectric energy harvesting is often favored due to its high energy density, long lifetimes, higher sensitivity for low stresses, and its ability to be unaffected by environmental conditions [1].

1.2.2. Piezoelectric Energy Harvesting

The principle of piezoelectric energy harvesting lies in the ability of certain materials, known as piezoelectric materials, to generate an electrical potential when subjected to mechanical stress. A piezoelectric energy harvester typically consists of piezoelectric material integrated into a structure designed to convert ambient mechanical energy into electrical energy by inducing mechanical stress in the piezoelectric element.

An example of such a system, designed specifically for harvesting energy from vibrations, is shown in Figure 1.2. In this setup, a mass is connected to a base structure via a flexible substrate. When the base moves, the attached mass also moves, causing the substrate to flex. This flexing action stretches or compresses the piezoelectric patch, generating a potential difference between its electrodes. This potential difference can then be harnessed to supply energy to an attached load. This type of PEH is known as a cantilever.

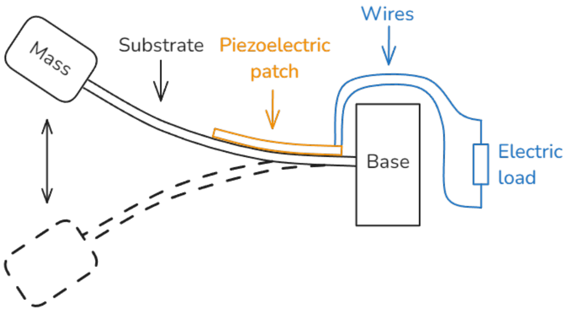

Figure 1.2: Example of a linear piezoelectric energy harvesting structure based on a mass attached to a flexible substrate.

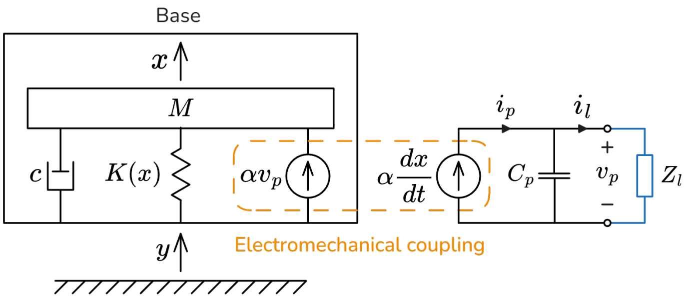

Figure 1.3: A single-degree-of-freedom model of a piezoelectric energy harvesting system.

Harvester Dynamics

To better understand the dynamic behavior of PEHs, it is useful to describe their operation using a simplified mechanical model. Systems like the one shown in Figure 1.2 can be represented using a single-degree-of-freedom (SDOF) model [2]. This abstraction captures the essential physics of base-excited PEH systems and their electromechanical coupling, allowing for analytical study of both mechanical motion and electrical output. The SDOF model used throughout this work is shown in Figure 1.3. The governing equations for this model are given by

$$M\frac{d^2x}{dt^2} + c\frac{dx}{dt} + Kx + \alpha v_p = -M\frac{d^2y}{dt^2}, \tag{1.1}$$

and

$$i_l = \alpha\frac{dx}{dt} - C_p\frac{dv_p}{dt}. \tag{1.2}$$

Here:

- M: Mass of the vibrating structure.
- x: Displacement of the mass relative to the base.
- y: Base displacement due to external excitation.
- c: Damping coefficient.
- K: Stiffness coefficient.
- α: Force voltage factor of the harvester.
- C_p: Capacitance of the piezoelectric patch.
- v_p: Voltage across the piezoelectric patch.
- i_p: Current generated by the piezoelectric patch.
- i_l: Part of the current generated by the piezoelectric patch moving into the load.
- Z_l: Impedance of the electrical load attached to the piezoelectric patch.

Equation 1.1 describes the mechanical dynamics of the system. These dynamics are governed by an external force acting on a base causing a displacement of the base (y). The base has a mass-spring-damper system attached, with the additional term αv_p. This term represents the coupling effect introduced by the piezoelectric material, linking the electrical domain to the mechanical domain. Similarly, Equation 1.2 outlines the electrical dynamics, which are governed by the flow of current in the system. The current source is directly related to the mass's velocity through the term $\alpha(dx/dt)$, which represents the coupling between the mechanical motion and the electrical output. This demonstrates that the mechanical and electrical dynamics are directly interconnected. A voltage across the piezoelectric patch generates a force that acts on the mechanical system, while the velocity of the mass induces a current in the electrical system.

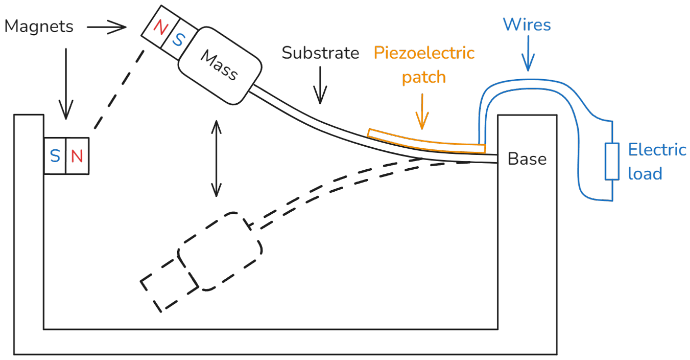

Figure 1.4: Example of a nonlinear piezoelectric energy harvesting structure based on a mass attached to a flexible substrate and two permanent magnets.

Linear vs Nonlinear Harvesters

Figure 1.3 shows a linear piezoelectric energy harvester with its dynamics outlined in Equation 1.1. Linear systems only have a single stable point in terms of displacement. Furthermore, linear systems are characterized by resonant behavior. The resonant frequency for a linear harvester in short circuit condition ω_n is defined as

$$\omega_n = \sqrt{\frac{K}{M}}. \tag{1.3}$$

Linear harvesters are only suitable for harvesting energy from vibrations at or near the resonant frequency. Attempting to harvest energy from vibrations with a frequency differing from the resonance frequency leads to reduced power output [3]. This means the frequency bandwidth of these types of harvesters is typically quite narrow. This makes linear harvesters unsuitable for applications that require energy to be harvested from various frequencies of vibration. Nonlinear harvesters can be tuned to harvest effectively from a wider range of frequencies [4]. In this context, nonlinear refers to the nonlinear stiffness $K(x)$ used in the system.

Figure 1.4 shows an example of such a nonlinear structure based on the linear structure discussed earlier. Here, the addition of two permanent magnets causes a repulsive force that is strongest at the point of zero displacement and lessens as the mass moves further away. This creates a nonlinear relationship between force acting on the mass and deflection, which creates two stable displacement points instead of one. This effect is visualized in the plots of Figure 1.5. Here, the force deflection curve visualizes how the nonlinear stiffness can create two stable points of displacement. The Phase-space and time varying waveforms show different behaviors for different amplitudes of oscillation. Here, the blue and orange lines represent the behavior of the system with a low amplitude harmonic vibration as input. The low amplitude results in oscillations around one of the stable points, since there is not enough energy to move in between both stable points. This phenomenon is referred to as intra-well motion. As the input vibrations increase in amplitude, it becomes possible for the mass to achieve a higher energy orbit. This orbit is indicated by the red lines and allows the mass to move in between stable points. This type of orbit is referred to as an inter-well orbit. All of the previously discussed behaviors are specific to a bistable type of nonlinear PEH, which is one of the most common configurations, although other types of nonlinear harvesters also exist.

The mechanical dynamics for a nonlinear system can be seen in Equation 1.4. The only difference being the replacement of the constant stiffness K with nonlinear stiffness term $K(x)$.

$$M\frac{d^2x}{dt^2} + c\frac{dx}{dt} + K(x)x + \alpha v_p = -M\frac{d^2y}{dt^2} \tag{1.4}$$

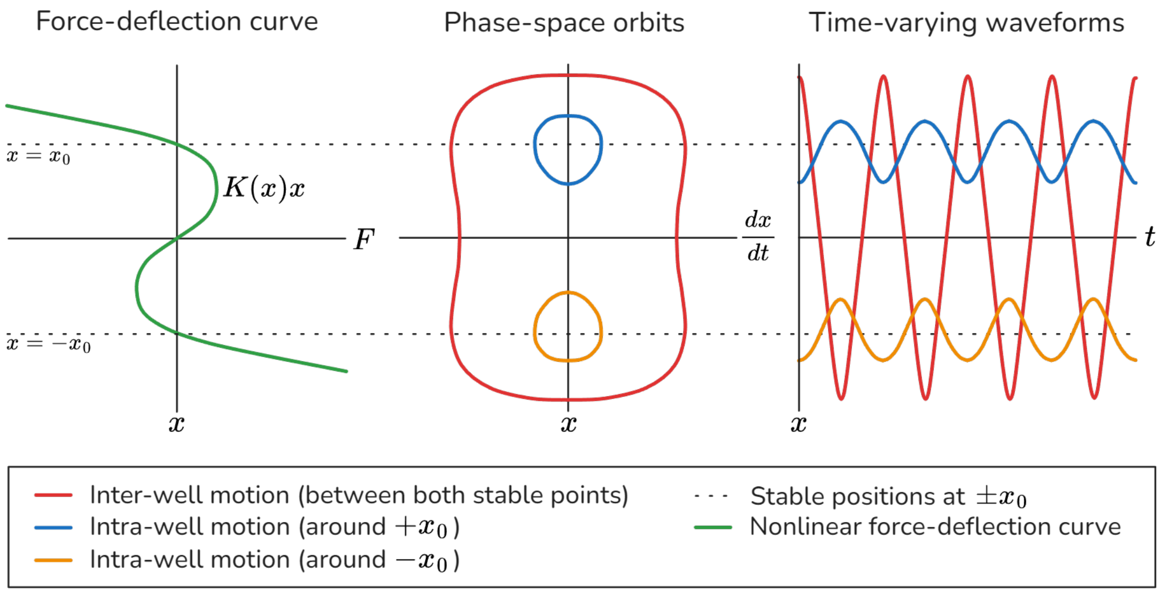

Figure 1.5: The force deflection curve combined with three different phase-space orbits and their accompanying time-varying waveforms of a nonlinear system.

The Force Voltage Factor

The force voltage factor α can be determined by measuring the maximum voltage and displacement, as outlined in Section A.1, giving the relationship

$$\alpha = \frac{V_{\text{OC}}}{X_{\text{OC}}} C_p. \tag{1.5}$$

Where V_{OC} represents the open-circuit voltage measured at maximum displacement, and X_{OC} denotes the open-circuit displacement also measured at its maximum.

The Electromechanical Coupling Coefficient

The electromechanical coupling coefficient quantifies the efficiency with which a piezoelectric harvester converts electrical energy into mechanical energy and is defined as

$$k_m^2 = \frac{E_{\text{elec}}}{E_{\text{mech}}}, \tag{1.6}$$

where E_{elec} is the electrical energy in the system and E_{mech} is the mechanical energy in the system. In a linear PEH, the electromechanical coupling coefficient can also be expressed as

$$k_m^2 = \frac{\alpha^2}{KC_p}. \tag{1.7}$$

Nonlinear harvesters do not have a simple constant electromechanical coupling coefficient. In these cases the expedient electromechanical coupling coefficient can be used in its place [5]. This coefficient can be taken by linearizing the system at one of its stable positions. This does mean the expedient electromechanical coupling coefficient only describes energy transfer for small oscillations around the stable position, making it unsuitable for describing energy conversion of bistable systems in a general sense. However, in many cases, it is still used as a metric for comparing different configurations.

The derivation and underlying assumptions of the expedient electromechanical coupling coefficient can be found in Section A.2.

1.2.3. The Challenges for PEH Circuitry

The previous section discussed how vibrational energy is converted to electrical energy. This section discusses the intricacies of using this electrical energy to power actual electric devices. The right side of Figure 1.3 shows an equivalent circuit model of the piezoelectric patch.

This equivalent circuit is based on a current source combined in parallel with a capacitor. This models the rate of charge buildup on the electrodes of the piezoelectric patch due to changes in stress caused by the velocity of the mass. Only a part of the current generated in this manner moves through the load Z_l. This is where the first issue becomes apparent, namely that the source impedance is highly capacitive. This can result in a significant portion of the alternating current simply charging and discharging the capacitor C_p, meaning it does not contribute to power transfer to the load Z_l.

This type of power is referred to as reactive power, while the power that is dissipated by the load is referred to as active power. Reactive power is created in this case when the current of the source and the voltage across the load do not have the same phase. Typically, one would reduce the reactive power by matching the source impedance to the load impedance. In this circuit example, that would mean compensating for the capacitive source by making the load more inductive. This is, however, not a practical solution in most PEH systems. The reason is twofold: Firstly, the inductance needed varies with different excitation frequencies. This means that, by choosing a constant inductance value, one would not be able to adapt to changes in ambient vibration frequencies or vibrations that are more complex than simply one harmonic frequency [6]. Second, the inductance required to counterbalance the capacitance would need to be impractically large in most cases.

Another important element is the need for the alternating current from the PEH in to be converted into direct current. This is needed since most devices can not run on an alternating current source.

1.2.4. The Standard Energy Harvesting Circuit

The most basic method of extracting energy from a PEH is using the Standard Energy Harvesting (SEH) circuit. The SEH circuit consists of a Full Bridge Rectifier (FBR) followed by a smoothing capacitor. It is a common circuit in a wide variety of fields that require the conversion from alternating to direct current. The circuit itself and a qualitative representation of its behavior can be seen in Figure 1.6. Its functioning can be described in the following way:

1. When the piezoelectric material deforms, it generates a charge on the electrodes. This is modeled as a current source i_p that moves charge into the piezoelectric capacitor C_p, which increases the voltage v_p. As more charge is generated, v_p keeps rising.
2. v_p rises until it exceeds the voltage after the rectifier, v_r (assuming ideal diodes). At this point, the diodes in the FBR start conducting, and the generated charge flows into both the smoothing capacitor C_r and the load Z_l.
3. As the deformation reaches its maximum, the direction reverses, causing the charge to flow in the opposite direction. This is reflected by i_p changing direction, discharging C_p instead of charging it.
4. v_p continues to drop until it falls below the negative of v_r. When this happens, the diodes in the FBR conduct again, and the charge flows into C_r and Z_l once more. This cycle repeats each time the deformation changes direction.

As explained, the piezoelectric current i_p charges and discharges the piezoelectric capacitor C_p. There is only power transfer to the load when the piezoelectric voltage v_p reaches a point where the FBR starts to conduct. While the SEH circuit does successfully create a direct current source for the load, it has the reactive power issue as discussed in Section 1.2.3 remains. This reactive power can be seen in Figure 1.6 as a difference in phase between the piezoelectric current i_p and the piezoelectric voltage v_p.

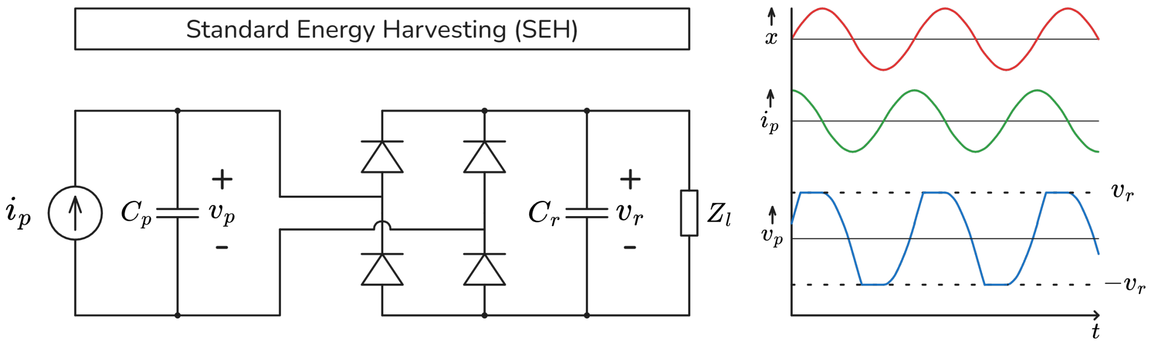

Figure 1.6: The SEH circuit combined with an illustration of relative waveforms showing the relationships between displacement (x), piezoelectric current (i_p), and piezoelectric voltage (v_p) over time (t).

1.2.5. Electrically-Induced Stiffness and Damping

The influence of the extraction circuit on the dynamics of the PEH can be characterized in two factors, as established by [5], [7], [8]. These factors are the electrically-induced stiffness and the electrically-induced damping. Electrically-induced stiffness is when the extraction circuitry acts in such a way as to create additional stiffness in the mechanical domain. An example of this would be simply to keep the PEH in an open-circuit condition. In this case the voltage on the piezoelectric material is proportional to the displacement assuming no losses. Since the force caused by the electrical dynamics is also proportional to the voltage, a direct linear relationship between displacement and force is established. This relationship resembles mechanical stiffness.

Electrically-induced stiffness can be seen in the electrical domain as reactive power. Subsection 1.2.3 outlines the issues with having reactive power in the harvesting circuit. However, one cannot simply make the assertion that limiting the amount of reactive power is always the best option. This is because changing the reactive power changes the electrically induced stiffness, which on its turn can positively effect the mechanical dynamics. In the case of a linear harvester for example, a change in stiffness can result in a change of the resonance frequency and thus can drastically impact the harvestable output power. This means that tweaking the electrically-induced stiffness can be an important part of maximizing power extracted from a PEH.

Electrically-induced damping occurs when the extraction circuitry acts in such a way as to create additional damping in the mechanical domain. This happens when the circuitry causes the current from the piezo element and the voltage across it to be in phase. In this case, power is dissipated in the electrical domain. This type of power can be used to supply loads and is referred to as active power. Tweaking the electrically-induced damping is an important part of maximizing the power extracted from a PEH.

Different energy extraction circuits exhibit distinct time-dependent behaviors in terms of electrically-induced damping and stiffness. The degree of damping and stiffness observable from the mechanical domain varies dynamically over time. This variation is influenced by two primary factors: the inherent dynamics of the extraction circuitry and the electromechanical coupling coefficient of the piezoelectric system. It is important to note the extraction circuit can change the electrically-induced damping and stiffness only to the degree the electromechanical coupling allows. A stronger electromechanical coupling coefficient means extraction circuit can have more influence on the dynamics of the mechanical domain, since it can generate greater electrically-induced damping and stiffness [9].

1.3. Problem Statement

In order to broaden the frequency range from which energy can be harvested, nonlinear PEH systems are becoming increasingly common. However, these nonlinear systems are inherently difficult to use for the evaluation of energy extraction circuitry. A prominent example of nonlinearity is the bistable harvester, which is shown in this work to exhibit chaotic behavior even when subjected to identical mechanical inputs. As a result, evaluating energy extraction circuits using real PEH devices leads to inconsistent results.

Currently, most researchers rely on custom-built linear PEH systems for experimental circuit evaluation. While the linear dynamics alleviate the chaotic behavior, this approach does not align with the broader trend toward nonlinear harvesters. Additionally, the use of custom PEH devices makes replication of results nearly impossible unless the materials, fabrication process and input excitation conditions are exactly duplicated, which is not done in practice.

Another drawback of using custom PEH systems is the lack of flexibility in key parameters. Characteristics such as the piezoelectric capacitance, which strongly influence the relative performance of energy extraction circuits, cannot be easily adjusted. Exploring different configurations would require physically rebuilding the harvester for each set of parameters, which is highly impractical.

These limitations motivate the development of a configurable PEH emulator that supports repeatable and configurable testing of energy extraction circuits under realistic electrical conditions. Such a system would allow researchers to consistently evaluate circuit performance across a range of PEH characteristics without being constrained by the behavior of real harvesters.

1.4. State-of-the-Art Overview

A wide range of circuit topologies have been proposed to improve the efficiency of PEH systems. These include synchronized switch harvesting on inductor and synchronous electric charge extraction circuits, both of which aim to increase active power transfer by minimizing voltage-current phase mismatch through techniques such as voltage inversion or charge redirection [10], [11]. Complementary control strategies such as maximum power point tracking are also used to further optimize extraction under varying load and excitation conditions [12].

While the design of energy extraction circuits has matured significantly, their experimental evaluation remains inconsistent. As described in Section 2.4, methods such as external excitation using shakers [13]–[15] and direct excitation using magnetic or mechanical actuation [16]–[18] are commonly used. However, both approaches depend heavily on the mechanical and material properties of the specific PEH device being tested, which introduces significant variability. These challenges are exacerbated when dealing with nonlinear PEHs, such as bistable harvesters, which may exhibit chaotic or hysteretic behavior under minor changes in input excitation [19], [20].

The consequence is that energy extraction circuits evaluated on different physical PEHs, or even the same PEH under slightly different conditions, can yield results that are difficult to reproduce or compare. At the point of writing, no research appears to have been done regarding how to fully decouple circuit testing from harvester variability.

In contrast, other energy harvesting domains have adopted emulator-based approaches to address similar evaluation challenges. In photovoltaics (PV), programmable PV emulators are commonly used to mimic the current-voltage characteristics of solar cells, enabling controlled, repeatable testing of power management circuits under a wide range of simulated conditions [21], [22]. Likewise, in thermoelectric energy harvesting, thermal emulators have been developed to replicate the electrical response of thermoelectric generators (TEGs) across programmable temperature profiles [23].

These emulator systems allow circuit performance to be evaluated independently of the variability inherent to physical harvesters. They also enable parameter sweeps that would be impractical with physical devices. However, no equivalent hardware emulator currently exists for PEH systems. As identified in Section 2.6, this absence represents a critical gap in the current research landscape. The lack of a configurable, repeatable PEH emulator has limited the ability to benchmark energy extraction circuits under controlled conditions.

This thesis addresses that gap by presenting a dedicated emulator for piezoelectric energy harvesters, capable of replicating real PEH output behavior while offering configurability, repeatability, and compatibility with the current state-of-the-art energy extraction circuits.

1.5. Research Objectives and Scope

The primary objective of this thesis is to investigate whether it is feasible to build a hardware emulator that replicates the electrical output behavior of PEH systems. To the best of the author's knowledge, no such emulator has been developed before, despite the widespread use of emulator-based testing platforms in related energy harvesting domains such as photovoltaics and thermoelectrics. This work explores the design and realization of a custom emulator architecture which is suitable for PEH system emulation and identifies the limitations encountered in the practical implementation.

In addition to evaluating feasibility, this thesis aims to design and implement a prototype emulator capable of supporting repeatable evaluation of energy extraction circuits. Specifically, the emulator should reproduce PEH-like electrical behavior, offer configurable output impedance, and support high peak voltages and currents compatible with fast-switching extraction techniques such as SSHI and SECE.

To demonstrate the usefulness of the emulator, a secondary objective is to validate its output behavior by comparing it to that of a real PEH device under various operating conditions. This is done by assessing the emulator's accuracy across different load resistances and excitation amplitudes, as well as evaluating its suitability for use with nonlinear extraction circuits and representative laboratory equipment.

The scope of this work is limited to the electrical emulation of PEH systems based on pre-recorded voltage waveforms under open-circuit conditions. Mechanical dynamics and back-coupling effects are not modeled. The emulator is intended for laboratory use and does not aim to replicate all physical phenomena present in real piezoelectric materials. Furthermore, impedance matching is implemented using discrete analog components rather than digitally synthesized models, in order to ensure real-time responsiveness. This thesis establishes a baseline hardware platform and experimental methodology that can be extended in future work to support more advanced impedance modeling and improve emulation accuracy.

In summary, the central research question addressed by this thesis is the following: ”Is it technically feasible to develop a hardware emulator that replicates the electrical behavior of real PEH systems to support repeatable circuit evaluation?” Rather than optimizing for performance or comparing against existing solutions, which do not currently exist for piezoelectric energy harvesters, this work seeks to establish a functioning emulator design baseline and to characterize the practical trade-offs involved in such systems.

1.6. Thesis Structure

This thesis is structured as follows:

- **Chapter 2** reviews energy extraction circuits for PEH systems, experimental evaluation methods, and the absence of emulator-based testing in current literature.
- **Chapter 3** presents the design and implementation of the proposed PEH emulator, including architectural choices, circuit design, and supporting simulations.
- **Chapter 4** experimentally validates both the emulator's standalone behavior and its ability to replicate the output of a real PEH system across varying conditions.
- **Chapter 5** analyzes emulator performance and limitations, and outlines open questions and future research opportunities.
- **Chapter 6** summarizes the contributions of the work, reflects on its broader impact, and concludes the thesis.

2

Literature

This chapter expands upon the background provided in chapter 1, specifically addressing the challenges identified in Section 1.2.3 regarding circuitry for PEH systems. The following sections explore more advanced circuit solutions and techniques designed to optimize energy extraction across, addressing the limitations inherent in standard energy harvesting circuits.

Although the main focus of this thesis is on developing a PEH emulator, a substantial part of this chapter reviews energy extraction circuits. The reason for this is that these circuits ultimately define the operational context of the emulator: they determine what electrical behavior the emulator must be able to reproduce and under what conditions it should operate. Understanding the requirements and challenges of state-of-the-art extraction techniques ensures that the emulator is designed to be compatible with real-world energy extraction circuits.

Initially, the concept of Synchronized Switch Harvesting on Inductor (SSHI) is examined, detailing its operating principles, advantages in maximizing output power, and practical limitations. This technique notably enhances performance by improving voltage-current phase alignment through strategic voltage inversion, although it introduces increased complexity and reliance on inductors. Complementary to SSHI, the discussion then introduces Synchronous Electric Charge Extraction (SECE) circuits, highlighting their reduced load dependency and decreased design complexity compared to SSHI-based solutions.

Additionally, this chapter explores critical considerations in implementing switch control mechanisms, emphasizing the challenges associated with achieving self-starting operation and reliable switching. Both analog and digital solutions are analyzed, with particular emphasis on self-powered electronic breakers that enable autonomous switching.

Further, this chapter addresses methods for evaluating the performance of PEH circuits through experimental testing. It reviews current practices involving external and direct excitation methods and underscores inherent difficulties, particularly with nonlinear harvesters exhibiting chaotic dynamics and hysteresis. The difficulties in experimental evaluation of energy extraction circuits using PEH systems is contrasted with solutions for tackling this difficulty employed in photovoltaic and thermoelectric energy harvesting domains.

The chapter concludes by identifying key gaps in current literature, particularly the absence of a standardized emulator capable of accurately replicating the electrical characteristics of PEH systems for consistent, repeatable testing of extraction circuits. This identified gap establishes the motivation for developing the piezoelectric emulator, the central focus of subsequent chapters.

2.1. Synchronized Switch Harvesting on Inductor

Originally energy extraction from PEH was mainly done using the SEH circuit as discussed in Section 1.2.4. The next sections explore the first circuits aiming to improve the energy extraction performance compared to SEH circuits.

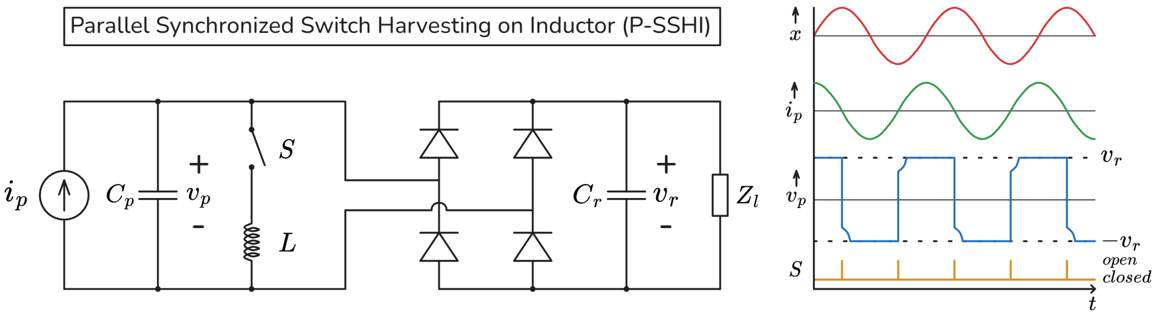

Figure 2.1: The P-SSHI circuit combined with an illustration of relative waveforms showing the relationships between displacement (x), piezoelectric current (i_p), piezoelectric voltage (v_p), and the state of the switch (S) over time (t).

2.1.1. The Workings of Synchronized Switch Harvesting on Inductor

In a search for methods to increase the overall output power Guyomar et al. proposed a novel power flow optimization technique, which is called Parallel Synchronized Switch Harvesting on Inductor (P-SSHI) [24]. The proposed technique relies on an electrical switch device connected to the piezoelectric element in combination with an inductor. The circuit itself and a qualitative representation its behavior can be seen in Figure 2.1. Its functioning can be described in the following way:

1. Initially, the piezoelectric capacitor C_p is charged to a voltage v_r. As mechanical deformation of the PEH occurs, charge flows directly from C_p to the smoothing capacitor C_r and the load Z_l, while the switch S remains closed.
2. When the displacement direction reverses and the piezoelectric current i_p changes polarity, the piezoelectric voltage v_p reaches its peak and begins to decrease. At this instant, the switch S is opened.
3. Upon opening the switch, charge stored in C_p begins to flow through the inductor L, transferring charge from one electrode of C_p to the other. The the movement of charge through the inductor creates a magnetic potential energy due to the formation of a changing magnetic field. This energy reaches its maximum when v_p reaches zero volts.
4. The stored magnetic potential energy in the inductor is then converted back into electrical energy, resulting in additional extraction of charge from C_p. This means a further decrease in v_p, which now transitions from zero volts to a negative potential approaching $-v_r$.
5. Once all stored magnetic energy has been depleted the charge transfer is complete and no further current flows through the inductor. At this point, the switch opens, and the process repeats with opposite polarities during the next half-cycle of mechanical excitation.

A similar technique, called Series Synchronized Switch Harvesting (S-SSHI), has also been proposed by Taylor et al. [25]. This technique relies on the series connection of the switch and inductor rather than the parallel connection in P-SSHI. The circuit itself and a qualitative representation of its behavior can be seen in Figure 2.2. Its functioning can be described in the following way:

1. Initially, charge accumulates on the piezoelectric capacitor C_p, increasing the voltage v_p. As more charge is generated, v_p continues to rise. The switch S remains open during this phase.
2. When the displacement direction reverses and the piezoelectric current i_p changes polarity, the voltage v_p reaches its peak and begins to decrease. At this instant, the switch S is closed to initiate voltage inversion.
3. Once the switch closes, charge starts flowing out of C_p through the inductor L and into the smoothing capacitor C_r and the load Z_l. The charge movement through the inductor generates a changing magnetic field, storing energy in the inductor as magnetic potential energy. This energy is maximized when v_p reaches the potential v_r.
4. The stored magnetic potential energy in the inductor is then converted back into electrical energy, extracting additional charge from C_p. This further reduces the piezoelectric voltage v_p below v_r.

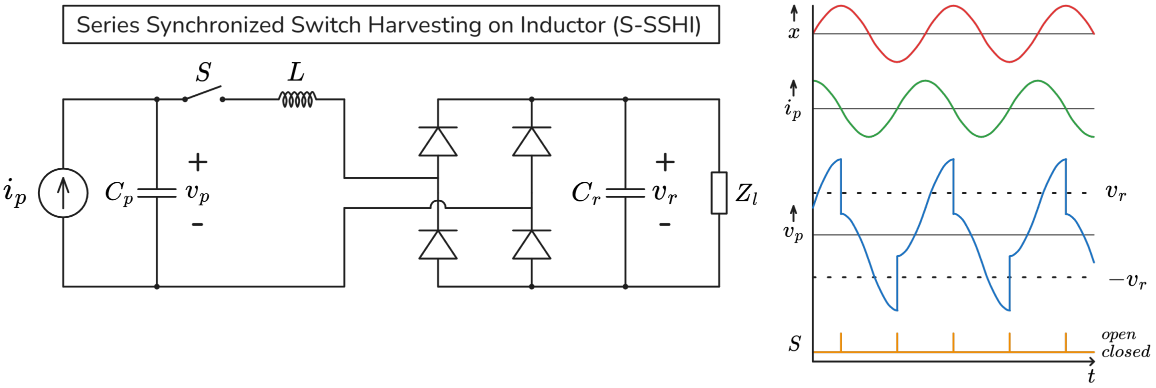

Figure 2.2: The S-SSHI circuit combined with an illustration of relative waveforms showing the relationships between displacement (x), piezoelectric current (i_p), piezoelectric voltage (v_p), and the state of the switch (S) over time (t).

5. When the charge transfer is complete and all magnetic potential energy in the inductor is depleted, no more current flows through the switch. At this point, the switch opens, and the process repeats in the opposite polarity during the next half-cycle of mechanical excitation.

2.1.2. The Advantages of Synchronized Switch Harvesting

SSHI enhances energy extraction efficiency by inverting the voltage across the piezoelectric element when the piezoelectric current changes direction. The inverting of voltage in this manner is referred to as bias flip. This process improves the phase alignment between voltage and current, thereby minimizing reactive power losses. The reduction in reactive power increases the proportion of active power transferred to the load. SSHI-based techniques have demonstrated power extraction improvements of over 900% compared to the SEH circuit [24]. This enhancement is most notable in PEH systems with a low electromechanical coupling factor. As the coupling factor increases, the performance difference between SSHI and SEH diminishes [26].

2.1.3. The Disadvantages of Synchronized Switch Harvesting

One of the main drawbacks of using the SSHI technique is the need for an inductor, which can increase cost and the amount of space required [27]. Recent developments have aimed at minimizing the increase in cost and space requirements by performing bias flip using a set of capacitors instead of inductors. This technique is referred to as synchronized switch harvesting on capacitors (SSHC) [28]. One of the drawbacks of this technique is the increase in circuit complexity.

Another drawback with SSHI-based techniques is the dependence of power transfer on the load Z_l [29]. Different SSHI configurations exhibit distinct optimal load resistances, which must be matched carefully to achieve maximum power transfer. For instance, comparative studies have shown that P-SSHI circuits typically reach peak output power at significantly higher load resistances than S-SSHI circuits. One such study reported optimal resistances in the range of 20 kΩ for P-SSHI and around 2 kΩ for S-SSHI [30]. The exact optimal load values do not only depend on the type of SSHI circuit used but also on the specific PEH implementation and the excitation conditions.

2.1.4. Maximum Power Point Tracking

Since tweaking the load for optimal power transfer is impractical in most applications, often a separate circuit is used to create the optimal load conditions for the SSHI circuit. This type of circuit is known as a Maximum Power Point Tracking (MPPT) circuit. The next sections discuss the three main types of MPPT used.

Perturb-and-Observe

The Perturb-and-Observe (P&O) MPPT method operates by making adjustments to the load impedance and observing the resulting change in harvested power. If the power increases, the adjustment continues in the same direction; if power decreases, the adjustment is reversed. By doing this repeatedly the system is able to converge toward the maximum power point over time. However, it introduces oscillations around the optimal point and can be slow to adapt to rapidly changing environmental conditions [31]. Another drawback of this method is the computational overhead. Since it requires continuous power measurements and iterative adjustments, it consumes additional energy, making it less suitable for applications with limited power availability [12].

Fractional Open Circuit Voltage

The Fractional Open-Circuit Voltage (FOCV) MPPT method [32] estimates the optimal operating voltage as a fixed fraction of the open-circuit voltage (V_{OC}). Using this simple fractional relationship can allow for a power-efficient way to approximate the maximum power point. The disadvantage of this method is that, in order to measure V_{OC}, the circuit must periodically disconnects the PEH from the load. This interrupts power delivery and thus reduces overall energy transfer.

Fractional Normal Operating Voltage

The Fractional Normal Operating Voltage (FNOV) MPPT method [33] improves upon FOCV by estimating the maximum power point voltage as a fraction of the normal operating voltage rather than the open-circuit voltage. This approach eliminates the need to periodically disconnect the harvester, allowing for continuous power transfer. This technique can only be applied on extraction circuit methods where the open-circuit voltage can be estimated based on the voltage levels on the piezoelectric capacitor during operation of the extraction circuitry. This is the case for S-SSHI since it disconnected from the load most of the time, but this is not the case for P-SSHI since the voltage on its piezoelectric capacitor is clamped by the voltage on the load. This means this technique is only usable for specific energy extraction circuit topologies while both P&O and FOCV do not have this limitation.

2.2. SECE

Another method used to extract more power out of PEH systems is by using the Synchronous Electric Charge Extraction (SECE) circuits [11]. The main difference between SECE and SSHI is their respective load dependence. The output power of SECE circuits is significantly less dependent on the load compared to SSHI. This lessens the need for combining SECE with an MPPT circuit to get maximum output power thus decreasing design complexity. The circuit itself and a qualitative representation its behavior can be seen in Figure 2.3. This figure contains two versions of the classical SECE circuit as well as the Optimized Synchronous Electric Charge Extraction (OSECE) circuit which requires one less diode in the power path reducing losses [34]. The functioning of SECE is largely similar to that of S-SSHI with the difference being the energy transfer from the PEH to the inductor or transformer happens by moving charge from one plate of the piezoelectric capacitor to the other instead of moving charge directly into the load.

2.3. Switch Control in Energy Extraction Circuits

In order to realize the previously discussed energy extraction circuit the switches featured in the designs need to be implemented and controlled to switch at the right time. This is a complex issue since the control mechanism of the switch is needed for the circuit to harvest energy but at the same time harvested energy is required for the system to operate its switch control mechanism. This is knows as the self-start problem. This section discussed different switch implementations as well as how they are controlled and how they tackle the self-start problem.

2.3.1. Start-Up Circuits and Digital Switch Control

One potential solution to the self-start problem is using start-up circuits. An example of such circuit can be seen in [10] where a separate piezoelectric patch is added inside the PEH and attached an SEH circuit. The SEH circuit does not rely on any switching based control and is implemented purely with passive components, making the ideal startup circuit. The energy from the startup circuitry can be used to power a switching based energy extraction circuit connected to the main piezoelectric patch in the PEH.

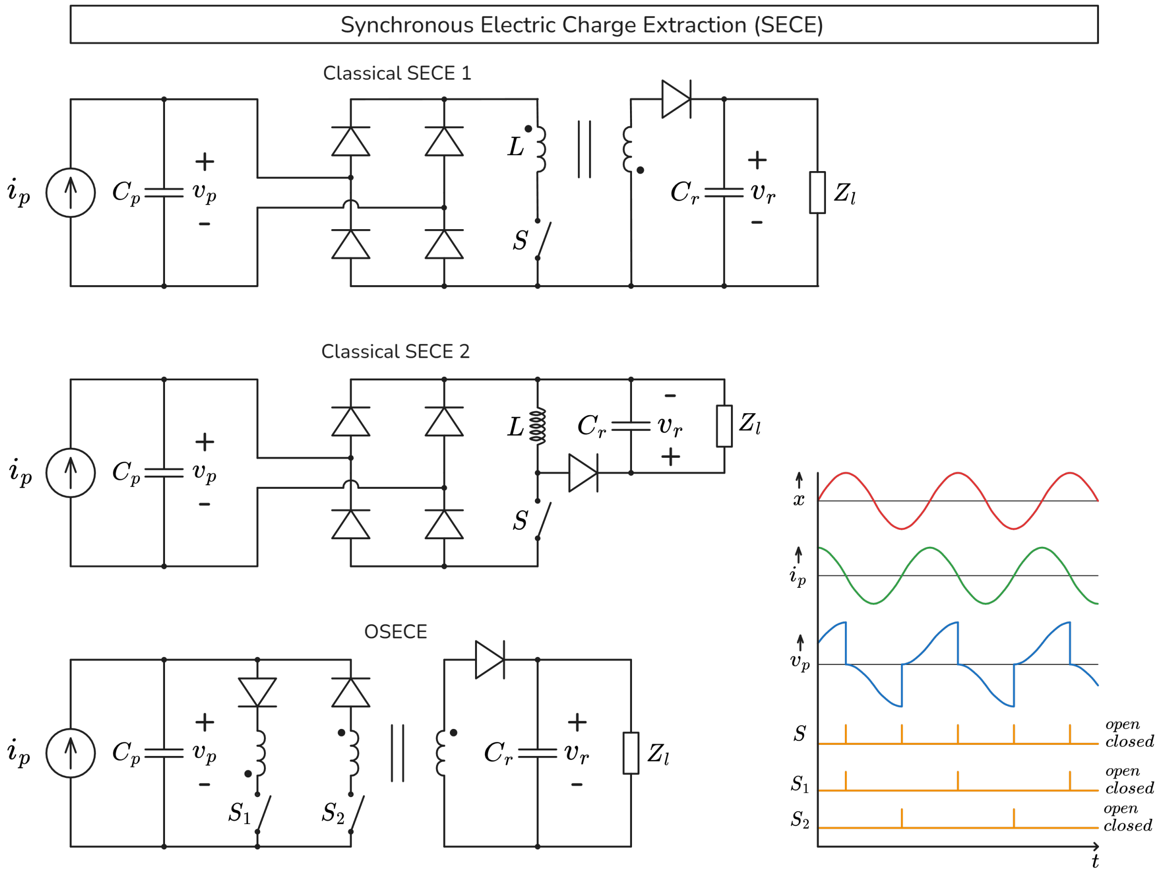

Figure 2.3: Three differing SECE circuits combined with an illustration of relative waveforms showing the relationships between displacement (x), piezoelectric current (i_p), piezoelectric voltage (v_p), and the state of the switch (S) over time (t).

Start-up circuits are required for energy extraction circuits that have their switch controlled via a digital control system such as a Micro controller Unit (MCU). Though the use of MCUs for switch control allows for complete freedom in terms of control algorithms, it often comes at the cost of increased power consumption. In the example given by [10] the control circuitry dissipated $328.8\,\mu\mathrm{W}$ which would make it infeasible for many PEH systems.

2.3.2. Envelope Detection and Analog Switch Control

A widely adopted implementation for handling both switch timing and self-starting issues is the self-powered electronic breaker [35]. The block diagram illustrating the circuit's operation along with the circuit itself is shown in Figure 2.4.

In this circuit, the components R_3, D_3, and C form the envelope detector. As the input voltage v_p increases, the voltage across C rises. During this phase, the base voltage of transistor T_2 remains higher than its emitter voltage, resulting in a non-conducting state for T_2. Consequently, transistor T_1 also remains non-conducting. This condition persists until the input voltage v_p begins to decline. As v_p decreases, the voltage across C retains its previous value until the potential difference between the base and emitter of T_2 exceeds the threshold voltage. At this point, T_2 enters its conducting state, allowing the charge accumulated on C to discharge through D_2, T_2, R_1, and T_1. At this point both T_1 and T_2 are in their conducting modes and the switch is considered open. This process is interrupted when the current through D_1 ceases, causing D_1 to stop conducting. The envelope detector's input can be filtered using the combination of R_3 and C. Additionally, R_1 and R_2 serve to limit bias currents, although they are often omitted in more recent designs [36]. Various modifications of this circuit topology exist, with each implementation differing slightly compared to the original.

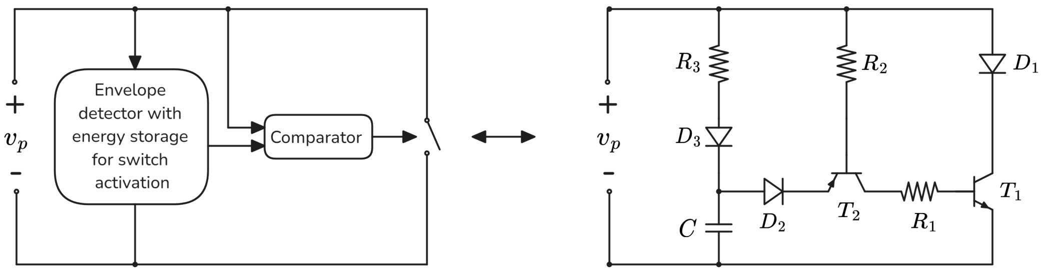

Figure 2.4: The positive switching variant of the electronic breaker [37].

Figure 2.4 shows only the breaker design meant to work on positive input voltage peak detection and switching, though this design can altered to work for negative input voltage peak detection and switching as well. In many cases switching at both positive and negative peaks is required. Figure 2.5 shows an example implementation of a slightly altered breaker implementation in an implementation of P-SSHI. Note that this breaker design can be used in a wide variety of energy extraction circuits including the ones mentioned earlier [26].

2.4. Evaluating Energy Extraction Circuit Performance

Typically new energy extraction circuitry is evaluated using a mix analytical methods, simulation and experimental testing. This section discusses the methods for experimental evaluation of energy extraction circuits.

2.4.1. Experimental Testing For Energy Extraction Circuits

This section explains the three main methods currently in use for experimental validation of energy extraction circuitry.

External Excitation Testing

A widely adopted approach for evaluating energy extraction circuitry involves subjecting a PEH to controlled vibrations, thereby generating an electrical output suitable for circuit testing. This method can be conceptualized as the manipulation of the external excitation (y), as illustrated in Figure 1.3. The way this is typically achieved is by mounting the base of the PEH onto an electrodynamic shaker [13]–[15].

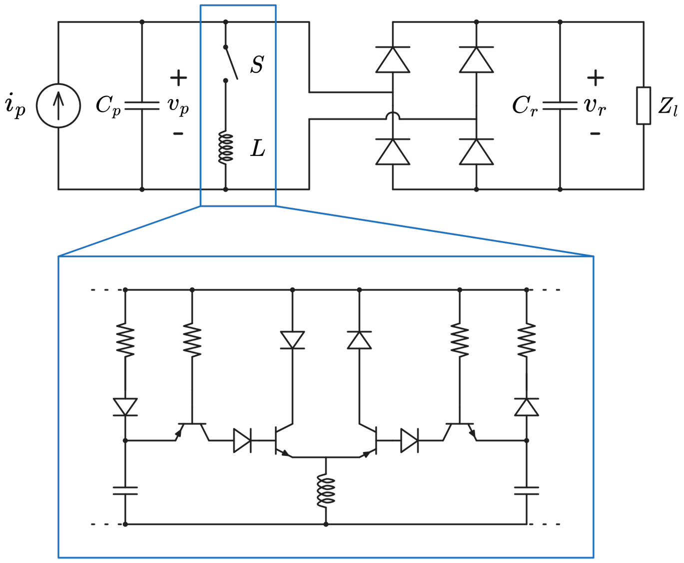

Figure 2.5: A P-SSHI circuit implemented using the electronic breaker [6].

Such a setup provides precise control over the input vibrations, enabling the replication of real-world mechanical excitation conditions.

However, employing external excitation to assess energy extraction circuits introduces a dependency on the dynamic mechanical characteristics of the specific PEH used. As a result, the measured performance of the energy extraction circuitry is influenced not only by the circuit itself but also by the particular PEH's mechanical behavior. Since different studies often utilize different PEH designs and configurations, direct comparison of circuit performance becomes challenging. Furthermore, in scenarios where the PEH exhibits strong nonlinear dynamics, its response may be chaotic in certain conditions, complicating comparisons even when the same harvester is used across multiple experiments. A more detailed discussion of this issue is presented in Section 2.5.

Direct Excitation Testing

Direct excitation, in contrast to external excitation that vibrates the base of the PEH, involves directly controlling the internal movement of the mass within the PEH. This method can be conceptualized as the direct manipulation of the mass displacement (x), as illustrated in Figure 1.3.

There are several techniques to achieve direct excitation. One commonly employed method is electromagnetic actuation, wherein a magnetic field generated by a coil is used to move a magnet attached to the internal mass [16], [17]. While this approach is relatively straightforward to implement, it offers limited precision compared to mechanisms that allow for direct mechanical actuation of the mass [18], [38].

Although direct excitation enables repeatable and controlled testing of energy extraction circuits, the limited availability and standardization of PEH devices used in such setups hinders the broader comparability of results across different research groups. This makes it difficult to benchmarking energy extraction circuits against each other using a consistent experimental framework.

2.4.2. Experimental Testing for Energy Extraction Circuits in Different Fields

The difficulty in comparing different energy extraction circuits is by no means exclusively an issue in piezoelectric vibration energy harvesting. That being said other energy harvesting related fields do have solutions for this issue. An example solution for this issue in the context of Photovoltaic (PV) energy harvesters would be making use of an emulator [21], [22]. The PV emulator is a nonlinear power supply capable of producing the current-voltage (I-V) characteristic of the PV module. It does this by measuring the I-V characteristics of a PV source, saving the characteristics to memory and emulating them as an energy source. This allows for repeatable testing conditions that are not dependent on the characteristics of the PV harvester.

Similarly, in the field of thermoelectric energy harvesting, thermal emulators have been developed to mimic the electrical output characteristics of thermoelectric generators (TEGs) exposed to different temperature gradients. These emulators are capable of producing programmable temperature profiles across a TEG module, enabling precise and repeatable experimental conditions [23]. This allows researchers to decouple extraction circuit performance from the physical thermal behavior of the TEG.

The use of emulators in various energy harvesting domains offers a promising approach to enhance the consistency and reproducibility of experimental evaluations, both within individual studies and across different research groups. In the field of piezoelectric energy harvesting, the development of comparable emulator systems to those in other energy harvesting fields could yield similar advantages if successfully implemented.

2.5. Bistable Harvester Dynamics

Building upon the discussion in Section 1.2.2, this section explores the dynamic behavior of energy harvesters with nonlinear stiffness, with particular emphasis on chaotic motion and hysteresis. In order to illustrate these phenomena, the bistable configuration is chosen as an example of a harvester with nonlinear dynamics.

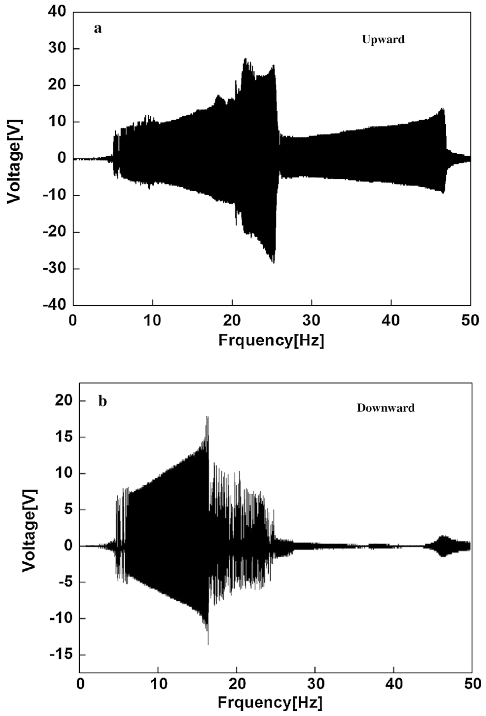

Figure 2.6: The output voltages of an example bistable system when changing the excitation frequency as shown in [19]. Here figure **a** shows an upward sweep and figure **b** shows a downward sweep.

One example of such behavior can be seen in the experimental work by Yao et al. [19]. The results, shown in Figure 2.7, include time-domain waveforms and phase portraits for different excitation frequencies. These plots show how the system transitions between periodic and chaotic motion with only small changes in frequency, highlighting the system's sensitivity to input conditions.

Further evidence of this complex behavior is shown in Figure 2.6, which presents the frequency response of the same system. The figure clearly demonstrates hysteresis: the output at a given input frequency depends not only on that frequency but also on the system's previous state. As a result, the harvester does not produce a consistent output for the same input frequency, which makes both analysis and comparison more challenging.

Similar hysteresis has also been observed when varying excitation amplitude. For example, Stanton et al. [20] reported results showing hysteretic behavior when adjusting the excitation acceleration, showing that this effect is a common feature of bistable harvester dynamics.

All of the results discussed were obtained using single-frequency excitation while the PEH was connected to a simple resistive load. Introducing additional nonlinearity such as through the use of energy extraction circuits like the previously discussed SSHI or SECE methods may further increase the complexity and unpredictability of the harvester's response. Similarly, replacing the single-frequency input with multi-modal or broadband excitation signals better reflecting real operating conditions of harvesters could lead to even more irregular and less predictable behavior. As a result, conducting repeatable and reliable evaluations of energy extraction circuits using nonlinear harvesters presents a significant challenge.

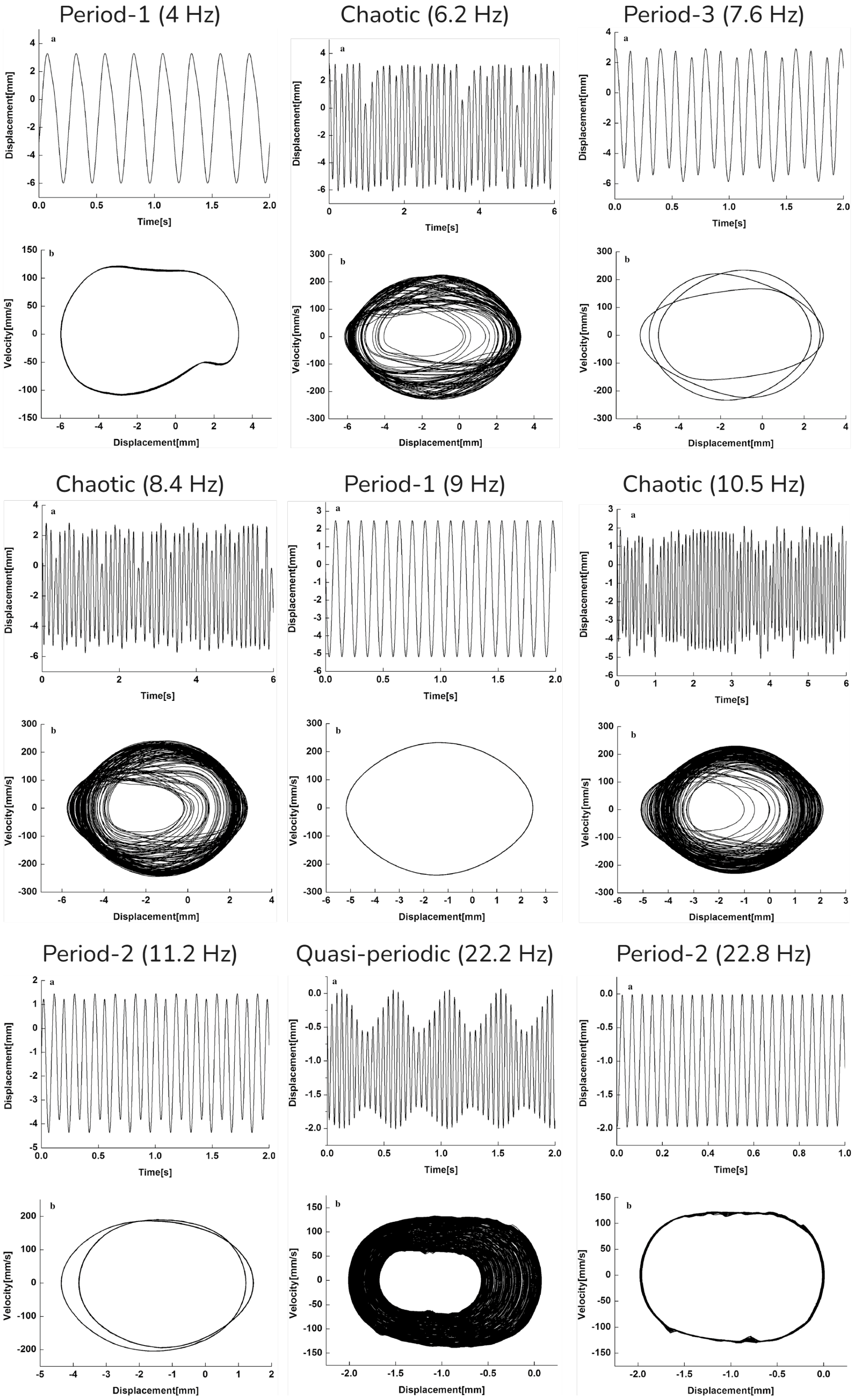

Period-1 (4 Hz)

Chaotic (6.2 Hz)

Period-3 (7.6 Hz)

Chaotic (8.4 Hz)

Period-1 (9 Hz)

Chaotic (10.5 Hz)

Period-2 (11.2 Hz)

Quasi-periodic (22.2 Hz)

Period-2 (22.8 Hz)

Figure 2.7: The motion patterns of an example bistable harvester in terms of the waveforms and phase portraits for a constant external excitation amplitude and for different external excitation frequencies as shown in [19]. The titles above the plots indicates the type of motion.

2.6. Summary and Identified Gaps

This section summarizes the main findings from the literature and outlines the key gaps that motivated the development of the PEH emulator.

As outlined in Sections 2.1–2.3, a variety of methods have been proposed to enhance the energy extracted from PEH systems. These typically involve nonlinear interface circuits that use timed switching of inductors to reduce the phase difference between the piezoelectric voltage and current, thereby increasing the amount of active power transferred to the load.

Section 2.4 reviewed the experimental approaches used to evaluate such energy extraction circuits and highlighted the difficulties in comparing results across studies due to variations in PEH systems. Further challenges were illustrated in Section 2.5, where even the use of the same harvester, particularly one with bistable dynamics, can result in inconsistent electrical output behavior due to the system's sensitivity to small variations in excitation and its hysteretic behavior. These nonlinear effects make it difficult to perform repeatable evaluations of energy extraction circuits using actual PEH devices.

In contrast, as discussed in Section 2.4.2, other energy harvesting domains such as photovoltaics and thermoelectrics have addressed similar challenges by developing emulators that replicate the electrical behavior of their respective harvesters. These emulators allow for consistent and repeatable testing of energy extraction circuits, independent of the physical harvester's behavior. At present, no equivalent solution appears to exist for piezoelectric harvesters. This gap in the literature has motivated the development of the PEH emulator, which is introduced and explored in the following chapters.

3

PEH Emulator Design

This chapter outlines the full design process of the PEH emulator, from the initial formulation of functional and technical requirements through to circuit-level implementation and prototype realization. The objective is to construct a hardware system that can replicate the electrical behavior of real PEH systems with build in repeatability, and configurability. Key design decisions are motivated by the need to accurately reproduce voltage and current profiles under a wide range of load and excitation conditions while maintaining compatibility with typical laboratory infrastructure. The chapter first defines the system-level requirements and constraints, followed by a discussion of the underlying architecture. The implementation details are then presented, covering both the internal analog circuitry and supporting instrumentation. Finally, simulations and physical prototyping are used to validate that the system meets its performance targets and is ready for experimental evaluation.

3.1. Emulator Requirements and Specifications

This section defines the operational expectations and design constraints that the emulator must meet to replicate the electrical behavior of real PEH systems. The functional requirements outline the capabilities the system must provide to ensure accurate and reliable energy extraction circuit evaluation. These are then translated into technical specifications, which serve as a foundation for subsequent design and implementation decisions.

3.1.1. Functional Requirements

The piezoelectric emulator must accurately replicate the electrical behavior of real PEH systems. To achieve this, the following functional characteristics have been identified as essential:

- **Accurate Emulation of PEH Electrical Characteristics**: The emulator should reproduce voltage and current profiles consistent with actual piezoelectric harvesters across the intended frequency bandwidth, including both linear and nonlinear operational regimes.
- **Adaptability to Various PEH Systems**: The system must support the changing of critical system parameters such as the piezoelectric capacitance C_p to better emulate different types of PEH harvester implementations.
- **Wide Frequency Range Operation**: The emulator needs to operate effectively across a broad frequency spectrum, thus accommodating typical operational conditions of various PEH systems.
- **Real-Time Responsiveness**: Rapid and accurate response to changes in emulation parameters and circuit loading conditions is required. The emulator should dynamically respond in real-time to ensure representative emulation of transient behaviors.
- **Measurement and Data Acquisition**: The system should allow for measurement capabilities including real-time voltage, current, and power monitoring.

- **Reliability and Repeatability**: The emulator should provide highly repeatable and stable test conditions to facilitate comparative analyses across multiple experimental trials and circuit configurations.
- **Ease of incorporation in existing lab setups**: The emulator could require additional equipment to operate with the caveat being that this additional equipment should be commonly found in most electronic labs (e.g., power supplies, waveform generators, current and voltage measurement equipment).

3.1.2. Technical Specifications

Based on the functional requirements previously defined, the piezoelectric emulator (PE) must fulfill the following technical specifications:

- **Voltage Output Range**: The emulator shall provide a voltage output ranging from $0\,\mathrm{V}$ up to at least $\pm 25\,\mathrm{V}$ peak-to-peak in open circuit condition. $\pm 25\,\mathrm{V}$ peak-to-peak strikes a balance between the high voltages some PEH systems are able to produce and the limitations of analog front ends combined with the typical $30\,\mathrm{V}$ limit of lab power supplies.
- **Current Capability**: The system must be able to source and sink currents of up to $3\,\mathrm{A}$. This requirement arises from the behavior of certain energy extraction circuits, such as SSHI and SECE, which can draw high peak currents when switching their inductors. This is particularly true for implementations that use lower inductance values to save space, or piezoelectric patches with relatively high capacitance. Based on values observed in the literature, the worst-case scenario assumes a capacitance (C) of 1 μF and an inductance (L) of 100 μH. Under these conditions, a peak current (I_{peak}) of 3 A corresponds to a maximum capacitor voltage (V_C) calculated as $V_C = I_{\text{peak}}/\sqrt{C/L}$, which yields $30\,\mathrm{V}$. This value aligns with the voltage requirement discussed earlier.
- **Frequency Bandwidth**: The emulator should operate reliably within a frequency range of at least $1\,\mathrm{Hz}$ to $1000\,\mathrm{Hz}$, covering the majority of practical piezoelectric harvester applications as outlined in the frequency of potential sources of vibration as covered in [39].
- **Input and Output Interfaces**: An analog output is required for interfacing with external energy extraction circuitry. Additionally outputs should be available for measuring output current and voltage.
- **Output loading**: Capacitive loading, for example by attaching long cables to the output, should not cause instability of the emulator output. The worst-case capacitive load is considered to be $1\,\mathrm{nF}$.
- **Thermal Management**: The design should incorporate adequate thermal management to ensure reliable performance without overheating, under continuous operation within room temperature ($24\,°\mathrm{C}$) environments.
- **Physical Dimensions**: The emulator design should fit within standard laboratory equipment dimensions for ease of integration into existing test setups.

3.2. Back Coupling Effects of Electrical Loading

A typical emulator relies on a model to predict how input parameters, such as the mechanical excitation applied to the PEH, influence electrical outputs like voltage and current. However, as previously discussed in Section 1.2.5, the interaction between the PEH and the electrical load is inherently bidirectional. This means the dynamics of the PEH influence the behavior of the load, and simultaneously, the dynamics of the load influence the mechanical behavior of the PEH.

Implementing a model that accurately captures this interaction poses two main challenges. First, the nonlinear dynamics involved in PEH systems are complex and chaotic. These systems are highly sensitive to minor variations in both external excitations and internal system parameters. Modeling these nonlinearities accurately would significantly increase the complexity of the emulator. Second, and more importantly, precisely emulating the nonlinear and hysteretic dynamics of a real PEH system would inherently replicate the very issue that the emulator aims to resolve, namely the difficulty in creating reproducible and consistent test conditions. Consequently, the piezoelectric emulator does not take into account the effects of the electrical domain on the mechanical domain (back-coupling effects).

By making this design choice, no modeling is required, and the emulator can simply replay output signals from existing PEH systems without taking into account how the load characteristics might influence the PEH dynamics. For systems in which the back-coupling effects are minimal (such as systems with low electromechanical coupling factors), evaluations using the emulator could fully replace traditional testing with actual PEH devices, ensuring consistent and replicable conditions. Conversely, for systems where back-coupling effects are significant, the emulator can still provide value. It allows researchers to conduct repeatable and directly comparable tests across various energy extraction circuits. These emulator-based results can then be complemented by additional evaluations using an actual PEH device to quantify the back-coupling effects of electrical loading. Analyzing the differences between the emulator-based results and the real PEH test results can offer deeper insights into the specific contributions of back-coupling effects. This is an experimental result that would be challenging to get without the emulator. This result could then be used to get more insight into whether the PEH is effectively converting its mechanical energy into electrical energy.

3.3. Proposed Conceptual Architecture

This section outlines the proposed architecture for the PEH emulator and describes the context in which it operates. Figure 3.1 illustrates the working principle of the emulator.

The PEH being emulated is excited by a vibration source, which influences the displacement of the PEH y. This displacement causes charge to build up in the piezoelectric element, represented by the piezoelectric current i_p, which results in a voltage potential v_p across the piezoelectric capacitance C_p. This voltage is measured under open-circuit conditions and the corresponding waveform is recorded.

The recorded voltage waveform is then replayed using an arbitrary waveform generator (AWG), which serves as the input to the PEH emulator. The emulator itself functions as a voltage-controlled voltage source (VCVS) with an output impedance matched to that of the actual piezo element. This source generates an output voltage equivalent to the measured v_p, assuming $\beta v_{in} = v_p$. Given the source impedance and voltages are the same as those in the piezoelectric patch, the output of the PEH emulator should replicate the behavior of the real PEH.

While the architecture in Figure 3.1 includes a dedicated VCVS within the emulator, it is natural to question whether this component is strictly necessary. One might consider omitting the VCVS and using the AWG directly to emulate the PEH, simply by driving a matched output impedance equivalent to the piezoelectric capacitance C_p. However, there are three primary reasons for introducing this intermediate stage.

Firstly, most commercially available AWGs are limited in their output voltage range. Typical maximum output amplitudes lie between $\pm 5\,\mathrm{V}$ and $\pm 12\,\mathrm{V}$, which is insufficient to meet the emulator's target specification of up to $\pm 25\,\mathrm{V}$. This is also why gain factor β for v_{in} is needed. Secondly, the current drive capabilities of standard AWGs are inadequate for the intended application. While high-end instruments may deliver output currents in the range hundreds of milliamperes, the PEH emulator is required to both source and sink currents up to $3\,\mathrm{A}$. Thus, relying solely on the AWG would not satisfy the voltage and current performance requirements.

Finally, although not a critical flaw, the use of an earth-referenced signal by most AWGs introduces a practical complication. Most AWGs produce an earth referenced output signal. Measurement equipment (such as most oscilloscopes) are also commonly earth-referenced. This means any attempt to perform measurements after a full-bridge rectifier could result in a direct short, as illustrated by the red path in Figure 3.2. This scenario would necessitate the use of differential measurement techniques for all analysis after the full bridge rectifier, including evaluations of potential wireless sensor node circuits connected to the emulator. Although differential measurements are feasible, avoiding the need for them would be preferable. Therefore, the choice was made to implement a floating output for the emulator.

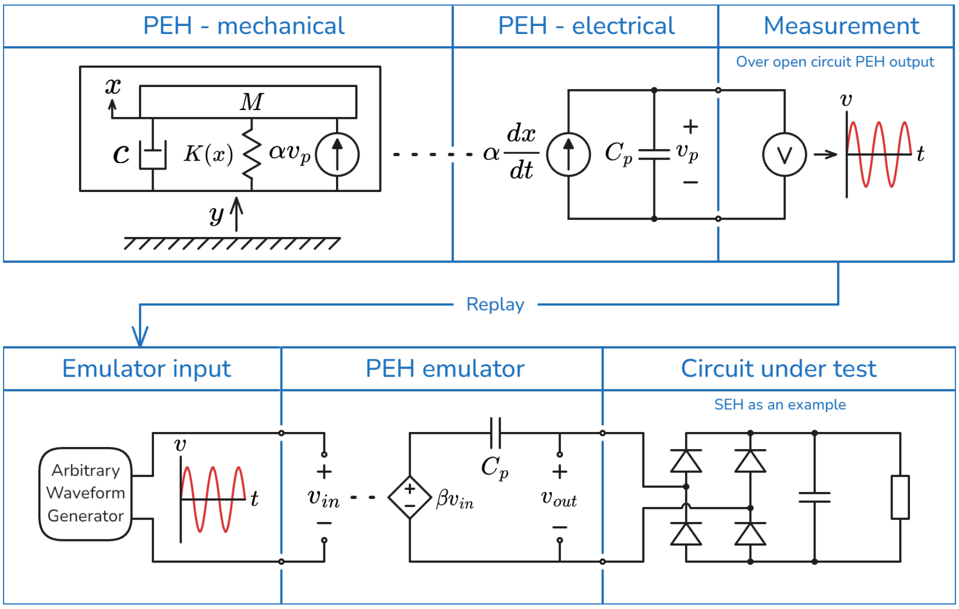

Figure 3.1: The general architecture of the PEH emulator placed in the context of the proposed lab setup.

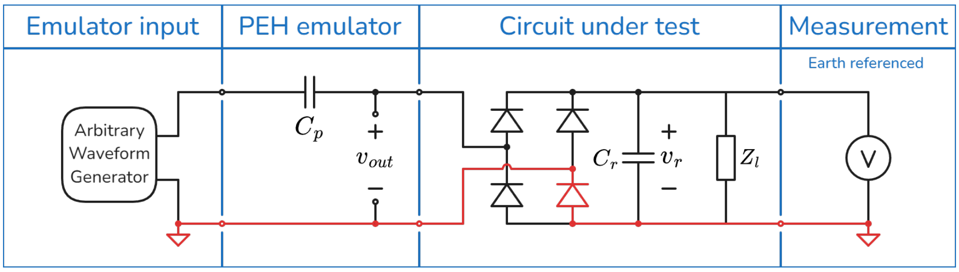

Figure 3.2: The potential issues of using an earth referenced AWG to directly while performing measurements with earth referenced measurement equipment. The red line indicates the path of the short circuit created.

3.4. Detailed System Design

This section describes the implementation of the system outlined in Section 3.3.

3.4.1. Digital or Analog Based Emulation

As illustrated in Figure 3.1, the PEH emulator must ultimately convert digital measurements of the output voltage into an analog signal that emulates the physical behavior of a real PEH system. An important design decision in this context is determining the domain in which to model the emulator's output impedance, denoted as C_p. The choice is between modeling in the analog or digital domain. Modeling in the analog domain refers to the use of discrete physical components, such as capacitors, to replicate C_p. Conversely, a digital approach involves algorithmically defining the behavior of C_p within the control loop and generating the corresponding analog output through digital-to-analog conversion.

Modeling the impedance digitally offers several advantages, primarily in terms of precision and flexibility. Digital control allows for exact specification of the effective capacitance C_p, including nonlinear characteristics such as DC-bias, wherein the capacitance value changes with the applied voltage. Replicating such voltage-dependent behavior using discrete analog components is challenging. These types of effects are explored in further detail in Section 4.3.

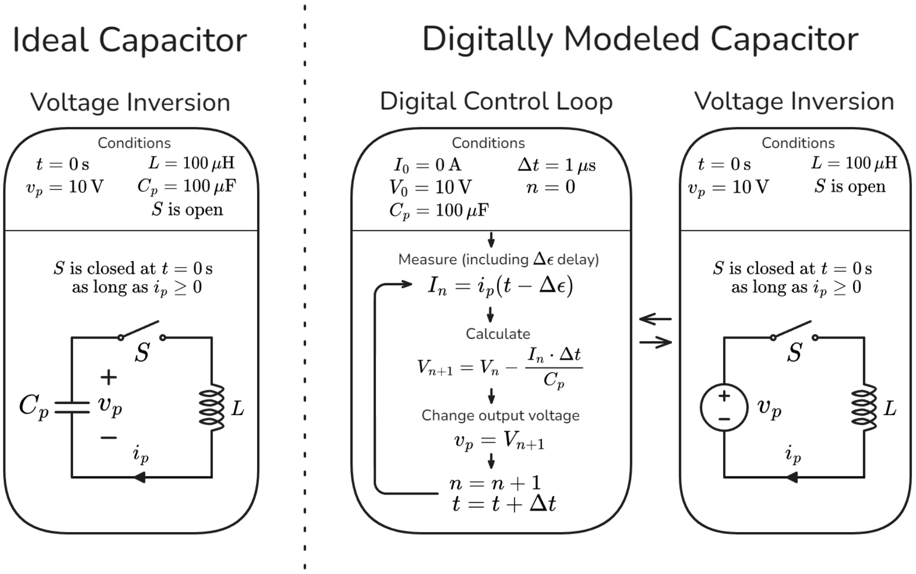

Figure 3.3: The comparison setup used between an ideal capacitor and a proposed digital model of a capacitor. The digital model controls v_p beased on the output current i_p measured with delay $\Delta\epsilon$.

However, the digital modeling approach also introduces notable drawbacks. To highlight these limitations, we first consider the idealized case in which the impedance is represented purely as a linear capacitor. A digitally emulated capacitor, in this context, measures the output current and updates its output voltage in accordance with the fundamental capacitor relationship. The challenge lies in the inherent latency of digital systems. Many energy extraction techniques, such as P-SSHI, involve rapid voltage transitions across the output impedance. The emulator must respond to these rapid changes with high precision in order to accurately emulate the PEH system.

Figure 3.3 illustrates the setup used to compare an ideal analog capacitor with its digitally modeled counterpart. Both configurations are subjected to the same conditions, with the key differences being the digital system's sampling interval Δt and its measurement delay $\Delta\epsilon$. As shown in Figure 3.4, even a small measurement delay $\Delta\epsilon$ results in a substantial overestimation of the flipped voltage magnitude v_p. To preserve accuracy in emulating the true capacitor behavior, it is essential that the total delay $\Delta\epsilon$

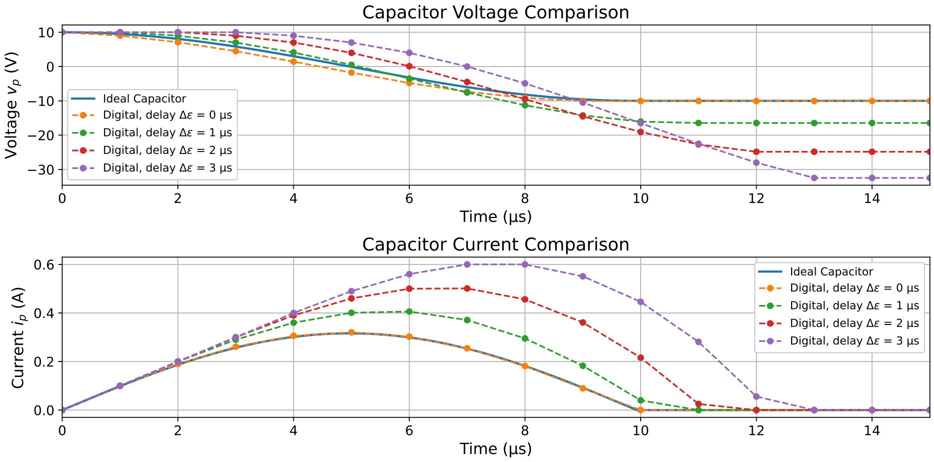

Figure 3.4: The voltage and current waveforms comparing the effects of a voltage inversion circuitry combined with digital modeling of the output impedance in the PEH emulator. Here the results show the effect of measurement delay on the accuracy of the voltage inversion process.

remains much smaller than the oscillation period of the LC circuit, given by $2\pi\sqrt{L \cdot C_p}$.

For example, a measurement delay of just 100 ns results in a deviation of approximately 0.545 V in the flipped voltage. This illustrates the significant impact that even minor delays can have. Consequently, designing a digital system to emulate capacitive impedance with sufficient accuracy presents a major challenge. Without extremely low-latency sensing and control, the emulator may introduce substantial inaccuracies, undermining its effectiveness in mimicking real PEH behavior. For this reason the choice was made to model the output impedance in the analog domain.

3.4.2. Circuit Implementation

This section elaborates on the practical realization of the conceptual PEH emulator architecture presented in Figure 3.1. The core of the circuit implementation is illustrated in Figure 3.5.

From the input side, resistors R_1 and R_2 are used to limit the build-up of excessive common-mode voltage relative to ground. Series resistors R_3 and R_4 act as current-limiting elements to safeguard under potential fault conditions and are part of the filter network. The input path includes switches S_1 and S_2, which allow for the selection between AC- and DC-coupling. When AC-coupling is selected, the signal path incorporates both low-pass and high-pass filters to suppress unnecessary noise.

The conditioned differential signal is subsequently processed by an instrumentation amplifier, U_1, which provides a gain referenced to ground. This stage ensures a high common-mode rejection ratio. The gain of this stage can be configured by selecting an appropriate resistor R_7.

The output of U_1 is then fed into an inverting power amplifier, U_2, which serves to deliver the required output voltage and current levels as dictated by the emulator's design specifications. This amplifier stage increases signal amplitude and acts as a voltage buffer with high output current drive capability. To ensure the stability of this buffer stage a compensation network comprising R_9 and C_6 is introduced. This network serves to improve the phase margin and suppress undesirable peaking or oscillatory behavior. This is explained further in Section 3.5.2. Additionally, R_{10} and C_7 define the frequency-dependent gain characteristics of the inverting amplifier through their inclusion in the feedback path. Protection diodes D_1 and D_2 are placed at the amplifier output to clamp the voltage swing within safe limits, thereby protecting output of the inverting amplifier.

The resulting output forms the effective VCVS output of the emulator. After this output impedance matching is still required to mimic PEH behavior. Impedance matching is achieved through the configurable elements C_p and R_p, which are mounted on sockets to allow easy replacement or tuning. This modular approach enables the emulator to accurately replicate a wide range of PEH characteristics by adapting its output impedance to that of the target piezoelectric element.

3.4.3. Component Selection

This section details the component values and their corresponding roles within the circuit implementation shown in Figure 3.5.

Coupling Selection and Filtering

The configuration of switches S_1 and S_2 determines whether the input path operates in AC- or DC-coupling mode, thereby activating different parts of the filter network.

When configured for AC-coupling, the components R_3, R_4, C_1, C_2, and C_3 collectively form a filter that simultaneously attenuates high-frequency content in both the differential and common-mode portions of the input signal. The low-pass cutoff frequency for differential-mode signals is defined as

$$f_{\text{LP DIFF}} = \frac{1}{2\pi R_3(2C_2 + C_1)}, \tag{3.1}$$

assuming symmetrical component values, specifically $C_1 = C_3$ and $R_3 = R_4$, to ensure balanced signal processing across both input lines. To minimize the degradation of the common-mode rejection ratio (CMRR) caused by mismatches in the filter network, it is advisable to select C_2 to be at least an order of magnitude greater than C_1 (i.e., $C_2 \geqslant 10C_1$), as recommended in [40]. The corresponding low-pass

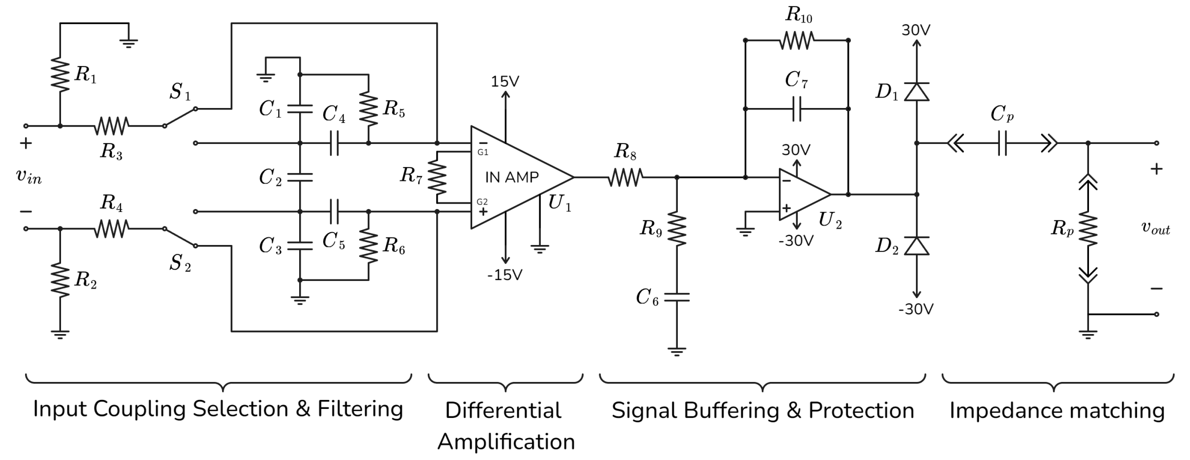

Figure 3.5: The core of the circuit implementation of PEH emulator.

cutoff frequency for common-mode signals is given by

$$f_{\text{LP CM}} = \frac{1}{2\pi R_3 C_1}, \tag{3.2}$$

again under the assumption that $C_1 = C_3$ and $R_3 = R_4$, ensuring that both legs of the differential signal experience identical common-mode attenuation. Following the low-pass filter stage, a high-pass filter may be formed using components R_5, R_6, C_4, and C_5. The cutoff frequency for the common-mode high-pass filter is defined as

$$f_{\text{HP CM}} = \frac{1}{2\pi R_5 C_4}. \tag{3.3}$$

Symmetry in this case is again essential, with $C_4 = C_5$ and $R_5 = R_6$, to ensure equivalent filtering across both differential inputs. This configuration helps suppress DC offset components that could affect amplifier performance.

When the emulator is operated in DC-coupling mode, resistors R_1 and R_2 become important. These high-value resistors are introduced to prevent the accumulation of excessive common-mode voltage with respect to the circuit ground. In cases where the input is left floating or unconnected, they define a default bias point near 0 V at the amplifier's input. Their high resistance is critical, as the input stage is likely earth-referenced while the output of the emulator must remain floating. By limiting the current path between earth-referenced and floating domains, these resistors mitigate the risk of affecting DUTs that are themselves referenced to earth, as illustrated in Figure 3.2.

Differential Amplification

Following the input filtering stage, the conditioned differential signal is amplified and referenced to ground using an instrumentation amplifier U_1. In this design, the AD8421 instrumentation amplifier is employed [40]. In general, instrumentation amplifiers have good CMRR, which allows it to effectively suppress common-mode noise and pass only the true differential component of the signal .

The gain of the instrumentation amplifier, denoted as G_{INA}, is set by an external gain resistor R_7. The relationship between the desired gain and the resistor value is given by

$$R_7 = \frac{9.9\ \text{k}\Omega}{G_{INA} - 1}. \tag{3.4}$$

As is typical for instrumentation amplifiers, the AD8421 operates within supply voltage limits that do not support input voltages exceeding ±18 V. To accommodate this constraint, a dedicated ±15 V supply rail was derived from the main ±30 V power input. This lower-voltage rail exclusively powers the instrumentation amplifier stage, while the higher ±30 V supply is reserved for the buffer amplifier stage that follows.

Signal Buffering and Protection

After the differential amplification stage, the signal is routed to an inverting buffer amplifier responsible for delivering the required voltage and current levels. This stage is implemented using the OPA544 [41], denoted U_2, and is configured for both signal amplification and output protection.

The core of this stage is a standard inverting amplifier topology, composed of input resistor R_8 and a feedback network consisting of resistor R_{10} and capacitor C_7. The voltage gain of this amplifier stage, G_{BUF}, is determined by the ratio of these two resistors and is given by

$$G_{BUF} = -\frac{R_{10}}{R_8}. \tag{3.5}$$

The negative sign indicates phase inversion, which is acceptable within the overall emulator chain given that the previous stage is implemented in such a way that it also inverts the signal.

To ensure stability across a wide range of load conditions, a compensation network comprising resistor R_9 and capacitor C_6 is included. This network forms a low-pass filter at the inverting input of the amplifier and serves to enhance phase margin, reduce bandwidth-induced gain peaking, and suppress high-frequency oscillations. The cutoff frequency of this compensation filter is defined by

$$f_{\text{COMP}} = \frac{1}{2\pi R_9 C_6}. \tag{3.6}$$

This compensation technique is particularly important given the potentially partially capacitive loads, such as long cabling, that the PEH emulator must be capable of driving. An example of the effect of the addition of these components can be seen in Section 3.5.2.

The amplifier U_2 is powered from ±30 V rails directly coming from external power supplies. This allows it to deliver output signals with amplitudes up to ±25 V, as required by the emulator's design specification. To protect the amplifier and connected circuitry against voltage excursions beyond its safe operating range, clamping diodes D_1 and D_2 are included at the output. These diodes conduct when the output exceeds 30 V in magnitude, thereby preventing damage to the amplifier.

Impedance Matching

Following the buffer amplifier stage, the emulator output requires impedance matching to accurately reflect the electrical characteristics of the PEH system being emulated. This is achieved by configuring both a series impedance C_p and a parallel impedance R_p, which together define the effective output impedance seen by the connected circuit.

To facilitate this, a quick-swap connector is employed at the emulator output. This allows for easy insertion and removal of through-hole components that represent the desired impedance values. The use of physical components enables straightforward adaptation to different PEH systems by selecting matching values for C_p and R_p, based on the specific characteristics of the device being emulated. Additionally, this modular setup provides flexibility to represent more complex impedance profiles when needed. For instance, multiple components can be combined to approximate frequency-dependent impedance behavior.

Component Values

Table 3.1 provides an overview of the component values and calculated parameters used in the core design of the PEH emulator. The table includes all passive and active elements involved in signal conditioning, amplification, as well as previously discussed performance metrics such as cutoff frequencies and gain settings.

Parameter	Value	Function / Description
C_1, C_3	1 μF	Common-mode low-pass filter capacitors to ground
C_2	10 μF	Differential-mode low-pass filter capacitor
C_4, C_5	10 μF	High-pass filter capacitors
C_6	470 pF	Compensation capacitor
C_7	82 pF	Feedback capacitor, affects high-frequency gain roll-off
C_p, R_p	Swappable	Output impedance matching components
D_1, D_2	SS56	Output clamping diodes
R_1, R_2	100 MΩ	Input referencing resistors
R_3, R_4	5 Ω	Series low-pass filter resistors
R_5, R_6	20 kΩ	High-pass filter resistors
R_7	10 kΩ or 5 kΩ	Gain setting resistor for U_1 (changeable via header)
R_8	5 kΩ	Input resistor for inverting buffer amplifier
R_9	1 kΩ	Compensation resistor
R_{10}	15 kΩ	Feedback resistor for buffer gain
U_1	AD8421ARZ	Instrumentation amplifier
U_2	OPA544FKTTT	High-current, high voltage buffer op-amp
f_{COMP}	339 kHz	Compensation network frequency
$f_{\text{HP CM}}$	0.796 Hz	Cutoff frequency for both common mode high-pass filters
$f_{\text{LP CM}}$	31.8 kHz	Cutoff frequency for both common mode low-pass filters
$f_{\text{LP DIFF}}$	1516 Hz	Cutoff frequency for the differential low-pass filter
G_{BUF}	-3	Inverting buffer gain
G_{INA}	-2 or -3	Instrumentation amplifier gain (changeable via header)
β	6 or 9	Full system gain ($G_{INA} \cdot G_{\text{BUF}}$)

Table 3.1: Component values and calculated parameters for PEH emulator.

3.4.4. Supporting Equipment

This section discusses supporting instrumentation that complements the operation of the PEH emulator, with particular emphasis on voltage and current measurement tools. Accurate electrical characterization of energy extraction circuits presents two primary challenges.

The first challenge involves current measurement, which must accommodate a wide dynamic range. Certain energy harvesting techniques, such as those employing voltage inversion, generate brief but significant current spikes during inversion events. These are followed by extended periods of minimal current draw. Capturing both transient high-current pulses and steady low-current consumption with sufficient resolution requires a measurement solution capable of rapid sampling and a great dynamic range.

The second challenge pertains to voltage measurement, particularly with respect to probe impedance. For example, the input impedance of conventional 10x oscilloscope probes is typically 10 MΩ, which may not be sufficiently high for low-power systems. At an output voltage of 25 V, such a probe would dissipate 62.5 μW. This load is non-negligible in the context of PEH systems, where total power levels can be comparably low. As a result, high-impedance measurement is essential to ensure minimal impact on the DUT measurements.

To address these challenges, the Joulescope JS220 precision energy analyzer was selected [42], which can be seen in Figure 3.6. The JS220 combines high-speed sampling with automatic dynamic current range switching, making it well-suited for measuring systems with rapidly fluctuating currents. It also features an high input impedance of approximately 1 GΩ, which significantly reduces measurement-induced loading on low-power circuits.

Figure 3.6: The Joulescope JS220: precision energy analyzer [42].

A key limitation of the JS220 is its absolute maximum input voltage rating of ±15 V. For scenarios requiring measurements above this limit, the PEH emulator includes an optional resistive voltage divider that attenuates the output voltage by a factor of three. This divider introduces an additional 30 $\mathrm{M}\Omega$ load across the output. While this feature enables safe operation within the JS220's input range, it is recommended to avoid its use unless absolutely necessary, as it introduces additional loading on the system and may affect measurement accuracy as previously discussed.

3.5. Simulations

To verify that the emulator meets its performance requirements, a series of simulations were conducted focusing on both frequency-domain and time-domain behavior. These simulations assess the stability and accuracy of the buffer stage under varying load conditions, as well as the emulator's ability to maintain voltage fidelity during transient events such as voltage inversion. The following sections detail the simulation setup, test configurations, and results.

3.5.1. Simulation Setup

All simulations were performed using LTspice 24.1.0. The OPA544 power amplifier was modeled using the official SPICE model provided by Texas Instruments. The transistors used in the electronic breaker circuit are the standard 2N3904 and 2N3906 bipolar junction transistors included with LTspice. Passive components such as resistors, capacitors, and inductors were taken from the LTspice default library.

3.5.2. Frequency Dependent Behavior

This section evaluates the emulator's stability and frequency response under varying capacitive and resistive load conditions, with a focus on the buffering stage as the critical component influencing system behavior.

Capacitive Loads

To assess the system's stability with different capacitive loads, a simulation was carried out. Since the buffering stage is the main factor influencing stability in this case, only this part of the circuit was included in the analysis. The buffer should be able to drive up to 1 nF of capacitive load without becoming unstable.

The Bode plots in Figure 3.7 show the frequency response of the buffer stage without a compensation network (i.e., with R_9 and C_6 omitted) for three capacitive loads: 100 pF, 500 pF, and 1000 pF. All cases show a phase shift near or beyond 180° at their respective resonant peaks. The 100 pF load reaches a peak gain of −6.0 dB, which is likely not enough to cause instability, though it may still lead to output ringing. In comparison, the 500 pF and 1000 pF loads result in peak gains of 5.4 dB and 21.8 dB, respectively. At these levels, combined with their phase behavior, instability becomes a clear issue if no compensation is used.

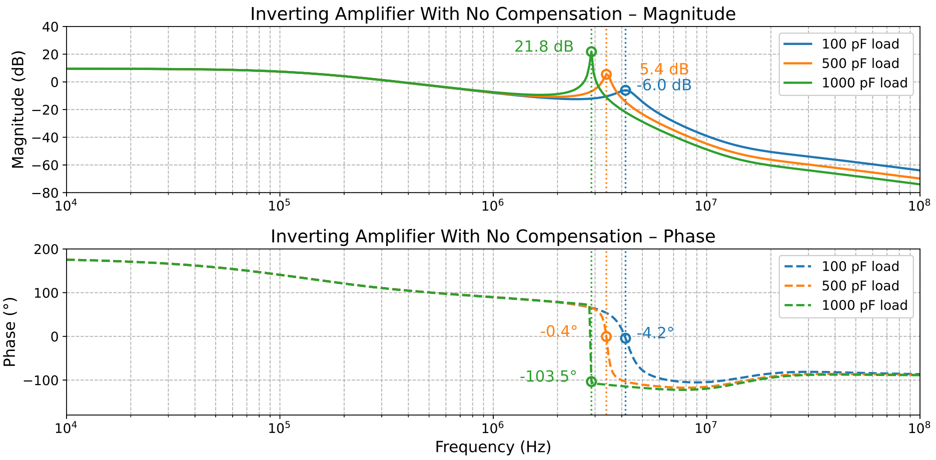

Figure 3.7: Bode magnitude and phase plots of the inverting amplifier's buffer stage under varying capacitive loads with no compensation network applied. Increased capacitive loading results in resonant peaks at frequencies with already significant phase lag, leading to instability beyond 100 pF.

Figure 3.8 shows the effect of adding the compensation network on the stability of the buffer stage. Compared to the uncompensated case, the resonant peaks in the magnitude response have been significantly reduced. The remaining peaks are low in gain and unlikely to introduce any instability. This indicates that the compensation network is effective in damping out resonance and maintaining stable operation across all tested capacitive loads.

Resistive Loads

To assess the system's stability under different resistive loads, a simulation was carried out. As with the capacitive load test, only the buffer stage was included in the analysis since it is the main factor that affects stability. Figure 3.9 shows the frequency response of the buffer stage for four resistive loads: 1 Ω, 10 Ω, 100 Ω, and 1000 Ω. The output voltage was chosen so that the 1 Ω load would draw peak currents of up to 3 A, which is the maximum current specified for the system.

The figure clearly shows that the phase and gain margins are high for all tested load values. This means the system is not at risk of becoming unstable, even under heavy loading conditions. The results confirm that changing the resistive load does not negatively affect the stability of the buffer stage.

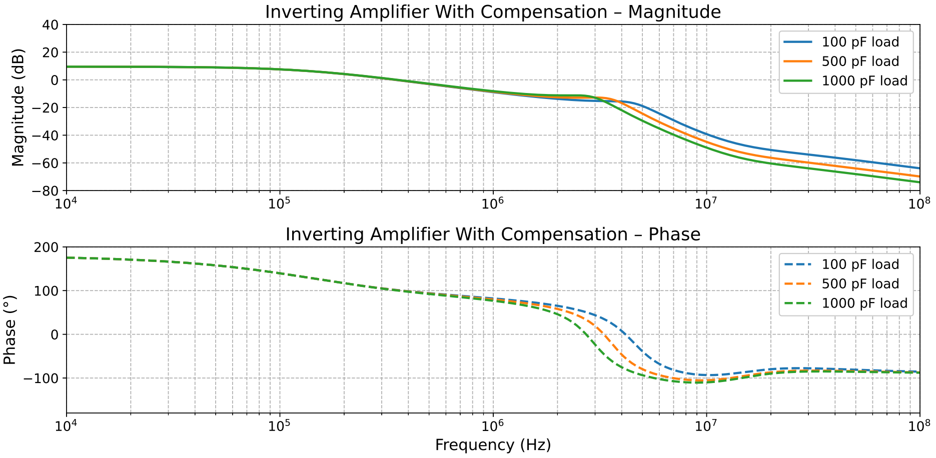

Figure 3.8: Bode magnitude and phase plots of the inverting amplifier's buffer stage with compensation network (R_9 and C_6) added. The resonant peaks seen in the uncompensated configuration are significantly suppressed, resulting in improved stability across all capacitive load conditions.

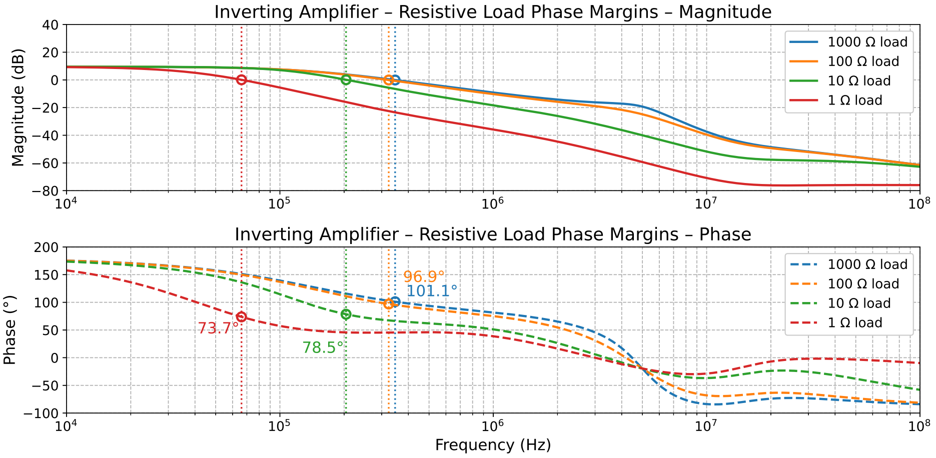

Figure 3.9: Bode magnitude and phase plots of the inverting amplifier's buffer stage under varying resistive load conditions. The system remains stable across all tested loads, including at maximum current draw.

Full System

The frequency-dependent gain of the VCVS, which includes the AC-coupled input, differential amplification stage, and signal buffering stage, is shown in Figure 3.10. The plot shows a gain of six in the 1 Hz to 1000 Hz range, with a maximum deviation of 1%. Beyond 1 kHz, the signal starts to attenuate. This is first due to the low-pass filter at the input, and then at higher frequencies it is additionally due to the limited bandwidth of the buffer stage.

3.5.3. Transient Behavior

While previous sections focused on frequency-dependent behavior, this section addresses the emulator's response to transient current spikes, particularly during voltage inversion events, which are common in energy extraction circuits.

Voltage inversion techniques cause brief but intense current demands from the emulator. It is critical that the signal buffering stage maintains voltage stability during these moments. If not, the operation of circuits such as the electronic breaker (see Section 2.3.2) may be compromised. Specifically, a voltage drop followed by a sudden rise can cause premature disconnection in the breaker circuit, preventing complete charge inversion and reducing efficiency.

To evaluate this behavior, a simulation was performed using the circuit shown in Figure 3.11. The setup includes an electronic breaker with a 100 µH inductor, which is a relatively low value for energy extraction circuits, leading to higher current peaks. A 10 Ω resistor is included to model energy extraction. Without this resistor, the voltage across the impedance matching capacitor C_p would rise to unrealistically high levels.

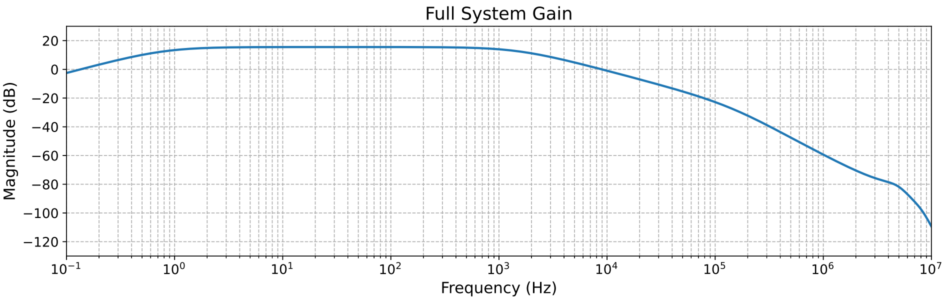

Figure 3.10: Frequency response of the full VCVS system including AC-coupling, amplification, and buffering stages.

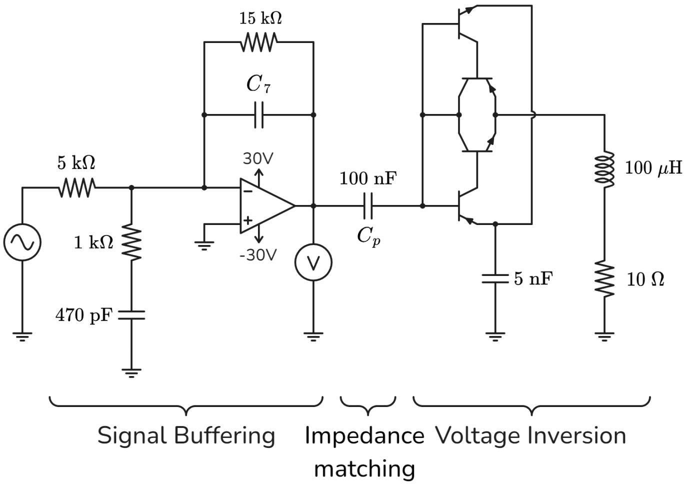

Figure 3.11: The voltage inversion circuit used to test transient behavior. The voltage probe corresponds to the traces shown in Figure 3.12.

Figure 3.12 presents the simulation results, configuring the input in such a way to cause a 10 V peak-to-peak, 50 Hz sine wave at the buffer output. The top plot shows the full waveform at the buffer output, with noticeable voltage disturbances at each inversion moment. The bottom plot provides a zoomed-in view of these transients, and highlights the effect of varying the feedback capacitor C_7, which determines the feedback cutoff frequency f_c of the inverting amplifier stage.

The results reveal an interesting takeaway. One might expect that a higher feedback cutoff frequency (lower C_7) would allow the amplifier to respond more quickly to sudden current spikes, resulting in less voltage drop. However, the opposite is observed. Lower values of C_7 lead to worse transient stability. This is because, aside from shaping the feedback response, C_7 also contributes directly to output voltage stability by adding capacitance between the output and virtual ground. In essence, C_7 helps smooth out the output voltage. Therefore, increasing C_7, and thus lowering the cutoff frequency, leads to better performance in handling fast transient conditions.

However, care must be taken not to increase C_7 to the point where it begins to attenuate or distort the desired output signal. The choice of C_7 must balance transient stability while providing the required bandwidth.

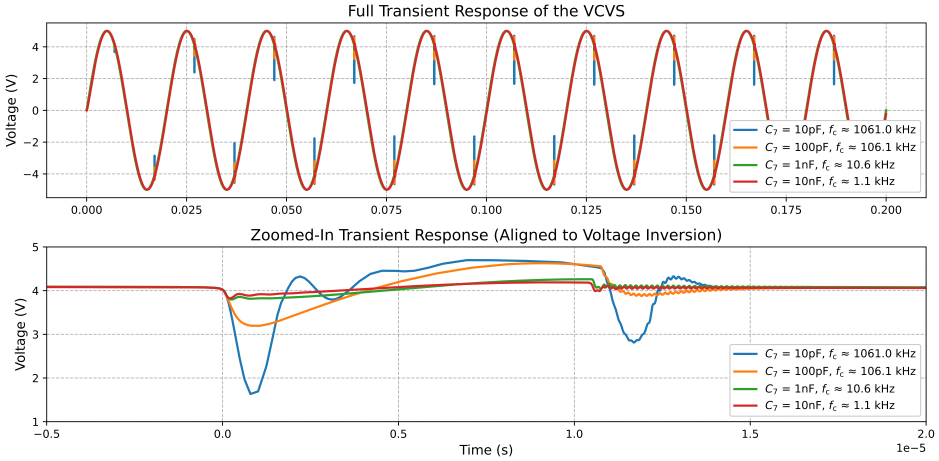

Figure 3.12: Transient response of the buffer stage under voltage inversion for various values of the feedback capacitor C_7. In the bottom plot, signals are synced at the time where the voltage inversion starts ($t = 0$). Higher C_7 (lower f_c) results in improved voltage stability.

3.5.4. Simulation Summary

The simulation results presented in the previous sections confirm that the emulator meets its performance requirements under a wide range of conditions. The frequency domain analysis shows that the system remains stable for both capacitive and resistive loads, provided the compensation network is present. Without compensation, capacitive loads above 100 pF introduce gain peaking and significant phase shifts, which could lead to instability. The addition of R_9 and C_6 effectively suppresses these effects and ensures stable operation up to the specified 1 nF load.

In the resistive load case, the system maintains a high phase margin even under heavy loading, including conditions that push the current draw to the 3 A design limit. This validates that the buffer stage is robust enough to handle demanding load scenarios without risk of oscillation or signal degradation.

The full system frequency response confirms that the emulator provides a gain of six in the 1 Hz to 1 kHz range with less than 1% deviation. This validates that the combined input, amplification, and buffer stages operate within the specified bandwidth and gain accuracy requirements.

The transient simulations demonstrate that the emulator can withstand rapid current spikes caused by voltage inversion events, provided that C_7 is selected appropriately. Interestingly, a higher feedback cutoff frequency (lower C_7) results in poorer transient stability, despite offering a faster theoretical response. This is due to the stabilizing role of C_7 as an effective output capacitance. Larger values of C_7 provide better voltage stability by suppressing transients, but care must be taken not to compromise the system bandwidth.

Taken together, the simulation results confirm that the emulator design is capable of delivering both stable and accurate performance under the electrical loading conditions typically seen in energy extraction circuit evaluations. The findings also highlight the importance of selecting component values, such as C_7, that strike a careful balance between stability and responsiveness.

3.6. Prototype Realization

The prototype of the PEH emulator was developed using a custom-designed printed circuit board (PCB). The layout and routing of the board are shown in Figure 3.13. The design is intended to fit within an extruded aluminum enclosure, with separate PCBs serving as the front and rear interface plates. A 3D rendering of the complete design, including enclosure integration, is provided in Figure 3.14.

The design was subsequently fabricated, and the following figures present the final physical assembly. Figure 3.15 depicts the front view of the assembled emulator. It includes two quick-swap connectors used to configure the series and parallel impedance, as well as BNC outputs for monitoring current, voltage, and the emulator output signal. The rear side of the device is shown in Figure 3.16, where a BNC connector facilitates input from an AWG. Additionally, banana plug terminals are provided for connecting to positive and negative supply rails, along with an earth terminal which earth references the chassis.

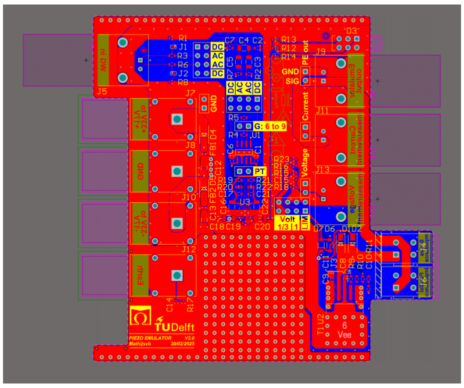

Figure 3.13: Layout and routing of the PEH emulator PCB.

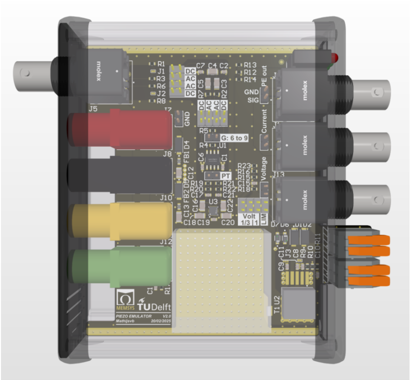

Figure 3.14: 3D render of the PEH emulator with enclosure.

Figure 3.15: Front panel of the PEH emulator.

Figure 3.16: Rear panel of the PEH emulator

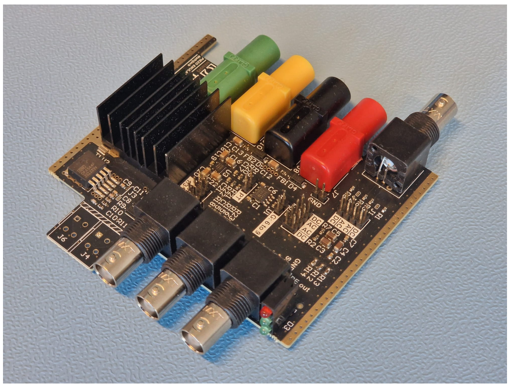

Figure 3.17: Custom PCB without enclosure components.

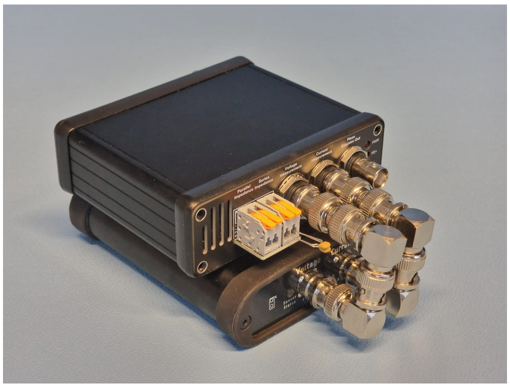

Figure 3.18: PEH emulator connected to Joulescope for power measurement.

For further detail, Figure 3.17 displays the custom PCB in isolation, without the enclosure or front/back interface plates. Finally, Figure 3.18 illustrates the PEH emulator connected to a Joulescope, enabling direct measurement of output power. The full system schematic can be seen in Appendix B. A detailed description of how to correctly set up and operate the emulator in a laboratory environment, including signal and power connections, can be found in Appendix C.

3.7. Summary

This chapter detailed the complete design process of the PEH emulator, starting from the identification of key functional and technical requirements. The emulator was required to emulate the electrical behavior of both linear and nonlinear PEH with sufficient current handling and voltage handling capability. Additional constraints included compatibility with standard lab equipment.

To meet these requirements, the design was based on a VCVS architecture with analog impedance modeling. This choice avoids the latency and complexity associated with digital impedance emulation, particularly under fast transients such as those introduced by voltage inversion in energy extraction circuits.

The analog domain output impedance matching was implemented by allowing for configurable discrete components, enabling flexibility across different PEH configurations. A custom buffer stage based on the OPA544 was designed to meet the current and voltage output specifications, with added compensation to ensure stability under both capacitive and resistive loading. Supporting circuitry, including filtering, protection, and circuitry allowing for measurements, was added to the design. Measurement considerations were addressed through integration with high-impedance, high-resolution tools like the Joulescope JS220.

Simulation results demonstrated that the emulator operates stably across the intended bandwidth. It also shows stability under varying loads, including voltage inversion circuits. Based on the design, a physical prototype was developed and assembled.

Together, the design, simulation, and prototype realization provide the foundation for validating the emulator's performance through experimental testing. The next chapter presents these experimental results and assesses the emulator's ability to accurately replicate real PEH behavior under practical circuit evaluation conditions.

4

Experiments

This chapter presents the experimental validation of the emulator developed in this work. The experiments are designed to address the performance, accuracy, and utility of the emulator in replicating piezoelectric energy harvester (PEH) behavior under realistic conditions.

The first part of this chapter focuses on validating the central motivation for the emulator, namely the difficulty of achieving repeatable circuit evaluations using real nonlinear PEH systems. This is demonstrated through long-duration measurements that show variability in electrical output even under constant excitation. These findings confirm the limitations of experimental evaluation using nonlinear harvesters and reinforce the value of an emulation-based approach.

The remainder of the chapter is dedicated to validating the performance of the emulator itself. The experiments are structured to evaluate its core functionalities, gain behavior, output noise characteristics, and impedance accuracy. Particular emphasis is placed on comparing the emulator's output against that of a real PEH device under varying excitation and electrical loads. This comparison provides insight into the emulator's accuracy and areas for potential refinement in future designs.

Collectively, the results presented in this chapter demonstrate that the emulator is capable of producing realistic PEH output behavior in a controlled manner. This establishes the emulator as a practical tool for energy extraction circuit evaluation, addressing the limitations identified in earlier chapters.

4.1. Validating the Chaotic Behavior in a Nonlinear PEH

The aim of this experiment is to validate the claim made in Section 2.5, namely that nonlinear harvesters can exhibit varying electrical output despite constant mechanical excitation. This phenomenon directly motivates the development of the PEH emulator, as it highlights the challenges in achieving repeatable circuit evaluations using real nonlinear PEH devices.

Experimental Setup

A custom bistable piezoelectric harvester was used for this experiment. The design of the bistable harvester was based on the buckled beam architecture combined with a PZT-5H piezoelectric patch. This PEH was excited using a shaker system replaying an 8-second vibration profile recorded from a 50 kW industrial electric motor. The harvester was connected to a P-SSHI extraction circuit, identical to the one shown in Figure 2.5, and was loaded with 3.3 V at the output. Output power was measured at the load over a one-hour period, representing a realistic longer-term energy harvesting scenario.

Results

Figure 4.1 shows the measured output power over the one-hour duration. Despite the excitation waveform remaining constant, the power output varies substantially over time. The signal exhibits both steady and irregular phases, with significant fluctuation in power levels even though input excitation signal remains identical.

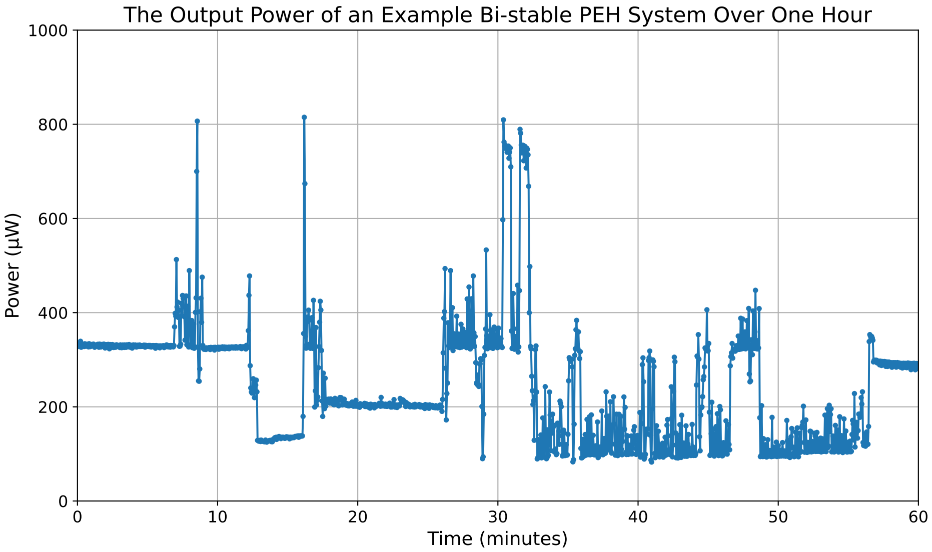

Figure 4.1: The variation in output power of an example nonlinear PEH under constant excitation conditions.

Discussion

The observed behavior confirms that nonlinear PEH systems can produce inconsistent output power even under constant excitation. This variation arises from internal chaotic effects caused by the dynamics introduced via bistability. As a result, using real nonlinear harvesters for evaluating extraction circuits can lead to results that are difficult to reproduce, even when the same PEH system is used. These findings support the need for an emulator that provides a stable, repeatable representation of PEH behavior for extraction circuit evaluation.

4.2. Validating Functioning of the PEH Emulator

This section evaluates the electrical behavior of the emulator in practice. Specifically, it verifies whether the frequency-dependent gain aligns with simulation results, and examines the emulator's inherent output noise characteristics under both AC- and DC-coupling configurations.

Experimental Setup

To measure the output noise spectrum, the emulator was connected to an AWG configured to output a constant zero-Volt signal. The emulator output was then measured using an oscilloscope, while a second oscilloscope channel was connected to an identical cable left unconnected to serve as the baseline. A total of 10,000 recordings, each consisting of 8192 samples, were captured and averaged in the frequency domain to obtain the noise spectrum.

Results

Figure 4.2 shows the RMS voltage noise spectrum of the emulator in both AC- and DC-coupling modes. Across most of the frequency range, the emulator introduces no more than 15.6 dB of additional noise above the baseline which exactly corresponds with a gain of 6. Some minor oscillatory behavior is observed around 165 kHz in the DC-coupled configuration, peaking at approximately –81 dBV.

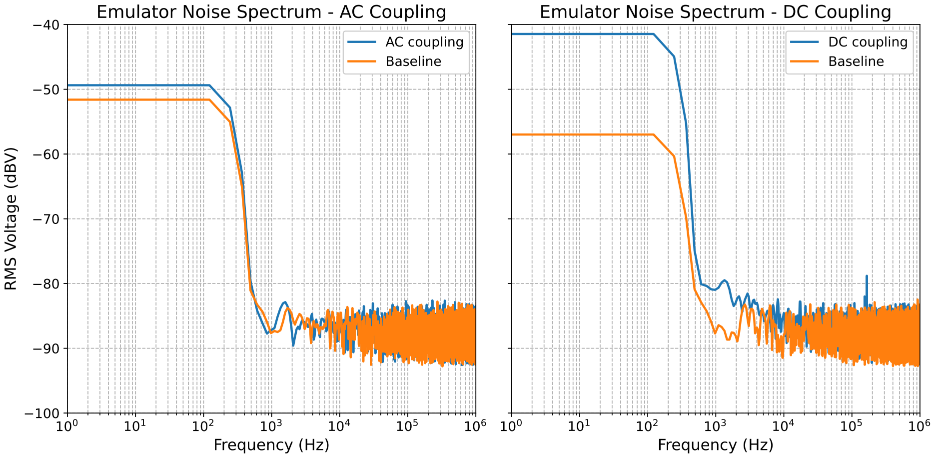

Figure 4.2: The noise spectra over frequency in terms of RMS voltage for both AC-coupled and DC-coupled emulator configurations based on an average of 10,000 recordings of 8192 samples.

Figure 4.3 shows the gain response of the emulator for both coupling configurations. The DC-coupled gain remains within the range of 5.931 to 5.939 between 1 Hz and 1000 Hz, closely matching the intended system gain of 6. The AC-coupled configuration displays a lower than expected high-frequency cutoff. The cutoff frequency is approximately one decade lower than simulations predicted.

Discussion

The results confirm that the emulator behaves in accordance with expectations. It is important to note, however, that the noise measurements were performed with a zero-volt input from the AWG, meaning the emulator output was idle throughout the acquisition. As such, the results might not reflect noise performance during active operation. Nevertheless, the low noise levels observed across the spectrum suggest that the emulator accuracy is unlikely to be influenced by noise under typical use conditions.

In terms of gain, DC-coupling meets the bandwidth and accuracy targets defined in Section 3.1.2 with only a slight deviation from the nominal gain, which can be corrected through adjusting AWG output voltages. The observed low-pass cutoff frequency in the AC-coupled configuration was approximately one order of magnitude lower than expected based on simulation. This discrepancy can be attributed to the 50 Ω output impedance of the AWG, which was not accounted for in the simulation model. This resistance adds to the resistance of the RC low-pass filter, thereby reducing the overall cutoff frequency of the system.

Overall, the results provide an initial characterization of the emulator's behavior under controlled conditions which is aligned with expectations.

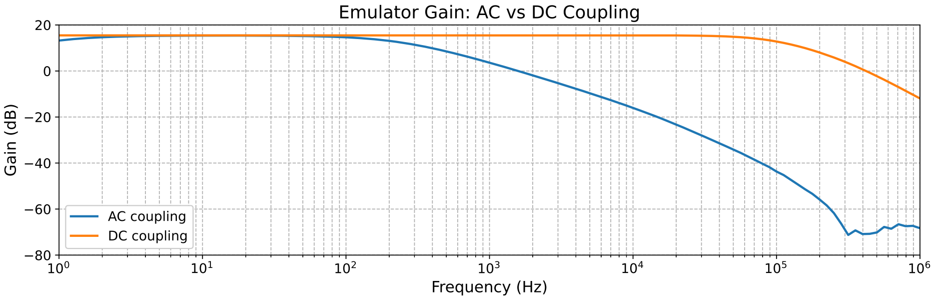

Figure 4.3: The gain over frequency characteristics of the emulator both in AC- and DC-coupled configuration.

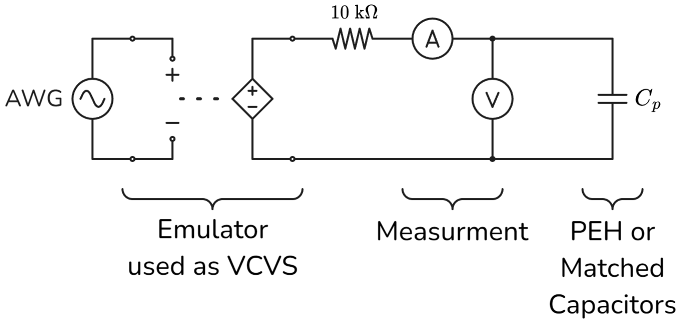

Figure 4.4: Experimental setup for impedance comparison between a PEH system and a ceramic capacitor array.

4.3. Impedance Matching a PEH

To evaluate how accurately the emulator can replicate the behavior of a real PEH system, it is essential to first match the emulator's output impedance to that of an actual PEH. This experiment focuses on performing that impedance matching using a discrete capacitor array and assesses how well this approximation captures the capacitive characteristics of a real PEH. Additionally, it provides insight into the limitations of modeling PEH impedance using discrete components, particularly under varying voltage conditions.

Experimental Setup

To evaluate how closely a matched ceramic capacitor array can replicate the impedance behavior of a real PEH system, this experiment focuses on a simplified impedance model. Specifically, the goal is to compare only the capacitive component of the impedance, as this is the most dominant and commonly modeled characteristic in literature.

The test configuration, shown in Figure 4.4, consists of the emulator acting as a voltage source driving an RC series circuit. The resistor value was 10 kΩ, and the capacitor under test was either a PEH or an array of ceramic capacitors. A triangle waveform was applied as the voltage source. This waveform was chosen to generate a square-wave current profile through the capacitor, simplifying current measurements by minimizing time spent in zero-crossing regions, where current noise dominates.

The resistor value was selected to be high enough to reduce current noise and low enough to preserve the linear slope of the applied voltage. During the test, voltage was limited to ±15 V to stay within the safe operating range of the measurement equipment.

For the ceramic capacitor array, multiple capacitors with X7R dielectric and 50 V voltage ratings were connected in parallel to approximate the PEH's nominal capacitance. The PEH device used was a simple cantilever beam with a PZT-5H piezoelectric patch. During testing, the cantilever was rigidly clamped to prevent mechanical deformation from influencing the electrical measurements.

Results

Figure 4.5 shows the voltage and current waveforms of both the PEH system and the matched ceramic capacitor under triangle wave excitation. Both systems exhibit current responses that resemble square waves, though with a sloped profile. The slope increases during higher-voltage portions of the charging and discharging phases, indicating that more current is required to sustain the same voltage change rate as voltage magnitude increases.

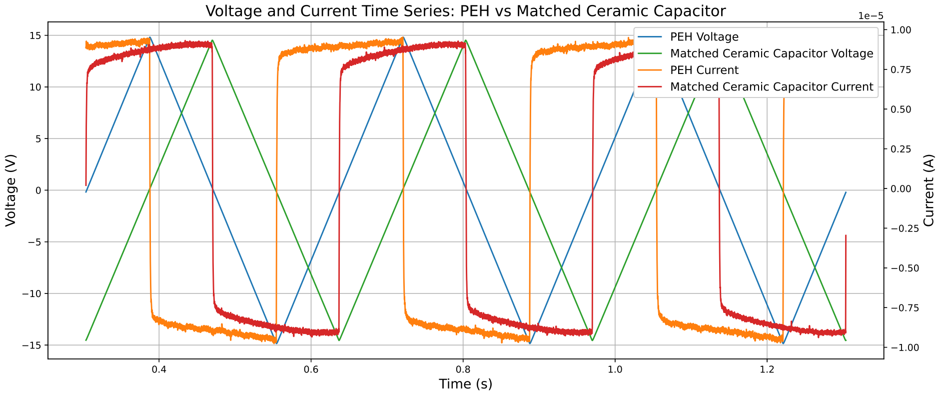

Figure 4.5: Voltage and current waveforms for a PEH system and matched ceramic capacitor under triangle wave excitation. The phase offset is manually added to make the waveforms more visible.

To better characterize the capacitive behavior over voltage, instantaneous capacitance was computed using a forward difference method as

$$C(V[n]) = \frac{i[n] \cdot \Delta t[n]}{V[n+1] - V[n]}, \tag{4.1}$$

where $i[n]$ is the current at sample n, $\Delta t[n] = t[n+1] - t[n]$, and $V[n]$ is the voltage at which the capacitance is evaluated. This method produces voltage–capacitance pairs for both the PEH impedance and the matched capacitor array. Figure 4.6 shows the resulting capacitance data as a scatter plot (left) and a binned mean curve (right), with bins of 0.1 V. An ideal capacitor would yield a flat, voltage-independent line in both plots. However, both the PEH and the ceramic array exhibit voltage-dependent behavior, deviating from the ideal case.

Discussion

The results show that both the PEH system and the matched ceramic capacitor array deviate from ideal capacitive behavior, exhibiting voltage dependency in a manner that suggests an impedance that is not purely capacitive. This non-ideal behavior is likely to introduce some inaccuracy in the emulator when using ceramic capacitors to mimic PEH output impedance.

In this experiment, the match targeted the zero-Volt region. However, the ceramic array shows a larger capacitance drop-off at higher voltages than the PEH. Because the emulator's output power scales

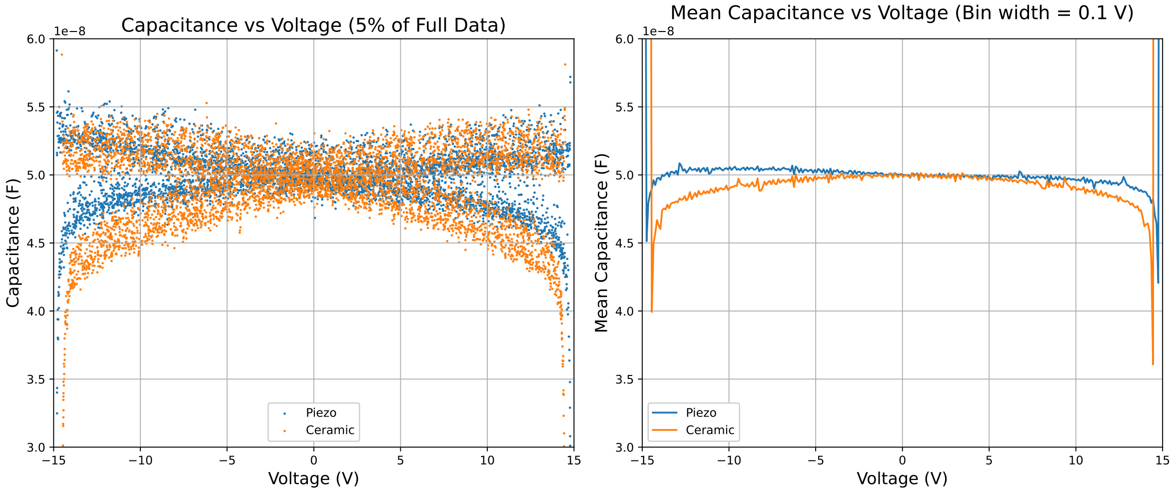

Figure 4.6: Voltage-dependent capacitance behavior of the PEH system and matched ceramic capacitor. Left: 5% of the raw sampled data; Right: binned mean values.

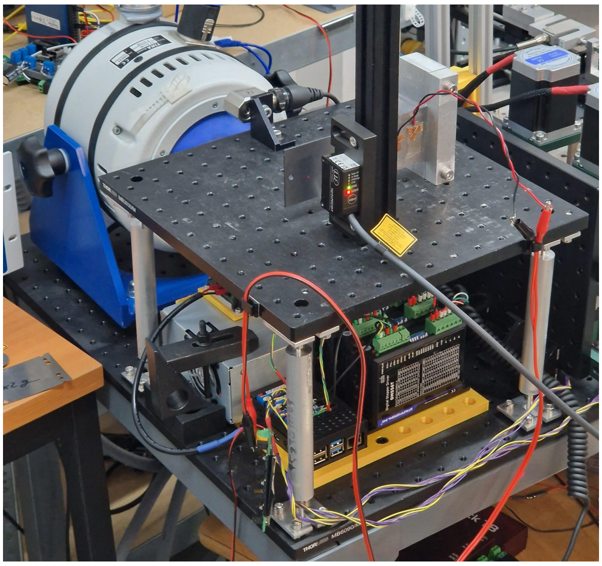

Figure 4.7: Experimental setup used to evaluate the electrical and mechanical behavior of the real PEH system. The PEH is mounted on a shaker platform, and tip displacement is measured using a laser displacement sensor.

with capacitance, this mismatch suggests that power delivery may be slightly underestimated. Importantly, the ceramic capacitance remains lower or equal to that of the PEH across the full voltage range, indicating that any power errors will likely result in underestimation rather than overestimation.

These findings suggest that while the initial impedance match is sufficient for testing, further refinements may be necessary if more accurate emulation is required, particularly under higher voltage conditions. A more detailed analysis of potential improvements is provided in Section 5.3.1. The next section will continue using this naive method of impedance matching to analyze its accuracy.

4.4. Validating the Accuracy of the PEH Emulator

This experiment aims to evaluate how accurately the emulator can reproduce the electrical output characteristics of a real PEH system under dynamic mechanical excitation. The comparison focuses on output voltage behavior across a range of resistive loads and excitation amplitudes.

Experimental Setup

The electrical characteristics of the PEH were measured using a custom-built vibration platform that provided horizontal displacement under sinusoidal acceleration as excitation. This excitation was generated using a TV 51140 shaker controlled via a Keysight EDU33212A signal generator going into an BAA 1000 shaker amplifier. The excitation frequency was chosen to be a few hertz below the system's mechanical resonance in order to minimize the influence of electrical loading on mechanical behavior. This choice helps mitigate back-coupling effects, which become more pronounced near resonance due to higher mechanical sensitivity to electrical loading conditions. A photograph of the experimental test setup used to evaluate the real PEH system is shown in Figure 4.7.

To characterize the PEH's output, a range of resistive loads from hundreds of ohms up to the megaohm range were applied. The resulting voltage across each load was measured using a resistor divider going into a Labjack T8 DAQ system, which added an additional 2.2 MΩ load to the system. This loading effect was accounted for in the calculation of total resistance. This meant the 2.2 MΩ value was the maximum measurable resistance in this setup.

During the experiment the mechanical displacement of the cantilever tip was monitored using a laser displacement sensor. This measurement served to validate the assumption of minimal electrical-to-mechanical back-coupling. A constant displacement profile across load conditions would support the assumption that changes in electrical load have negligible impact on mechanical behavior.

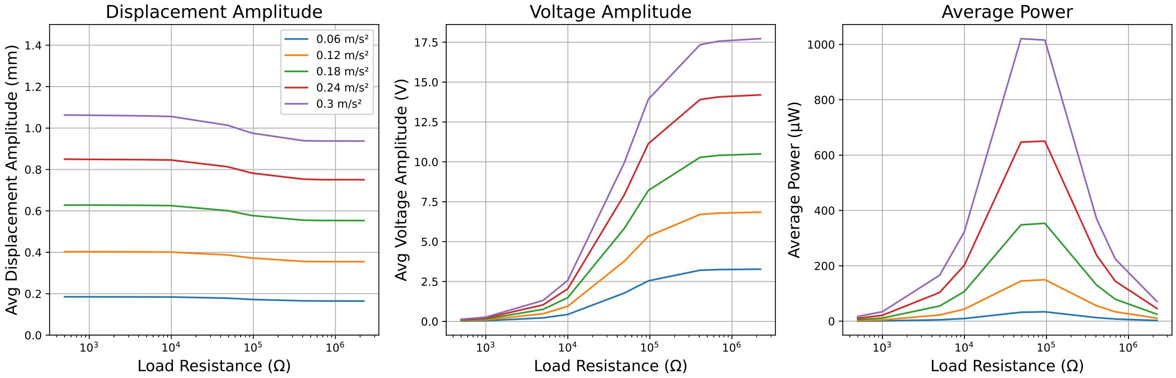

Figure 4.8: Measured displacement amplitudes (left), voltage amplitudes (center), and average output power (right) of the PEH system under different resistive loads and acceleration amplitudes.

For emulator validation, the matched capacitor array described in Section 4.3 was used to approximate the PEH output impedance. The open-circuit voltage of the PEH, defined as the voltage measured across the 2.2 MΩ load, was replayed by the emulator to simulate different acceleration levels. The rest of the emulator setup was the same as the one outlined in Appendix C with the only difference being the load not being an extraction circuit but a simple variable resistor.

Results showed that the assumption of negligible back-coupling did not hold. This meant a correction factor was required to adjust the emulator's output voltage to better align with the real PEH response. The derivation and application of this correction are detailed in the following section.

Results

Figure 4.8 shows the measured behavior of the real PEH system across a range of resistive loads and excitation amplitudes. The left plot shows average tip displacement amplitudes as measured by the laser sensor. The center and right plots show the resulting average voltage amplitudes and output power, respectively.

Across all excitation levels, output voltage increases with both load resistance and acceleration amplitude. Peak power output occurs between 50 kΩ and 100 kΩ, which is consistent with the expected behavior of a source with dominant capacitive impedance of around 50 nF excited at a frequency of 38 Hz.

The leftmost plot reveals a dependency of displacement amplitude on load resistance. At higher resistances, the PEH exhibits slightly greater mechanical displacement. This indicates that the electrical loading conditions influence the mechanical response which shows that back-coupling effects are present. As a result, the assumption that back-coupling effects do not influence the mechanical dynamics does not hold under these conditions.

Since this back-coupling violates the assumptions used in the emulator, the open-circuit voltage of the PEH cannot be directly used as an for emulator testing. Instead, a compensation method is applied to estimate the open-circuit voltage that would have occurred under equivalent mechanical excitation for each resistive load. This correction is based on the proportional relationship between open-circuit voltage and displacement amplitude, as derived in Equation A.3 and is given by the following formula:

$$v_{\text{OC comp}}(R) = v_{\text{OC}} \cdot \frac{X(R)}{X_{\text{OC}}} \tag{4.2}$$

Here, $X(R)$ is the measured displacement amplitude at load resistance R, X_{OC} is the displacement amplitude at open-circuit, and v_{OC} is the measured open-circuit voltage. The corrected open-circuit voltage, $v_{\text{OC comp}}(R)$, represents the voltage that would have been generated if the mechanical excitation under load matched that of the open-circuit condition. This corrected voltage is used in emulator

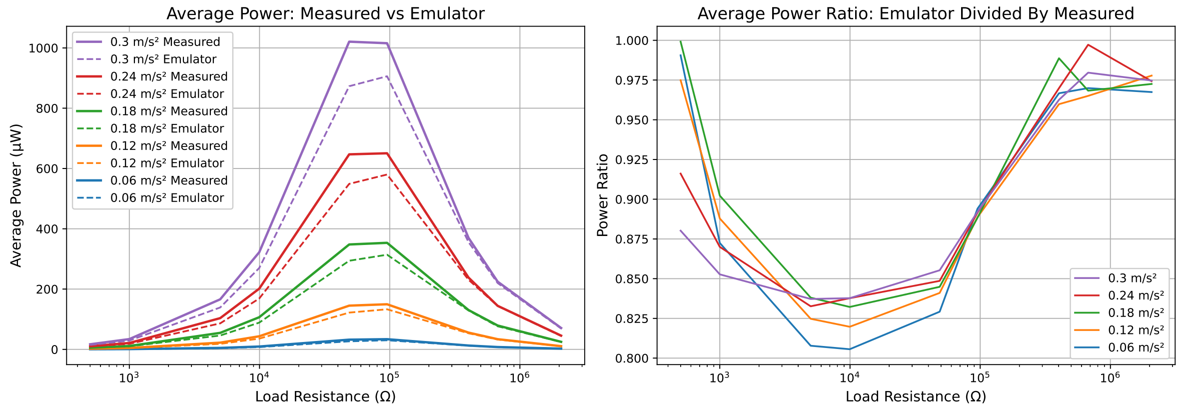

Figure 4.9: Left: Average power output of the real PEH and emulator across varying resistive loads. Right: Power ratio between emulator and PEH outputs. Corrected open-circuit voltage was used as emulator input.

validation to ensure a fair comparison between the emulator and real PEH behavior under matched mechanical input.

Figure 4.9 presents the comparison between the real PEH system and the emulator, using the corrected open-circuit voltage derived in the previous section. The left plot shows the average output power for both systems across a range of load resistances and excitation amplitudes. The emulator output tracks the measured power well across part of the range. The right plot shows the power ratio, defined as the emulator output power divided by the corresponding PEH output power. Across all acceleration levels, the power ratio remains between 0.80 and 1.00. The emulator shows the highest accuracy at the lower and upper ends of the load resistance range, while a dip in accuracy is observed in the mid-range (approximately 1 $k\Omega$ to 100 $k\Omega$), where underestimation of output power becomes more pronounced.

Discussion

The results of the output power comparison align with expectations discussed in Section 4.3. Specifically, the emulator is expected to slightly underestimate power output due to the conservative nature of the impedance match. The matched ceramic capacitor array has a lower equivalent capacitance at increasing voltage levels compared to the real PEH system. Since the applied voltage waveform is fixed, a lower capacitance results in reduced charge transfer per voltage cycle, and therefore lower electrical power output. This supports the hypothesis that the current impedance match does not lead to overestimation of performance, but instead introduces a systematic underestimation. Improving emulator accuracy may therefore require a more sophisticated impedance matching approach that more closely replicates the voltage-dependent characteristics of the real PEH system.

Another potential source of inaccuracy lies in the correction applied to the emulator's input voltage. This correction was based on a proportional relationship between mechanical displacement and open-circuit voltage. However, this method assumes a linear and voltage-independent capacitance, which may not be accurate enough of a simplification. Nonlinearities in the force-voltage conversion factor or piezoelectric capacitance could lead to deviations between the actual and assumed behavior, contributing to output power mismatch. That said, there is currently no direct evidence that such nonlinearities are the dominant cause of the observed error. Given the known limitations of the impedance approximation, improving the impedance match remains the most plausible and straightforward next step toward enhancing emulator accuracy. Potential methods of doing this will be discussed in Section 5.3.1.

4.5. Outcome and Experimental Limitations

The experiments presented in this chapter successfully validated the key design objectives of the emulator. As shown in Section 4.1, the chaotic nature of nonlinear PEH systems under constant excitation was confirmed, highlighting the need for a controllable and repeatable alternative. The emulator addressed this need effectively, as demonstrated in Section 4.2 - 4.4, by replicating realistic PEH output characteristics with a high degree of accuracy under linear resistive loads.

Quantitatively, the emulator exhibited low noise levels, predictable gain behavior, and realistic power delivery across a range of excitation levels and load conditions. Even when using a relatively simple impedance approximation, power output accuracy remained between 80% and 100%, as seen in Figure 4.9. These results support the conclusion that the emulator functions as a robust and accurate platform for evaluating energy harvesting circuits in repeatable test conditions.

However, one important aspect of the validation effort could not be completed. During the final phase of testing, the emulator experienced a hardware failure caused by power sequencing issues with the TPS7A3901 voltage regulator (see Section 5.2.1). This fault rendered the system inoperable before formal testing of nonlinear energy extraction circuits, such as P-SSHI, S-SSHI, and SECE, could be conducted.

Although no structured measurements could be recorded, it is worth emphasizing that these nonlinear circuits were actively explored during the development phase. The emulator was repeatedly used in informal tests involving nonlinear loading conditions, and no unexpected behavior or instability was observed. These observations strongly suggest that the emulator is capable of supporting such circuit types. Nevertheless, without formal datasets, it was not possible to include verified performance results for nonlinear circuits in this thesis.

This limitation does not affect the primary conclusion of the work, namely that the emulator meets its core objectives and can serve as a reliable tool for evaluating PEH extraction circuits. However, it highlights the importance of completing structured nonlinear circuit validation in future work to formally confirm the emulator’s performance under broader circuit topologies and operating conditions.

5

Discussion

This chapter reflects on the development, performance, and broader implications of the PEH emulator introduced in this thesis. The work combined theoretical modeling, circuit design, simulation, and experimental validation to create a hardware platform capable of replicating the electrical behavior of piezoelectric energy harvesters in a controlled and repeatable manner. The motivation for this work stemmed from the challenges associated with evaluating energy extraction circuits using real PEH devices, whose nonlinear and sometimes chaotic dynamics complicate consistent circuit benchmarking.

The chapter begins with a general discussion of the emulator's relevance, limitations, and potential role in broader research and development contexts. Design trade-offs, such as the exclusion of back-coupling to improve repeatability, are examined. The discussion also outlines several open research questions, including how estimating emulator accuracy might be extended to more complex excitation signals and circuit topologies. In addition, it explores the potential for standardization of emulator platforms, impedance models, and test procedures, drawing parallels with established practices in other energy harvesting domains.

Following this high-level reflection, the chapter shifts focus to practical design limitations uncovered during prototyping and testing. These include issues related to power supply configuration and the input voltage range of the differential amplifier in DC-coupling mode. Alternative hardware strategies are proposed to fundamentally improve the ability to accurately match the impedance of real PEH devices. This could be done via the architectural shift from a voltage-controlled voltage source to a current-source-based design.

Together, these discussions offer a comprehensive view of the emulator's current capabilities, the constraints encountered during development, and concrete next steps for advancing the design and its applications in both academic and commercial settings.

5.1. General Discussion

The following sections reflect on the broader significance of the emulator developed in this work, its current limitations, and opportunities for further research and standardization. While the primary focus of the thesis was technical implementation and validation, this discussion situates the emulator within the wider context of energy harvesting research and outlines key questions that remain for future development.

5.1.1. Broader Relevance and Applicability

The PEH emulator developed in this work addresses a fundamental challenge in the field of piezoelectric energy harvesting: the lack of a standardized and repeatable method for evaluating energy extraction circuitry. Unlike photovoltaics or thermoelectric systems, where emulator-based testing has become common practice, experimental evaluation of PEH circuits remains heavily reliant on real harvester devices. These devices often exhibit complex, nonlinear, and sometimes chaotic behavior, particularly in bistable configurations, making it difficult to reproduce results or conduct fair comparisons across different circuit designs.

By providing a hardware platform that replicates the electrical output of a real PEH system in a controllable and repeatable manner, the emulator introduced in this thesis fills this gap. Its compatibility with standard laboratory equipment and modular impedance configuration makes it a practical tool for both academic research and commercial development. In particular, it can significantly accelerate the design and validation process for energy extraction circuits by eliminating the variability and unpredictability associated with physical PEHs.

The emulator also proved valuable during the development process itself. Energy extraction circuits that initially failed to operate as intended were successfully debugged using the emulator, which provided a consistent and observable test environment. This facilitated diagnosis and iteration, highlighting the emulator's utility not only as a benchmarking platform, but also as a practical engineering tool for circuit development and troubleshooting.

5.1.2. Limitations and Future Research Opportunities

While the emulator demonstrated good agreement with the output behavior of a real PEH system, the validation process comes with several limitations that limit both the current scope. Most notably, the experimental evaluation was based on a single PEH configuration: a cantilever-based device with a PZT-5H patch-limiting the generalizability of the results to other geometries, materials, and coupling characteristics.

The emulator also does not account for back-coupling effects, where the electrical load influences the mechanical motion of the harvester. Omitting this interaction simplifies implementation and improves repeatability, since back-coupling effects are a major contributor to the chaotic behavior the emulator was designed to eliminate. However, it reduces realism in scenarios with strong electromechanical coupling. During validation, this limitation was partially mitigated by manually adjusting the input waveform, but this workaround does not fully capture dynamic feedback behavior.

Validation focused on resistive loads under single-frequency sinusoidal excitation, covering a useful but limited range of conditions. In real-world applications, excitation is often broadband or transient, and extraction circuits frequently introduce nonlinear behavior. As such, the emulator's performance under more complex conditions remains an open question.

An additional open question is how well the emulator performs in predicting *relative* circuit performance, rather than absolute power output. Even if the emulator consistently underestimates the absolute output power, as was seen to be the case, it may still correctly predict that Circuit A outperforms Circuit B by a certain margin, matching the relative performance seen in real PEH systems. If this relative ranking is preserved, the emulator could be used for accurate comparative evaluation and design space exploration, even when absolute accuracy is limited. Formal testing of this hypothesis would represent an important and practically relevant direction for future research.

The challenge of evaluating accuracy is compounded by a wide range of environmental, mechanical, and electrical factors that can influence emulator accuracy. These include temperature fluctuations, humidity, mounting conditions, material aging, impedance mismatch, emulator bandwidth limitations, and output constraints. Each of these factors can interact with the excitation signal and circuit topology in different ways, making it difficult to define a single accuracy metric. Further research is needed on how to systematically characterize these influences and to develop simplified models or bounding strategies that can estimate emulator performance under diverse scenarios. Ideally, such efforts would yield generalized error models. However, a more immediately practical approach may be to empirically characterize emulator accuracy across a representative set of PEH systems, providing reference cases that researchers can use to approximate performance for similar configurations.

In addition to these accuracy validation challenges, the emulator experienced a hardware failure during the final validation phase, traced to the power sequencing of the emulator power supplies combined with the TPS7A3901 voltage regulator (see Section 5.2.1). This failure prevented formal testing of nonlinear extraction circuits such as P-SSHI, S-SSHI, and SECE variants. Although these circuits were explored informally during earlier development and the emulator showed no signs of unexpected behavior under nonlinear loading, no structured data could be collected due to the timing of the failure.

Beyond these direct limitations, several broader questions remain. One is whether emulator-based testing can fully replace physical evaluations, or whether the two should be viewed as complementary. While the emulator enables controlled, repeatable experimentation, real PEH systems are subject to long-term effects and environmental interactions that may be difficult to emulate reliably.

Another potential area of research is the controlled reintroduction of back-coupling effects through hybrid architectures that combine analog and digital modeling. This approach could expand the emulator's applicability to systems where mechanical-electrical interactions are critical, provided it does not compromise the emulator's stability. However, care must be taken not to reintroduce the same chaotic behavior that the emulator was designed to avoid. Whether any form of back-coupling can be incorporated without triggering such instability remains an open question.

Finally, as emulator use becomes more widespread, it will be important to define standardized metrics and procedures for assessing emulator accuracy and reporting test results. Establishing a common evaluation framework, analogous to what exists in fields like photovoltaics, will be key to ensuring comparability and trust across future studies.

5.1.3. Toward Standardized PEH Emulator Platforms

The emulator presented in this work demonstrates the feasibility and utility of hardware-based emulation for piezoelectric energy harvesting systems. However, for such tools to become widely adopted in both research and industry, further development is needed toward standardized, flexible, and extensible emulator platforms.

A key step in this direction is improving modularity and repeatability in emulator design. The current prototype already supports rapid impedance reconfiguration through a dedicated connector interface that accepts standard electronic components. This makes it easy to adjust the emulator's output impedance to match different PEH systems during development and testing. Building on this, future versions could incorporate predefined or digitally selectable impedance modules, further streamlining reconfiguration and improving consistency across test setups.

To complement hardware modularity, standardization could also be supported through the creation of a shared library of impedance profiles. These profiles, based on empirical measurements of real PEH devices, could be used as references during testing. Combined with modular hardware, this would allow researchers and developers to emulate a wide range of known devices with greater accuracy and reproducibility.

In addition, to ensure reproducible and comparable results across different studies, it is important to define standard procedures for evaluating energy extraction circuits and assessing emulator performance. These could include standardized test waveforms, consistent impedance characterization methods (as discussed in Section 5.3.1), and common formats for reporting metrics such as output power versus input waveform amplitude. Together, these efforts would lay the groundwork for a broader benchmarking framework usable for anyone interested in energy extraction circuits for PEH systems.

5.2. Current Emulator Design Improvements

The general design of the emulator incorporates practical decisions that directly affect its usability, compatibility with laboratory equipment, and robustness under test conditions. This section discusses two critical aspects: the power supply related hardware faults and the choice of differential amplifier. Both areas introduce constraints that impact system functioning and measurement flexibility. Alternative solutions are presented to address these limitations and improve the overall resilience and versatility of the emulator design.

5.2.1. The Requirement for Multiple Lab Power Supplies

The current version of the emulator requires two separate power inputs: one for the positive rail and one for the negative rail. Since most laboratory power supplies capable of providing the required ± 30 V are single-channel, this setup necessitates the use of two distinct supplies. This configuration is not only impractical but also introduces a failure mode. In its present form, powering the supplies in the wrong order has been shown to damage the emulator hardware.

To step down the ± 30 V supply to levels compatible with the differential amplifier stages, a TPS7A3901 dual-channel voltage regulator [43] was used. This device generates $\pm$15 V rails from the input supplies. However, the regulator derives its internal reference voltage solely from the positive supply. Consequently, if the negative rail is applied before the positive rail, the reference voltage remains undefined, and the device may operate outside of its specified limits. This behavior likely caused the failure of one of the emulator boards during testing.

To resolve both the issue of requiring two power supplies and the associated power sequencing risk, alternative supply strategies should be considered. One common method is to use a virtual ground circuit, where an op-amp-based circuit establishes a midpoint voltage between a single supply's high and low rails. While this approach allows the creation of split rails from a single supply, it requires that the input supply cover the full voltage swing, from the negative to positive rail, meaning a 60 V range in this case. Since most lab supplies are limited to 30 V output, this is not a practical option for the current design.

A more flexible solution is to use a rail-inverting power stage, such as an inverting buck-boost converter. This type of circuit can generate a negative rail directly from a positive input voltage, allowing both the $\pm$30 V rails to be derived from a single 30 V supply. This not only simplifies the setup but also eliminates the risk of board damage due to incorrect power sequencing, as both rails can be generated internally in a controlled manner.

5.2.2. The Differential Amplifier

As discussed in Section 3.3, the emulator uses a differential amplifier to decouple the emulator output from the earth-referenced input signal. While this configuration enables floating operation and simplifies measurement integration, it introduces limitations when the emulator is used in DC-coupling mode, particularly in terms of allowable common-mode voltage. This section outlines those constraints and their implications for the emulator's compatibility with various energy extraction circuits.

A differential amplifier amplifies the voltage difference between its two inputs while rejecting signals common to both. In the context of the emulator, this common-mode voltage arises from the difference between the differential amplifier's reference ground and the average voltage seen at its two inputs. The amplifier's linearity and correct operation depend on this common-mode voltage staying within a specific range, given by

$$V_{\text{EE}} + V_{\text{headroom}} + \frac{1}{2}|V_{\text{DIFF}}| < V_{\text{CM}} < V_{\text{CC}} - V_{\text{headroom}} - \frac{1}{2}|V_{\text{DIFF}}|, \tag{5.1}$$

where:

- V_{CM} is the input common-mode voltage,
- $V_{\text{DIFF}} = V_{\text{IN+}} - V_{\text{IN-}}$ is the differential input voltage,
- V_{CC} and V_{EE} are the positive and negative supply voltages, respectively,
- V_{headroom} is the minimum input margin required for linear operation.

In the current implementation, the AD8421 instrumentation amplifier is supplied with ± 15 V. The maximum differential input signal amplitude from the AWG is 5 V, and the headroom is estimated to be 1 V. Substituting these values into the equation yields

$$|V_{\text{CM}}| < 15\,\text{V} - 1\,\text{V} - \frac{1}{2} \cdot 5\,\text{V} = 11.5\,\text{V}. \tag{5.2}$$

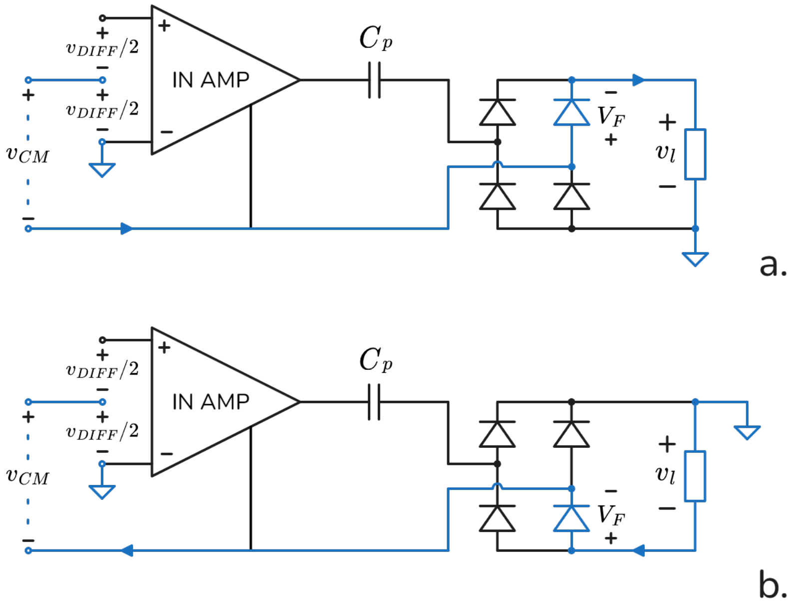

Figure 5.1: Two example SEH circuit topologies showing the resulting common-mode voltages at the differential amplifier input. Blue lines indicate the conduction path through which earth-referencing affects the amplifier. Circuit (a) yields the lowest common-mode voltage, while circuit (b) yields the highest.

This limit constrains the circuits that can be connected to the emulator without exceeding the amplifier's input range. For example, consider an energy extraction circuit where the emulator output is continuously connected to a full-bridge rectifier, such as in SEH or P-SSHI configurations. If the DC output of the rectifier is earth-referenced, a conduction path is formed from the emulator output through the differential amplifier input via earth.

Figure 5.1 illustrates two scenarios that represent the minimum and maximum common-mode voltages imposed on the amplifier inputs based on this conduction path. Applying Kirchhoff's Voltage Law (KVL) to these circuits yields

$$V_{\text{CM,min}} = \frac{V_{\text{DIFF,min}}}{2} - V_F - V_{l,\text{max}}, \tag{5.3}$$

and

$$V_{\text{CM,max}} = \frac{V_{\text{DIFF,max}}}{2} + V_F + V_{l,\text{max}}, \tag{5.4}$$

where $V_{\text{CM,min}}$ and $V_{\text{CM,max}}$ are the minimum and maximum common-mode voltages, respectively. Assuming $V_{\text{DIFF,max}}/2 = 2.5\,\text{V}$, $V_{\text{DIFF,min}}/2 = -2.5\,\text{V}$, and $V_F = 0.7\,\text{V}$, the common-mode voltage magnitude becomes

$$\max(|V_{\text{CM}}|) = 2.5\,\text{V} + 0.7\,\text{V} + V_{l,\text{max}} = 3.2\,\text{V} + V_{l,\text{max}}, \tag{5.5}$$

and, to remain within the allowable common-mode range of $11.5\,\text{V}$, the maximum permissible load voltage is

$$V_{l,\text{max}} < 8.3\,\text{V}. \tag{5.6}$$

This result shows that for certain circuit topologies with earth-referenced loads, the differential amplifier imposes a strict upper bound on allowable load voltages while in DC-coupling. In practical applications, however, achieving maximum power transfer may require load voltages that exceed this threshold. As such, this constraint is a design limitation that should be addressed.

This result shows that for certain circuit topologies with earth-referenced loads, the differential amplifier imposes a strict upper bound on allowable load voltages while in DC-coupling. In practical applications, however, achieving maximum power transfer may require load voltages that exceed this threshold. As such, this constraint is a design limitation that should be addressed.

One way to address the common-mode voltage limitation is to replace the differential amplifier with a device that supports a wider common-mode input range. An example of such a device is the isolation amplifier. These devices employ capacitive, magnetic, or optical coupling to transfer an encoded version of the input signal across an isolation barrier, effectively decoupling the input and output grounds. Isolation amplifiers can typically tolerate common-mode voltages in the kilovolt range, which would eliminate the restrictions observed in the current emulator design. The main drawback is that the input and output stages require separate power supplies, adding complexity to the system's power architecture.

5.3. Improving Emulator Accuracy

Accurately replicating the electrical behavior of a real PEH system requires both an appropriate impedance model and an emulator architecture capable of presenting that impedance under realistic conditions. The following sections explore two distinct strategies for improving emulator accuracy. The first focuses on refining the impedance model used within the emulator to better reflect the dynamic characteristics of real PEH devices. The second addresses architectural limitations of the current voltage-source-based design and proposes an alternative approach that could eliminate inherent structural inaccuracies.

5.3.1. Better Impedance Matching

As discussed in Section 4.3, the current emulator design uses a capacitor array to approximate the output impedance of a PEH system. While effective as a first-order approximation, this approach does not fully capture the dynamic electrical behavior of real piezoelectric devices. This section explores how alternative equivalent circuit models can better represent these behaviors.

The voltage and current waveforms shown earlier in Figure 4.5 reveal characteristic features that deviate from the behavior of an ideal capacitor. Under triangle wave voltage excitation, an ideal capacitive load would produce a clean, square-shaped current waveform. In contrast, the measured PEH current displays a more complex structure: a steep initial rise, followed by a rounded transition, and then a gradual ramping segment.

The rounded transition region can be attributed to dielectric relaxation, which refers to the delayed response of the material's internal polarization to changes in the electric field. At the moment the voltage begins to increase again, the material has not yet fully adjusted to the previous change in field direction. As a result, the dipoles within the material are still reorienting, and part of the polarization is effectively left over from the prior state. This residual polarization assists the initial voltage increase, meaning less external current is required during this phase. In this way, the lag in polarization leads to the curved shape observed in the current response. This behavior can be modeled by adding a parallel RC branch to the ideal capacitor, representing the time-dependent relaxation processes within the material.

Similarly, the gradual ramping region can be attributed to conductive leakage, where a small amount of current flows through the dielectric in proportion to the applied voltage. This leakage current contributes to the overall current during both charging and discharging phases. Specifically, it reduces the current required during discharge and increases the current required during charging, as the leakage flows in the same direction as the applied field. Because this behavior is approximately linear with voltage, it can be effectively modeled by placing a resistor in parallel with the capacitor.

Based on these observations, a refined impedance model is proposed that incorporates both dielectric relaxation and conductive leakage in addition to the nominal capacitance. Figure 5.2 shows both the ideal capacitive equivalent circuit model and the newly proposed equivalent circuit model, both of which

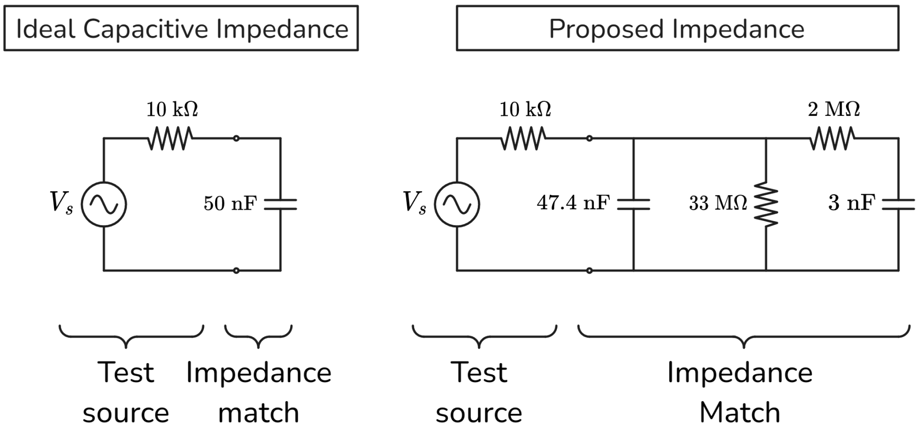

Figure 5.2: The ideal capacitive impedance circuit model (left) and the proposed equivalent circuit (right) that includes dielectric relaxation and leakage effects.

were simulated under the same test conditions described in Section 4.3.

Figure 5.3 presents the results of these simulations against real PEH current measurements. The proposed impedance model shows improved agreement with the measured waveform, particularly in replicating the shape of the curved transition and ramping regions. The left panel shows a full current cycle, while the center and right panels offer zoomed-in views of the positive and negative transitions, respectively.

These results demonstrate that a more detailed impedance match can improve the accuracy with which the emulator mimics the dynamic behavior of a real PEH. Although this particular model was fitted under one specific excitation condition, it shows clear potential. A more systematic characterization process, using a range of input frequencies and waveforms, would be required to generalize these results and identify the most robust equivalent circuit. The analysis presented here serves as a starting point and a proof of concept for this future development.

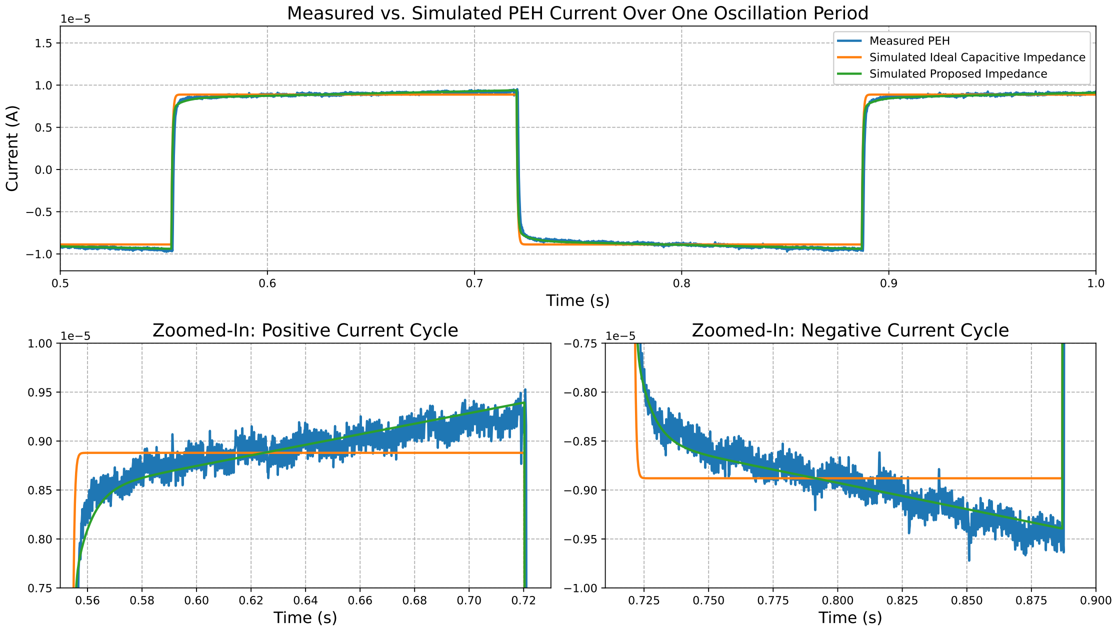

Figure 5.3: Simulated and measured current waveforms for a PEH system under triangle wave excitation. The proposed impedance model better captures transient waveform features such as the curved and ramping regions.

5.3.2. Using an AC Current Source

The previous section explored how improving the impedance match between the emulator and a real PEH system can increase accuracy. However, even with an ideal match, there remains a fundamental limitation in the current emulator design that cannot be addressed through impedance matching alone. This section outlines that limitation and proposes a potential architectural change as a direction for future research.

The source of this limitation lies in the inherent non-idealities present in all physical components. These imperfections are visible in Figure 4.5, where both the real PEH and the matched ceramic capacitor array deviate from the ideal square-wave current response expected from a linear capacitive system. In principle, this is not problematic, as long as the matched impedance, such as a capacitor array, more closely resembles an ideal capacitor than the PEH itself. If this is the case any remaining discrepancy can theoretically be corrected by including additional components in the impedance network to model the non-ideal behavior.

However, even with a perfect impedance match, the current emulator architecture introduces a limitation that leads to error. In the present design, the emulator is based on a VCVS. This implementation means that the output voltage of the emulator consists of the voltage generated by the VCVS superimposed on the voltage across the impedance network. As a result, the impedance does not experience the full output voltage in the same way a real PEH would, where the piezoelectric impedance directly experiences the output voltage.

This discrepancy is significant because the non-idealities of real components, particularly those in capacitive elements, are often voltage-dependent. If the impedance in the emulator is subjected to a different voltage than in the real PEH, the voltage-dependent behavior of the emulator's impedance naturally differ. This introduces an unavoidable accuracy penalty.

A possible solution is to redesign the emulator to use a voltage-controlled current source (VCCS) instead of a VCVS. In this configuration, shown in Figure 5.4, current is controlled by the input voltage which allows for the full output voltage to be applied across the impedance. This ensures that the emulator's impedance is subjected to exactly the same voltage as a real PEH, preserving the voltage-dependent characteristics of the system being emulated.

The primary drawback of a VCCS-based design is its added complexity. Implementing a stable and linear current source requires additional components, tight control of loop dynamics, and careful design to ensure performance across a range of output voltages and load conditions. This is in contrast to the current VCVS implementation, which relies on a relatively simple operational amplifier circuit with a small number of passive components. That design was shown to be stable and effective under both AC and DC operating conditions with minimal tuning effort.

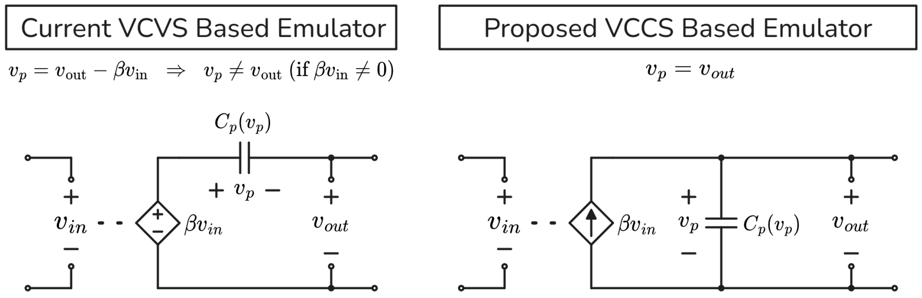

Figure 5.4: Comparison of emulator architectures. Left: current VCVS-based design, where the impedance does not experience the output voltage. Right: proposed VCCS-based design, where the impedance sees the same voltage as a real PEH.

6

Conclusion

This thesis addressed the challenge of repeatable and accurate evaluation of piezoelectric energy harvesting circuits by proposing, designing, and validating a PEH emulator. The motivation for this work stems from the complex and sometimes chaotic behavior of real nonlinear PEH systems, which hampers consistent circuit benchmarking and limits broader comparability across research efforts.

The design process began with an analysis of the functional and technical requirements for a PEH emulator. These included voltage and current capabilities, repeatable behavior, and compatibility with standard lab equipment. A voltage-controlled voltage source architecture with analog impedance modeling was chosen to meet these requirements while maintaining real-time responsiveness and avoiding latency issues associated with digital emulation.

A complete emulator circuit was developed, including input filtering, differential amplification, and a robust output buffer stage capable of handling up to ± 25 V and 3 A. The output impedance was designed to be modular and tunable, enabling adaptation to different PEH systems. Support for additional instrumentation was added to facilitate accurate measurements during circuit evaluation.

Simulation results confirmed the emulator's electrical stability across capacitive and resistive loads and under transient conditions such as voltage inversion. A physical prototype was fabricated and evaluated experimentally. Measurements confirmed low output noise and accurate gain behavior.

To validate the emulator's real-world utility, experiments compared the emulator output against the electrical characteristics of an actual PEH system under various excitation accelerations and with various resistance values as load. The emulator reproduced the measured power outputs with typical accuracy in the 80 to 100% range when comparing the output power of the emulator to that of the PEH being emulated. This is despite the emulator using a simplified impedance model.

These findings allow us to revisit the central research question posed at the start of this work: ”Is it technically feasible to develop a hardware emulator that replicates the electrical behavior of real PEH systems to support repeatable circuit evaluation?”. The results presented in this thesis clearly demonstrate that such an emulator can be built using a voltage-controlled voltage source architecture combined with analog impedance modeling. The emulator performs reliably under a wide range of electrical loading conditions and closely matches the behavior of real PEH devices.

In addition to validating the emulator, this work also identified specific limitations and proposed improvements. These include refining the impedance model to account for dielectric relaxation and leakage, replacing the differential amplifier with an isolation amplifier to expand common-mode range, and considering an architectural shift to a voltage-controlled current source to better replicate voltage-dependent impedance behavior. These future directions offer clear paths for increasing the accuracy of emulator systems.

A key contribution of this thesis is that, to the best of the author’s knowledge, it presents the first implementation of an emulator specifically for piezoelectric vibration energy harvesters. While emulator systems have already been adopted in related fields such as thermoelectric and photovoltaic energy harvesting to enable reproducible testing, no such solution has previously been proposed or demonstrated for PEH systems. By adapting this concept to piezoelectric harvesters and addressing their unique challenges such as capacitive source behavior and high peak currents, this work fills an important gap in the energy harvesting research landscape.

In closing, this work demonstrates that a PEH emulator based on a voltage-controlled voltage source architecture and analog impedance modeling can serve as a powerful tool for characterizing energy extraction circuit performance. It enables consistent, reproducible testing while decoupling circuit performance from the complex dynamics of physical nonlinear harvesters. As energy harvesting systems continue to grow in complexity and application scope, tools such as the PEH emulator will be essential for accelerating development, comparison, and optimization of energy extraction circuit solutions.

References

[1] E. Brusa, A. Carrera, and C. Delprete, “A Review of Piezoelectric Energy Harvesting: Materials, Design, and Readout Circuits,” *Actuators*, vol. 12, no. 12, p. 457, 12 Dec. 2023, ISSN: 2076-0825. DOI: `10.3390/act12120457`. [Online]. Available: `https://www.mdpi.com/2076-0825/12/12/457` (visited on 09/19/2024).

[2] L. Zhou, J. Sun, X. J. Zheng, *et al.*, “A model for the energy harvesting performance of shear mode piezoelectric cantilever,” *Sensors and Actuators A: Physical*, vol. 179, pp. 185–192, Jun. 1, 2012, ISSN: 0924-4247. DOI: `10.1016/j.sna.2012.02.041`. [Online]. Available: `https://www.sciencedirect.com/science/article/pii/S0924424712001549` (visited on 07/15/2025).

[3] Q. Li, C. Wang, C. Liu, Z. Li, X. Liu, and L. He, “Development Trend of Nonlinear Piezoelectric Energy Harvesters,” *Journal of Electronic Materials*, vol. 54, no. 1, pp. 1–23, 1 Jan. 1, 2025, ISSN: 1543-186X. DOI: `10.1007/s11664-024-11575-y`. [Online]. Available: `https://link.springer.com/article/10.1007/s11664-024-11575-y` (visited on 07/07/2025).

[4] J. Ghazanfarian, M. M. Mohammadi, and K. Uchino, “Piezoelectric Energy Harvesting: A Systematic Review of Reviews,” *Actuators*, vol. 10, no. 12, p. 312, 12 Dec. 2021, ISSN: 2076-0825. DOI: `10.3390/act10120312`. [Online]. Available: `https://www.mdpi.com/2076-0825/10/12/312` (visited on 07/07/2025).

[5] A. Morel, Q. Demouron, and A. Badel. “Enhancing Bistable Vibration Energy Harvesters with Tunable Circuits: A Comparative Analysis.” arXiv: `2409.00469`. (Aug. 31, 2024), [Online]. Available: `http://arxiv.org/abs/2409.00469` (visited on 11/13/2024), pre-published.

[6] C. Cheng, Z. Chen, Y. Xiong, H. Shi, and Y. Yang, “A high-efficiency, self-powered nonlinear interface circuit for bi-stable rotating piezoelectric vibration energy harvesting with nonlinear magnetic force,” *International Journal of Applied Electromagnetics and Mechanics*, vol. 51, no. 3, pp. 235–248, Jul. 8, 2016, ISSN: 13835416, 18758800. DOI: `10.3233/JAE-150093`. [Online]. Available: `https://www.medra.org/servlet/aliasResolver?alias=iospress&doi=10.3233/JAE-150093` (visited on 11/01/2024).

[7] A. Morel, A. Brenes, D. Gibus, *et al.*, “A comparative study of electrical interfaces for tunable piezoelectric vibration energy harvesting,” *Smart Materials and Structures*, vol. 31, no. 4, p. 045 016, Mar. 2022, ISSN: 0964-1726. DOI: `10.1088/1361-665X/ac54e8`. [Online]. Available: `https://dx.doi.org/10.1088/1361-665X/ac54e8` (visited on 11/13/2024).

[8] A. Tabesh and L. Fréchette, “On the concepts of electrical damping and stiffness in the design of a piezoelectric bending beam energy harvester,” Jan. 1, 2009. [Online]. Available: `https://scispace.com/papers/on-the-concepts-of-electrical-damping-and-stiffness-in-the-4jvai0dq4v` (visited on 07/15/2025).

[9] M. A. Trindade and A. Benjeddou, “Effective electromechanical coupling coefficients of piezoelectric adaptive structures: Critical evaluation and optimization,” *Mechanics of Advanced Materials and Structures*, vol. 16, no. 3, pp. 210–223, 2009. DOI: `10.1080/15376490902746863`. [Online]. Available: `https://doi.org/10.1080/15376490902746863` (visited on 07/07/2025).

[10] H. Shen, H. Ji, J. Qiu, Y. Bian, and D. Liu, “Adaptive synchronized switch harvesting: A new piezoelectric energy harvesting scheme for wideband vibrations,” *Sensors and Actuators A: Physical*, vol. 226, pp. 21–36, May 1, 2015, ISSN: 0924-4247. DOI: `10.1016/j.sna.2015.02.008`. [Online]. Available: `https://www.sciencedirect.com/science/article/pii/S0924424715000655` (visited on 09/03/2024).

[11] E. Lefeuvre, A. Badel, C. Richard, and D. Guyomar, “Piezoelectric energy harvesting device optimization by synchronous charge extraction,” *Journal of Intelligent Material Systems and Structures*, vol. 16, pp. 865–876, Oct. 1, 2005. DOI: `10.1177/1045389X05056859`.

[12] L. Mamouri and V. Frick, “Adaptive FOCV MPPT for Piezoelectric Energy Harvesting Circuit,” in *2023 21st IEEE Interregional NEWCAS Conference (NEWCAS)*, Jun. 2023, pp. 1–5. DOI: `10.1109/NEWCAS57931.2023.10198164`. [Online]. Available: `https://ieeexplore.ieee.org/document/10198164/?arnumber=10198164` (visited on 03/06/2025).

[13] A. B. Alamin Dow, A. Bittner, U. Schmid, and N. P. Kherani, “Design, fabrication and testing of a piezoelectric energy microgenerator,” *Microsystem Technologies*, vol. 20, no. 4, pp. 1035–1040, 4 Apr. 1, 2014, ISSN: 1432-1858. DOI: `10.1007/s00542-014-2116-9`. [Online]. Available: `https://link.springer.com/article/10.1007/s00542-014-2116-9` (visited on 04/09/2025).

[14] B. Zhang, H. Zhou, X. Zhao, J. Gao, and S. Zhou, “Design and experimental analysis of a piezoelectric energy harvester based on stacked piezoceramic for nonharmonic excitations,” *Energy*, vol. 282, p. 128 948, Nov. 2023, ISSN: 03605442. DOI: `10.1016/j.energy.2023.128948`. [Online]. Available: `https://linkinghub.elsevier.com/retrieve/pii/S0360544223023423` (visited on 04/09/2025).

[15] S. Roundy and P. K. Wright, “A piezoelectric vibration based generator for wireless electronics,” *Smart Materials and Structures*, vol. 13, no. 5, p. 1131, Aug. 2004, ISSN: 0964-1726. DOI: `10.1088/0964-1726/13/5/018`. [Online]. Available: `https://dx.doi.org/10.1088/0964-1726/13/5/018` (visited on 10/08/2024).

[16] M. Lallart, L. Garbuio, L. Petit, C. Richard, and D. Guyomar, “Double synchronized switch harvesting (DSSH): A new energy harvesting scheme for efficient energy extraction,” *IEEE Transactions on Ultrasonics, Ferroelectrics, and Frequency Control*, vol. 55, no. 10, pp. 2119–2130, Oct. 2008, ISSN: 1525-8955. DOI: `10.1109/TUFFC.912`. [Online]. Available: `https://ieeexplore.ieee.org/document/4638899` (visited on 03/05/2025).

[17] S. Basaran, “Hybrid energy harvesting system under the electromagnetic induced vibrations with non-rigid ground connection,” *Mechanical Systems and Signal Processing*, vol. 163, p. 108 198, Jan. 2022, ISSN: 08883270. DOI: `10.1016/j.ymssp.2021.108198`. [Online]. Available: `https://linkinghub.elsevier.com/retrieve/pii/S0888327021005744` (visited on 04/09/2025).

[18] L. Sun, L. Feng, B. Yang, *et al.*, “Design and Study of a Rotating Piezoelectric Energy Harvester with Dual Excitation Modules,” *Journal of Electronic Materials*, vol. 53, no. 7, pp. 4197–4213, 7 Jul. 1, 2024, ISSN: 1543-186X. DOI: `10.1007/s11664-024-11116-7`. [Online]. Available: `https://link.springer.com/article/10.1007/s11664-024-11116-7` (visited on 04/09/2025).

[19] M. Yao, P. Liu, L. Ma, H. Wang, and W. Zhang, “Experimental study on broadband bistable energy harvester with L-shaped piezoelectric cantilever beam,” *Acta Mechanica Sinica*, vol. 36, no. 3, pp. 557–577, 3 Jun. 1, 2020, ISSN: 1614-3116. DOI: `10.1007/s10409-020-00956-1`. [Online]. Available: `https://link.springer.com/article/10.1007/s10409-020-00956-1` (visited on 04/09/2025).

[20] S. C. Stanton, C. C. McGehee, and B. P. Mann, “Nonlinear dynamics for broadband energy harvesting: Investigation of a bistable piezoelectric inertial generator,” *Physica D: Nonlinear Phenomena*, vol. 239, no. 10, pp. 640–653, May 15, 2010, ISSN: 0167-2789. DOI: `10.1016/j.physd.2010.01.019`. [Online]. Available: `https://www.sciencedirect.com/science/article/pii/S0167278910000394` (visited on 04/10/2025).

[21] R. Ayop and C. W. Tan, “A comprehensive review on photovoltaic emulator,” *Renewable and Sustainable Energy Reviews*, vol. 80, pp. 430–452, Dec. 2017, ISSN: 13640321. DOI: `10.1016/j.rser.2017.05.217`. [Online]. Available: `https://linkinghub.elsevier.com/retrieve/pii/S1364032117308535` (visited on 04/09/2025).

[22] T. Dhanush and A. Sinha, *Microcontroller Based Design of a Simulation System for Energy Harvesting Application*. Nov. 5, 2022.

[23] E. A. Man, D. Sera, L. Máthé, E. Schaltz, and L. A. Rosendahl, “Thermoelectric generator emulator for MPPT testing,” in *Proc. 2015 ACEMP–OPTIM–ELECTROMOTION Joint Conf.*, IEEE, Sep. 2015, pp. 774–778, ISBN: 978-1-4673-7240-4. DOI: `10.1109/OPTIM.2015.7427051`. [Online]. Available: `https://doi.org/10.1109/OPTIM.2015.7427051`.

[24] D. Guyomar, A. Badel, E. Lefeuvre, and C. Richard, “Toward energy harvesting using active materials and conversion improvement by nonlinear processing,” *IEEE Transactions on Ultrasonics, Ferroelectrics, and Frequency Control*, vol. 52, no. 4, pp. 584–595, Apr. 2005, ISSN: 1525-8955. DOI: `10.1109/TUFFC.2005.1428041`. [Online]. Available: `https://ieeexplore.ieee.org/abstract/document/1428041` (visited on 03/05/2025).

[25] G. Taylor, J. Burns, S. Kammann, W. Powers, and T. Welsh, “The Energy Harvesting Eel: A small subsurface ocean/river power generator,” *IEEE Journal of Oceanic Engineering*, vol. 26, no. 4, pp. 539–547, Oct. 2001, ISSN: 1558-1691. DOI: `10.1109/48.972090`. [Online]. Available: `https://ieeexplore.ieee.org/document/972090/?arnumber=972090` (visited on 03/05/2025).

[26] Z. Zhang, H. Xiang, and L. Tang, “Modeling, analysis and comparison of four charging interface circuits for piezoelectric energy harvesting,” *Mechanical Systems and Signal Processing*, vol. 152, p. 107 476, May 1, 2021, ISSN: 0888-3270. DOI: `10.1016/j.ymssp.2020.107476`. [Online]. Available: `https://www.sciencedirect.com/science/article/pii/S0888327020308621` (visited on 07/15/2025).

[27] T. Martinez, G. Pillonnet, and F. Costa, “A 15-mV Inductor-Less Start-up Converter Using a Piezoelectric Transformer for Energy Harvesting Applications,” *IEEE Transactions on Power Electronics*, vol. 33, no. 3, pp. 2241–2253, Mar. 2018, ISSN: 1941-0107. DOI: `10.1109/TPEL.2017.2690804`. [Online]. Available: `https://ieeexplore.ieee.org/document/7892016` (visited on 03/11/2025).

[28] X. Yue, J. Mo, Z. Chen, S. Vollebregt, G. Zhang, and S. Du, “A Fully Integrated Sequential Synchronized Switch Harvesting on Capacitors Rectifier Based on Split- Electrode for Piezoelectric Energy Harvesting,” *IEEE Transactions on Power Electronics*, vol. 39, no. 6, pp. 7643–7653, Jun. 2024, ISSN: 1941-0107. DOI: `10.1109/TPEL.2024.3369728`. [Online]. Available: `https://ieeexplore.ieee.org/document/10444906` (visited on 09/01/2024).

[29] J. Qiu, H. Jiang, H. Ji, and K. Zhu, “Comparison between four piezoelectric energy harvesting circuits,” *Frontiers of Mechanical Engineering in China*, vol. 4, no. 2, pp. 153–159, Jun. 1, 2009, ISSN: 1673-3592. DOI: `10.1007/s11465-009-0031-z`. [Online]. Available: `https://doi.org/10.1007/s11465-009-0031-z` (visited on 09/03/2024).

[30] J. H. You, “Comparison study of standard, conventional SSHI and self-powered SSHI interface circuits in piezoelectric energy conversion,” [Online]. Available: `https://www.academia.edu/31738047/Comparison_study_of_standard_conventional_SSHI_and_self_powered_SSHI_interface_circuits_in_piezoelectric_energy_conversion` (visited on 07/16/2025).

[31] M. Abdel-Salam, M.-T. El-Mohandes, and M. Goda, “An improved perturb-and-observe based MPPT method for PV systems under varying irradiation levels,” *Solar Energy*, vol. 171, pp. 547–561, Sep. 1, 2018, ISSN: 0038-092X. DOI: `10.1016/j.solener.2018.06.080`. [Online]. Available: `https://www.sciencedirect.com/science/article/pii/S0038092X18306315` (visited on 07/15/2025).

[32] J. Ahmad, “A fractional open circuit voltage based maximum power point tracker for photovoltaic arrays,” in *2010 2nd International Conference on Software Technology and Engineering*, vol. 1, Oct. 2010, pp. V1-247-V1–250. DOI: `10.1109/ICSTE.2010.5608868`. [Online]. Available: `https://ieeexplore.ieee.org/document/5608868` (visited on 07/15/2025).

[33] S. Fang, H. Xia, Y. Xia, *et al.*, “An Efficient Piezoelectric Energy Harvesting Circuit With Series-SSHI Rectifier and FNOV-MPPT Control Technique,” *IEEE Transactions on Industrial Electronics*, vol. 68, no. 8, pp. 7146–7155, Aug. 2021, ISSN: 1557-9948. DOI: `10.1109/TIE.2020.3007054`. [Online]. Available: `https://ieeexplore.ieee.org/document/9138753` (visited on 11/29/2024).

[34] Y. Wu, A. Badel, F. Formosa, W. Liu, and A. E. Agbossou, “Piezoelectric vibration energy harvesting by optimized synchronous electric charge extraction,” *Journal of Intelligent Material Systems and Structures*, vol. 24, no. 12, pp. 1445–1458, Aug. 1, 2013, ISSN: 1045-389X. DOI: `10.1177/1045389X12470307`. [Online]. Available: `https://doi.org/10.1177/1045389X12470307` (visited on 07/15/2025).

[35] C. Richard, D. Guyomar, and E. Lefeuvre, “Self-powered electronic breaker with automatic switching by detecting maxima or minima of potential difference between its power electrodes,” pat. WO/2007/063194, PCT/FR2005/003000, 2007.

[36] X.-F. Shen, T.-C. Yuan, J. Yang, *et al.*, “Bias-Voltage-SSHI Interface Circuit for Strong Coupling Piezoelectric Energy Systems,” *IEEE Transactions on Power Electronics*, vol. 38, no. 9, pp. 11 568–11 584, Sep. 2023, ISSN: 1941-0107. DOI: `10.1109/TPEL.2023.3282179`. [Online]. Available: `https://ieeexplore.ieee.org/abstract/document/10143264` (visited on 09/11/2024).

[37] M. Lallart and D. Guyomar, “An optimized self-powered switching circuit for non-linear energy harvesting with low voltage output,” *Smart Materials and Structures*, vol. 17, no. 3, p. 035 030, May 2008, ISSN: 0964-1726. DOI: `10.1088/0964-1726/17/3/035030`. [Online]. Available: `https://dx.doi.org/10.1088/0964-1726/17/3/035030` (visited on 03/05/2025).

[38] K. Savarimuthu, R. Sankararajan, and S. Murugesan, “Analysis and design of power conditioning circuit for piezoelectric vibration energy harvester,” *IET Science, Measurement & Technology*, vol. 11, no. 6, pp. 723–730, 2017, ISSN: 1751-8830. DOI: `10.1049/iet-smt.2016.0377`. [Online]. Available: `https://onlinelibrary.wiley.com/doi/abs/10.1049/iet-smt.2016.0377` (visited on 09/09/2024).

[39] K. A. Cook-Chennault, N. Thambi, and A. M. Sastry, “Powering MEMS portable devices—a review of non-regenerative and regenerative power supply systems with special emphasis on piezoelectric energy harvesting systems,” *Smart Materials and Structures*, vol. 17, no. 4, p. 043 001, Jun. 2008, ISSN: 0964-1726. DOI: `10.1088/0964-1726/17/4/043001`. [Online]. Available: `https://dx.doi.org/10.1088/0964-1726/17/4/043001` (visited on 07/17/2025).

[40] Analog Devices. “AD8421 Data Sheet: Low-Noise, High-Speed Instrumentation Amplifier.” Instrumentation amplifier: 3 nV/√Hz input noise, 10 MHz bandwidth (G=1), gain set by single resistor, inputs protected to 40 V beyond supply rails. (2020), [Online]. Available: `https://www.analog.com/en/products/ad8421.html` (visited on 04/23/2025).

[41] Texas Instruments. “OPA544 data sheet, product information and support.” (2025), [Online]. Available: `https://www.ti.com/product/OPA544` (visited on 07/16/2025).

[42] Joulescope. “Joulescope JS220: Precision Energy Analyzer.” Precision DC energy analyzer measuring current from nanoamps to amps and voltage simultaneously; features ±15 V voltage range, ±3 A continuous current (10 A pulses), 0.5 nA resolution, 300 kHz bandwidth, and 2 million samples/s. (2024), [Online]. Available: `https://www.joulescope.com/products/js220-joulescope-precision-energy-analyzer` (visited on 04/24/2025).

[43] Texas Instruments. “TPS7A39 data sheet: Dual high-psrr positive & negative ldos.” Dual-channel high-PSRR low-dropout regulator (±3.3 V to ±33 V in, ±1.2 V to ±30 V out, up to 150 mA sink/-source per channel). (2025), [Online]. Available: `https://www.ti.com/product/TPS7A39` (visited on 07/15/2025).

[44] K. Song, M. Bonnin, F. Traversa, and F. Bonani, “Stochastic analysis of a bistable piezoelectric energy harvester with a matched electrical load,” *Nonlinear Dynamics*, vol. 111, pp. 1–15, Jul. 26, 2023. DOI: `10.1007/s11071-023-08746-7`.

[45] Y. C. Shu and I. C. Lien, “Efficiency of energy conversion for a piezoelectric power harvesting system,” *Journal of Micromechanics and Microengineering*, vol. 16, no. 11, p. 2429, Sep. 2006, ISSN: 0960-1317. DOI: `10.1088/0960-1317/16/11/026`. [Online]. Available: `https://dx.doi.org/10.1088/0960-1317/16/11/026` (visited on 07/24/2025).

A

Mathematical Derivations

A.1. The Force Voltage Factor α

This section outlines the method for determining the force voltage factor of a SDOF system. Based on the dynamics equation in Equation 1.2, we can expect the relationship, for open-circuit conditions ($i = 0$),

$$\alpha \frac{dx}{dt} - C_p \frac{dv_p}{dt} = 0, \tag{A.1}$$

Moving the constants and integrating both sides gives

$$v_p = \int \frac{dv_p}{dt}\, dt = \int \frac{\alpha}{C_p} \frac{dx}{dt}\, dt, \tag{A.2}$$

which, assuming the voltage v_p is zero when the displacement x is zero, becomes

$$v_p = \frac{\alpha}{C_p} x. \tag{A.3}$$

As shown in [44], if we measure both displacement and voltage at the same time, we have $v = V_{OC}$ and $x = X_{OC}$, giving

$$\alpha = \frac{V_{\text{OC}}}{X_{\text{OC}}} C_p. \tag{A.4}$$

Measuring both values at their respective maximum points provides a straightforward way to estimate α, since these maxima occur at the same time, as indicated by Equation A.3. However, this derivation assumes linear piezoelectric behavior. In practice, α is likely to be a nonlinear function of both displacement x and piezoelectric voltage v, and the same applies to the piezoelectric capacitance C_p, which may also exhibit nonlinearities.

A.2. The Expedient Electromechanical Coupling Coefficient k_m^2

The electromechanical coupling coefficient is defined as the ratio of the electrical energy to the mechanical energy,

$$k_m^2 = \frac{E_{\text{elec}}}{E_{\text{mech}}}, \tag{A.5}$$

where the mechanical energy stored in the system is

$$E_{\text{mech}} = \frac{1}{2}Kx^2, \tag{A.6}$$

assuming K is constant and not a function of x, and the electrical energy stored in the system is

$$E_{\text{elec}} = \frac{1}{2}C_p v^2. \tag{A.7}$$

Substituting Equation A.3 into the expression for electrical energy yields

$$E_{\text{elec}} = \frac{1}{2}C_p \left(\frac{\alpha}{C_p}x\right)^2 = \frac{1}{2}\frac{\alpha^2}{C_p}x^2. \tag{A.8}$$

Filling in the expressions for electrical and mechanical energy gives

$$k_m^2 = \frac{\frac{1}{2}\frac{\alpha^2}{C_p}x^2}{\frac{1}{2}Kx^2} = \frac{\alpha^2}{KC_p}, \tag{A.9}$$

as noted in [45]. This assumes the stiffness K is linear. In a bistable system, K will be a function of displacement, $K(x)$, which changes the mechanical energy to

$$E_{\text{mech}}(x) = \int_0^x F(x')\,dx' = \int_0^x K(x')\cdot x'\,dx'. \tag{A.10}$$

Not accounting for these nonlinear factors is what makes this calculation of the coupling factor “expedient” in the case of nonlinear harvesters. It provides only a rough estimation of the true coupling factor, which will depend on displacement.

B

PEH Emulator Schematic

An overview of the complete emulator circuit, as designed in Altium Designer, is shown in the schematic below.

Input amplifier stage

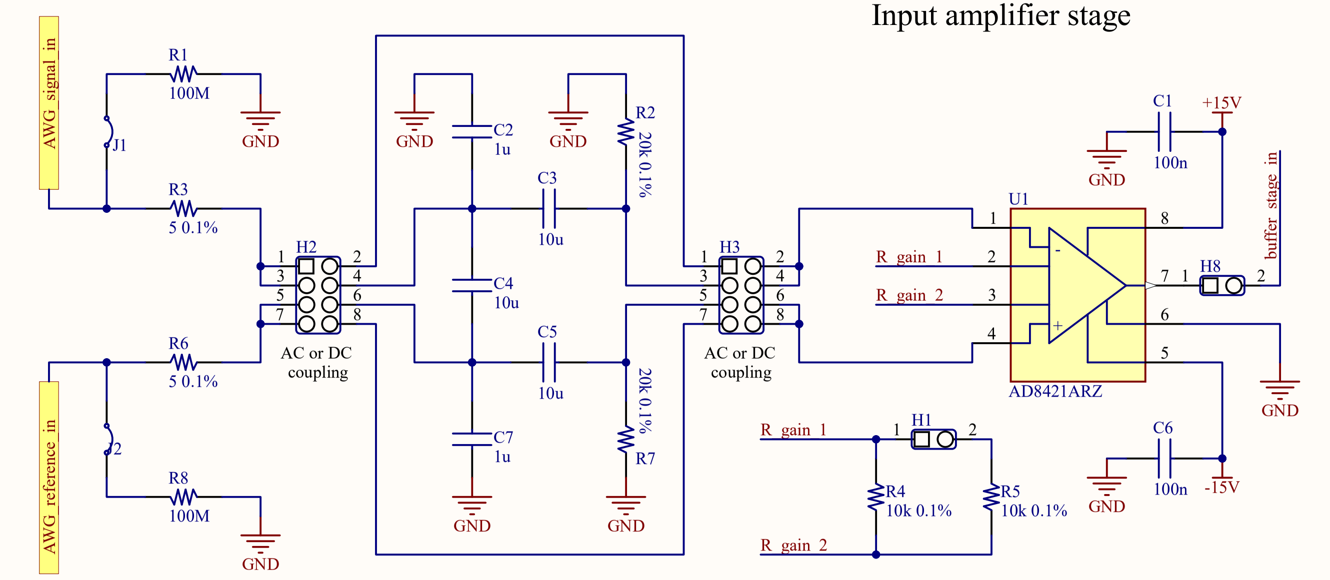

LPF differential cutoff: 1/(2π 5 (2 10u + 1u)) = 1515 Hz
LPF common mode cutoff: 1/(2π 5 1u) = 32 kHz

HPF cutoff: 1/(2π 5 10u) = 0.8 Hz

By bridging H1 the gain can be changed from 2 to 3

Buffer amplifier stage

The buffer stage generates the high voltages and currents required to test synchronous switching based energy extraction circuits.

Gain: 3 (for a total of 6 or 12 depending on the INA)

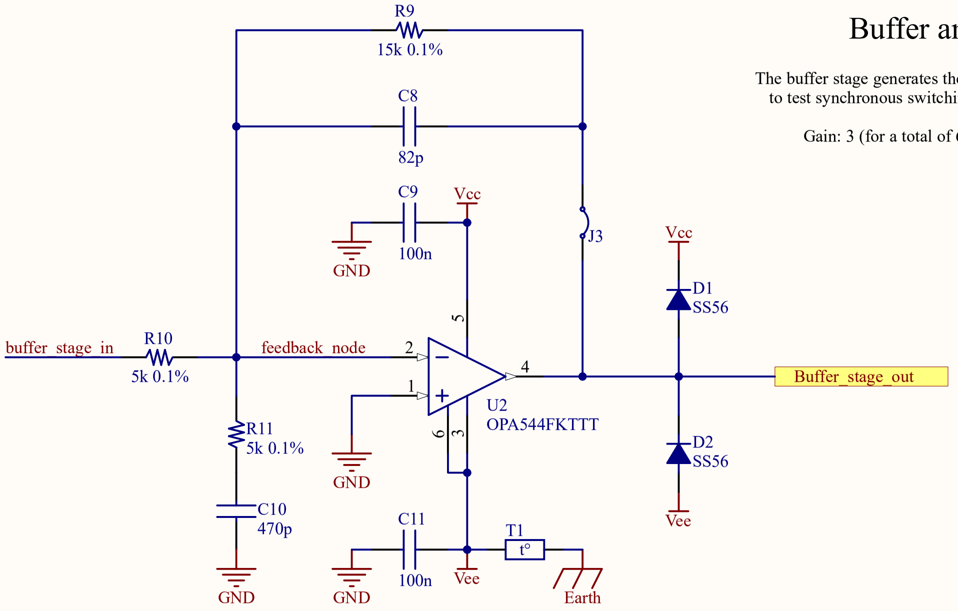

The piezo emulator

This circuit emulates a vibrational piezoelectric harvester by modeling it as a voltage source with a series and parralel impedance. The series and parralel impedance can be configured using through hole components. The voltage source is implemented via two amplifier stages controlled controlled using an AWG.

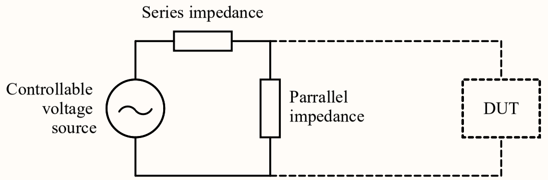

AWG outputs are mostly earth referenced. This could cause issues if the DUT has, for example, a FBR rectifier and one wishes to measure the DC output with an oscilloscope. By using a non-differential oscilloscope probe one would short part of the FBR. This issue is solved by using an instrumentation amplifier as an input stage which allows the output of the system to be floating w.r.t. earth (as long as the common mode input limitations of the instumentation amplifier are respected)

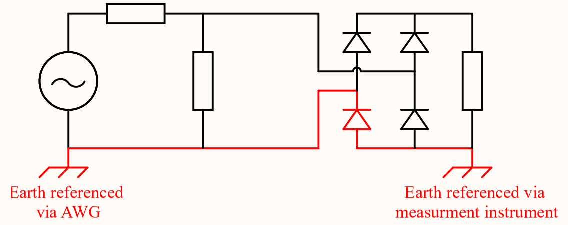

By using a instrumentation amplifier (INA) on the input stage we can solve this issue. This gives more freedom in terms of what point to use as earth reference in the DUT. The opamp after the INA is meant to increase the amount of current and the voltage range of the output

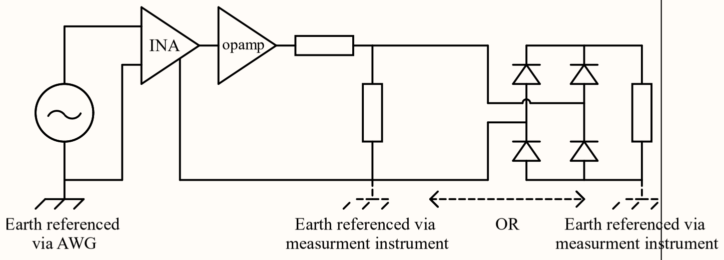

The circuit attempts to keep the common mode voltage at the input of the INA as low as possible. This common mode voltage is dependent on the conditions of the DUT and should not exeed the spec.

Title			
Size A4	Number		Revision
Date:	7/02/2025	Sheet of	
File:	C:\Users\..\Main.SchDoc	Drawn By:	

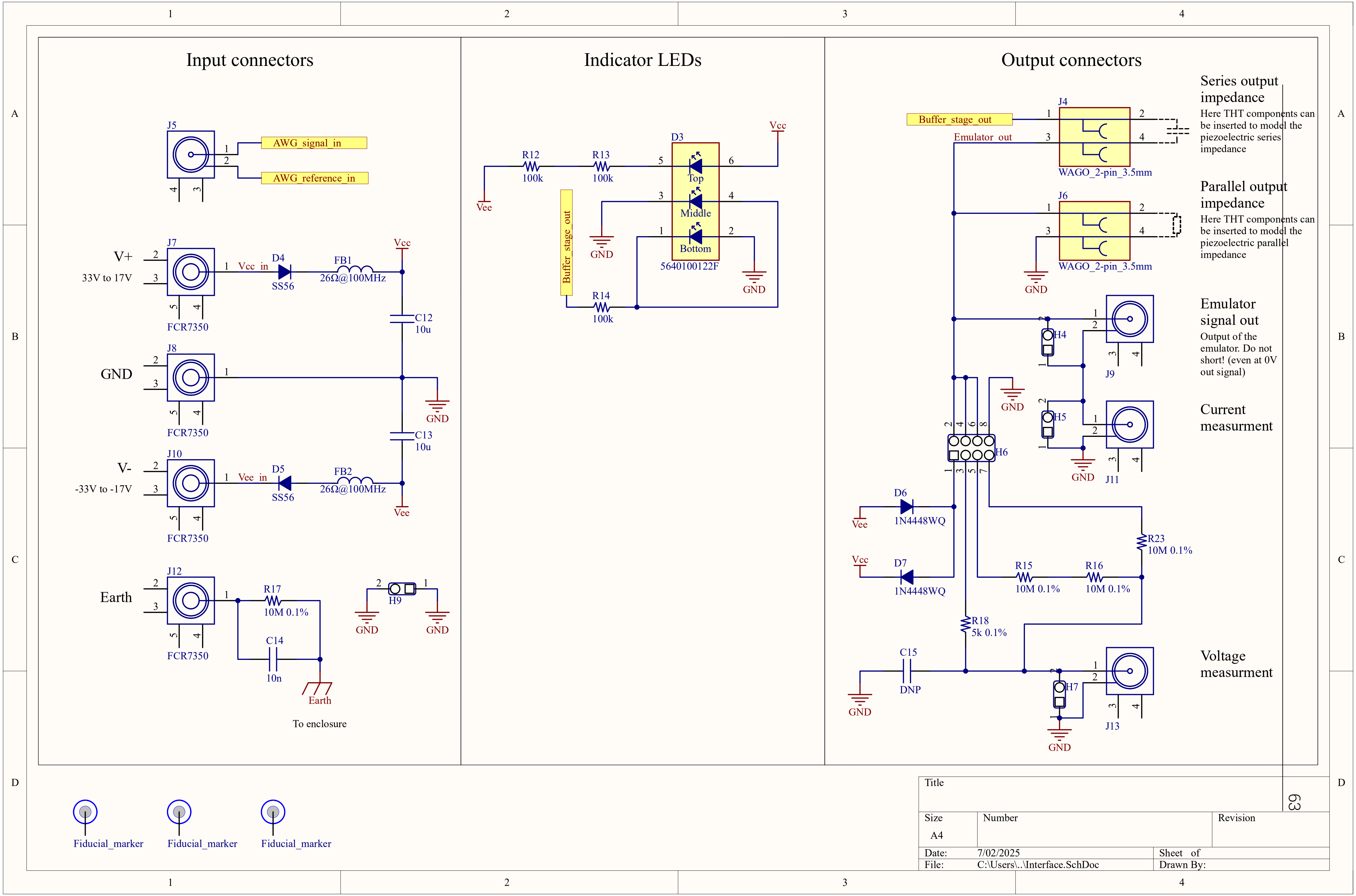
Input connectors
Indicator LEDs
Output connectors
J5
AWG_signal_in
AWG_reference_in
J7
V+
33V to 17V
Vcc_in
D4
SS56
FB1
26Ω@100MHz
Vcc
C12
10u
FCR7350
J8
GND
C13
10u
J10
V-
-33V to -17V
Vee_in
D5
SS56
FB2
26Ω@100MHz
Vee
J12
Earth
R17
10M 0.1%
C14
10n
To enclosure
H9
R12
100k
R13
100k
R14
100k
Buffer_stage_out
D3
Top
Middle
Bottom
5640100122F
Series output impedance
Here THT components can be inserted to model the piezoelectric series impedance
J4
WAGO_2-pin_3.5mm
Emulator_out
Parallel output impedance
Here THT components can be inserted to model the piezoelectric parallel impedance
J6
Emulator signal out
Output of the emulator. Do not short! (even at 0V out signal)
H4
J9
Current measurment
H5
J11
H6
D6
1N4448WQ
D7
1N4448WQ
R23
10M 0.1%
R15
10M 0.1%
R16
10M 0.1%
R18
5k 0.1%
C15
DNP
Voltage measurment
H7
J13
Fiducial_marker
Fiducial_marker
Fiducial_marker
Title
Size
A4
Number
Revision
Date:
7/02/2025
Sheet of
File:
C:\Users\..\Interface.SchDoc
Drawn By:

REVISION	DESCRIPTION	DATE	APPROVED

Dual rail LDO

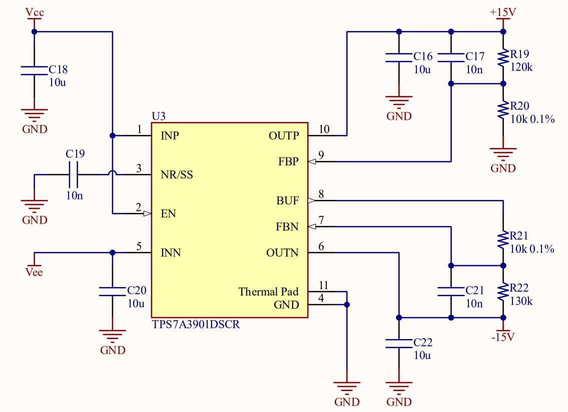

VOUTP = 1.19 × (1 + 120k / 10k) = 15.47V
VOUTN = 1.19 × (-130k / 10k) = -15.47V

APPROVALS		DATE
ENG:	*	--/--/--
DSN:	*	--/--/--
CHK:	*	--/--/--

REFERENCE DOCUMENTS
BOM:
ASSY DWG:
FAB DWG:
PCB DWG:

PROJECT
*

ADDRESS 1
ADDRESS 2
ADDRESS 3
ADDRESS 4

PROJECT REVISION: 09d6b858772b0ef1c5867[illegible]4590728e034b2e
DOCUMENT REVISION:
DESIGN ITEM:
4

TITLE
*

SIZE B
CAGE CODE
DWG NO.
REV

SCALE:
FILE NAME Power_fixed.SchDoc
SHEET 3 OF 3

DWG. NO. REV. SHT. 3

C

PEH Emulator User Guide

This appendix provides a practical overview of how to correctly set up and operate the PEH emulator for evaluating energy extraction circuits. The emulator replicates the electrical behavior of a PEH systems and is intended for use with standard laboratory instrumentation. This section details the required equipment, electrical connections, and instrumentation configuration to ensure safe and effective usage. The goal is to assist future users in performing circuit evaluations under.

Required Equipment

The following equipment is required to operate the emulator:

- PEH emulator unit (as described in Chapter 3)
- Two laboratory power supplies capable of sourcing $\pm 30\,\mathrm{V}$ (used to power the emulator)
- One additional lab power supply or variable resistance box (used to emulate a load in certain configurations)
- AWG, such as the Analog Discovery 3
- Two Joulescope JS220 precision energy analyzers (or equivalent voltage and current meters)
- Swappable impedance components (C_p) for emulator output configuration
- Circuit under test (e.g., SEH, SSHI, or SECE extraction circuit)

System Overview

Figure C.1 shows the full laboratory setup used to operate the emulator. Each labeled component corresponds to a block in the schematic shown in Figure C.2, which provides a wiring diagram of the full system.

- The Analog Discovery 3 is used to replay pre-recorded open-circuit voltage waveforms from a real PEH system.
- These waveforms are fed into the emulator's AWG input via BNC connector.
- The emulator amplifies the signal and presents it at the output, with a configurable impedance matching network to replicate the characteristics of a real PEH. By default, the gain of the emulator is 6 so divide any desired output signal by 6 for the AWG output.
- The emulator output connects directly to the input of the energy extraction circuit under test.
- Input and output power are measured using two Joulescope JS220 devices. These instruments capture time-aligned voltage and current waveforms with high dynamic range.

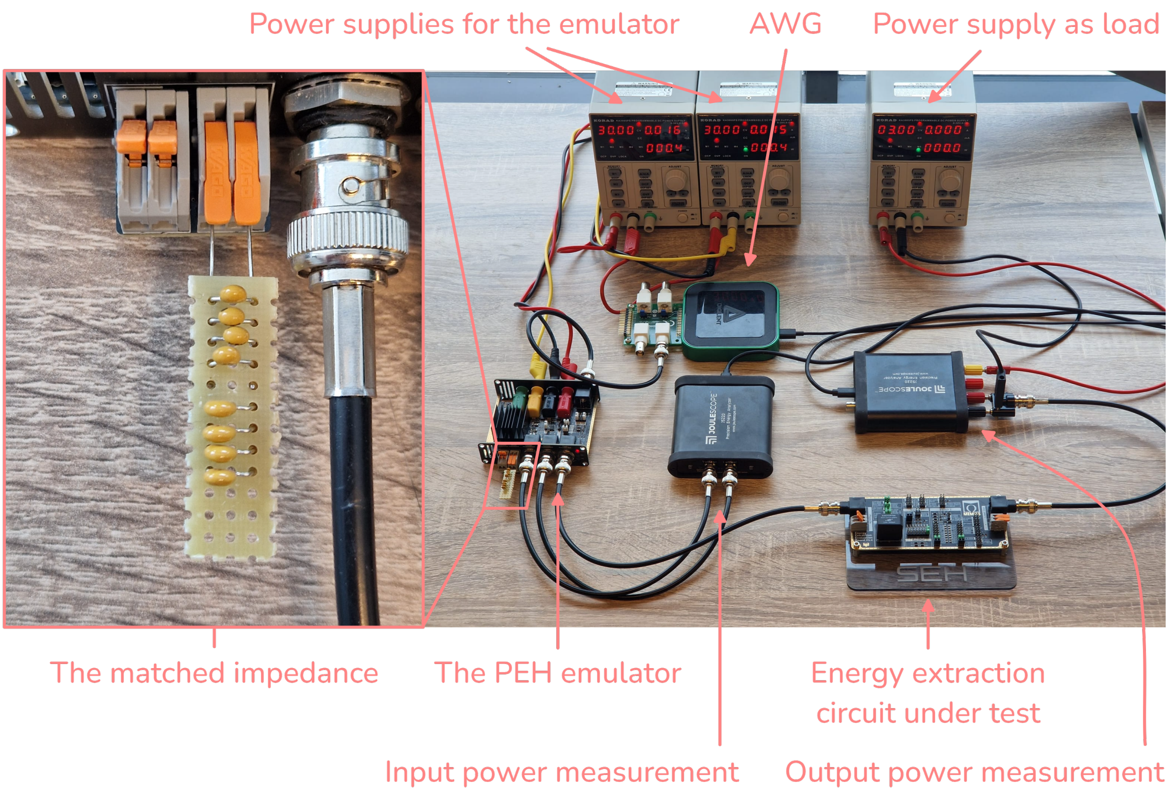

Figure C.1: Physical setup for using the PEH emulator. All major components including the waveform generator, emulator, Joulescopes, and power supplies are labeled.

Connection Instructions

Refer to Figure C.2 for the following steps:

1. **Power supplies:**
    - Connect one lab power supply to the positive rail input (V_{cc}) and another to the negative rail input (V_{ee}).
    - Ensure V_{cc} is turned on before V_{ee} to avoid damaging the internal voltage regulator (see Section 5.2.1).
2. **Waveform input:**
    - Connect the AWG output from the Analog Discovery 3 to the emulator's waveform input using a BNC cable.
    - Set the signal amplitude such that, after emulator gain, the output voltage matches the target PEH waveform (typically up to $\pm 25\,\mathrm{V}$ peak).
3. **Impedance configuration:**
    - Select and insert appropriate through-hole components at the output sockets to model tie series output impedance C_p.
    - A typical starting value is $C_p = 50\,\mathrm{nF}$, but this can be adapted to match the device under emulation.
4. **Circuit under test:**
    - Connect the emulator output to the input of the energy extraction circuit.
    - Ensure that any rectifiers or DC links in the circuit are compatible with the floating output of the emulator (see Section 5.2.2 for some limitations in this regard).

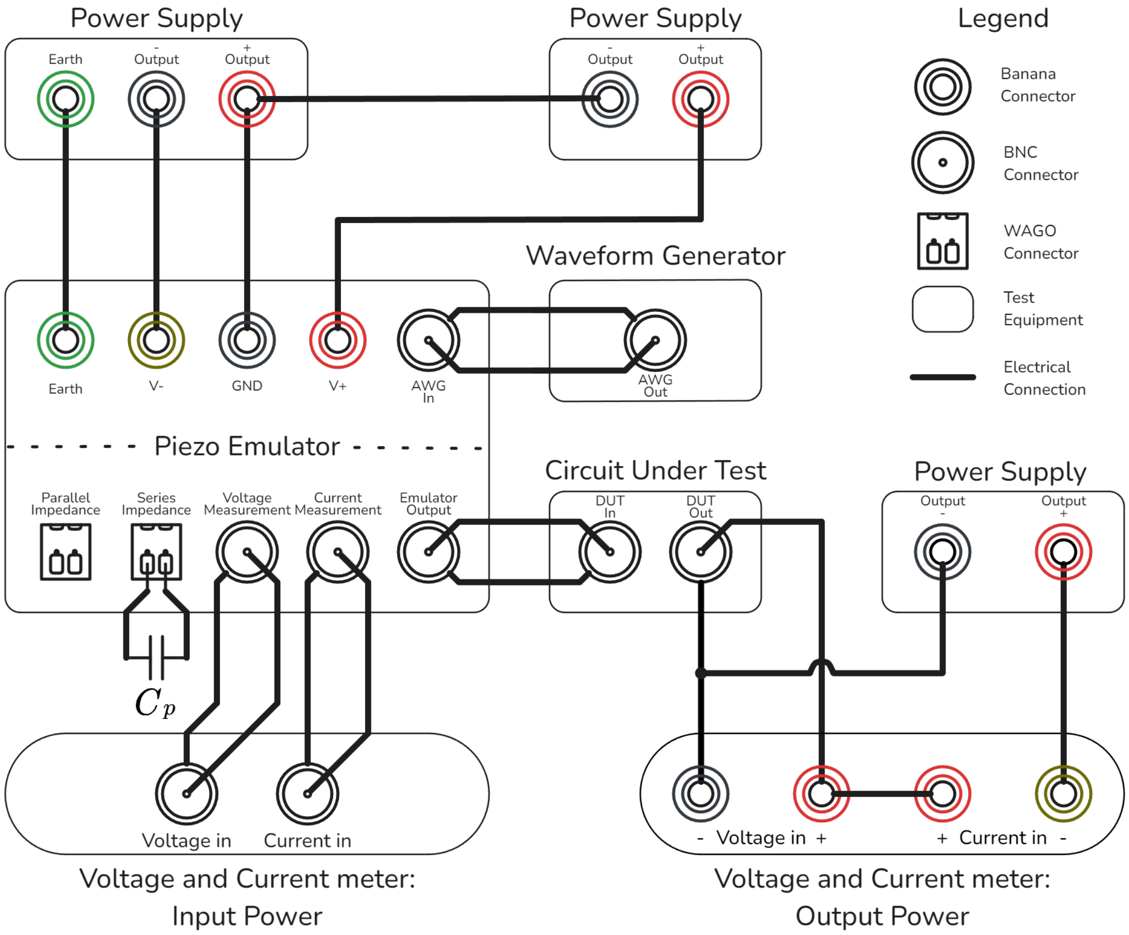

Figure C.2: Wiring diagram showing all electrical connections required to operate the emulator. Includes signal, power, and measurement interfaces.

5. **Power measurement:**
   - Place one Joulescope in series with the emulator output to measure input power to the DUT.
   - Place the second Joulescope at the output of the DUT to monitor extracted power.
   - For voltages above $\pm 15\,\mathrm{V}$, use the onboard resistor divider in the emulator output panel to safely attenuate the signal for the JS220 input.

Remarks

The emulator is intended for use with energy extraction circuits that expect PEH-like sources. It is not a general-purpose signal generator and should not be connected directly to low-impedance circuits without appropriate consideration.

D

Author Contributions and Use of AI Assistance

All conceptual designs, prototypes, and evaluation work presented in this thesis were carried out by the author. In this work, large language model services like ChatGPT have been used to improve the spelling, grammar, structure, and flow of written text. AI services have not been used to generate any informative content, technical explanations, or original ideas related to the research topic. All domain-specific knowledge, analysis, design, and conclusions presented are the result of the author's own understanding and work.